Three-Dimensional Microwave Imaging for Indoor Environments

Simon Scott

Three-Dimensional Microwave Imaging for Indoor Environments

by

Simon Scott

A dissertation submitted in partial satisfaction of the

requirements for the degree of

Doctor of Philosophy

in

Engineering - Electrical Engineering and Computer Sciences

in the

Graduate Division

of the

University of California, Berkeley

Committee in charge:

Professor John Wawrzynek, Chair
Professor Ali Niknejad
Associate Professor Aaron Parsons

Summer 2017

Three-Dimensional Microwave Imaging for Indoor Environments

Copyright 2017
by
Simon Scott

Abstract

Three-Dimensional Microwave Imaging for Indoor Environments

by

Simon Scott

Doctor of Philosophy in Engineering - Electrical Engineering and Computer Sciences

University of California, Berkeley

Professor John Wawrzynek, Chair

Microwave imaging involves the use of antenna arrays, operating at microwave and millimeter-wave frequencies, for capturing images of real-world objects. Typically, one or more antennas in the array illuminate the scene with a radio-frequency (RF) signal. Part of this signal reflects back to the other antennas, which record both the amplitude and phase of the reflected signal. These reflected RF signals are then processed to form an image of the scene.

This work focuses on using planar antenna arrays, operating between 17 and 26 GHz, to capture three-dimensional images of people and other objects inside a room. Such an imaging system enables applications such as indoor positioning and tracking, health monitoring and hand gesture recognition.

Microwave imaging techniques based on beamforming cannot be used for indoor imaging, as most objects lie within the array near-field. Therefore, the range-migration algorithm (RMA) is used instead, as it compensates for the curvature of the reflected wavefronts, hence enabling near-field imaging. It is also based on fast-Fourier transforms and is therefore computationally efficient. A number of novel RMA variants were developed to support a wider variety of antenna array configurations, as well as to generate 3-D velocity maps of objects moving around a room.

The choice of antenna array configuration, microwave transceiver components and transmit power has a significant effect on both the energy consumed by the imaging system and the quality of the resulting images. A generic microwave imaging testbed was therefore built to characterize the effect of these antenna array parameters on image quality in the 20 GHz band. All variants of the RMA were compared and found to produce good quality three-dimensional images with transmit power levels as low as 1 µW. With an array size of 80×80 antennas, most of the imaging algorithms were able to image objects at 0.5 m range with 12.5 mm resolution, although some were only able to achieve 20 mm resolution. Increasing the size of the antenna array further results in a proportional improvement in image resolution and image SNR, until the resolution reaches the half-wavelength limit.

While microwave imaging is not a new technology, it has seen little commercial success due to the cost and power consumption of the large number of antennas and radio transceivers required to build such a system. The cost and power consumption can be reduced by using low-power and low-cost components in both the transmit and receive RF chains, even if these components have poor noise figures. Alternatively, the cost and power consumption can be reduced by decreasing the number of antennas in the array, while keeping the aperture constant. This reduction in antenna count is achieved by randomly depopulating the array, resulting in a sparse antenna array. A novel compressive sensing algorithm, coupled with the wavelet transform, is used to process the samples collected by the sparse array and form a 3-D image of the scene. This algorithm works well for antenna arrays that are up to 96% sparse, equating to a 25 times reduction in the number of required antennas.

For microwave imaging to be useful, it needs to capture images of the scene in real time. The architecture of a system capable of capturing real-time 3-D microwave images is therefore designed. The system consists of a modular antenna array, constructed by plugging RF daughtercards into a carrier board. Each daughtercard is a self-contained radio system, containing an antenna, RF transceiver baseband signal chain, and analog-to-digital converters. A small number of daughtercards have been built, and proven to be suitable for real-time microwave imaging. By arranging these daughtercards in different ways, any antenna array pattern can be built. This architecture allows real-time microwave imaging systems to be rapidly prototyped, while still being able to generate images at video frame rates.

Contents

List of Figures

List of Tables

Glossary of Terms

ADC: Analog to Digital Converter: a device that converts a continuous (analog) signal to a discrete digital number.

ASIC: Application-specific Integrated Circuit: an integrated circuit that is designed for a specific application, rather than for general use.

cross-range: In radar systems, cross-range refers to the spatial axes that are parallel to the plane of the antenna array. The cross-range resolution is therefore the resolution in the plane of the array. Cross-range is also called azimuth.

colocated: When the transmitting antenna and the receiving antenna are in the same location. Either the same antenna can operate as both the transmitter and the receiver, or the two antennas are placed so close together that they can be approximated as being in the same location.

CS: Compressive Sensing: a technique whereby a signal can be sampled at a rate below the Nyquist threshold.

CW: Continuous Wave: refers to an RF signal that contains only one frequency. Also known as a monochromatic wave.

k_x, k_y, k_z**:**   The spatial frequency variables of spatial co-ordinates x, y and z.

LNA: Low-Noise Amplifier, usually used in the receive chain of a radio transceiver.

MIMO: Antenna arrays containing multiple transmit and multiple receive antennas.

NF: Noise Figure: a measure of how much a component degrades the signal-to-noise ratio of the signal.

PA: Power Amplifier: an radio-frequency amplifier, usually used to drive a transmitting antenna.

range: In radar systems, range refers to the axis that is normal to the plane of the antenna array.

RF: Radio Frequency.

RMA: The Range Migration Algorithm, a popular algorithm for microwave imaging.

SNR: Signal-to-Noise Ratio

STX: Single Transmitter, usually referring to a microwave imaging array with only one transmitting antenna.

UWB: Ultra Wideband: usually refers to a radio system operating over a wide bandwidth, such as 1 to 10 GHz.

voxel: A volumetric pixel, i.e. a single element or pixel in 3-D space.

X-MIMO: An antenna array that contains a linear array of transmit antennas on one axis and a linear array of receive antennas on the other axis, forming an X-pattern.

Acknowledgments

I would like to express my gratitude to John Wawrzynek for all the guidance he has given me over these past few years. Our conversations about my research have made me consider many aspects and avenues of this work that I would not have otherwise. Furthermore, the occasional nudge to continue working on a problem, even when no solution seemed apparent at the time, was always appreciated. I appreciated all your support and for allowing me to spend most of my time focusing on research, rather being distracted by administrative and funding concerns.

I would like to thank Aaron Parsons for his illuminating discussions on radio interferometry, and for helping me reconcile the apparent differences between antenna arrays for radio astronomy and antenna arrays for microwave imaging.

I would also like to thank Ali Niknejad for his assistance throughout the years in helping me improve my understanding of RF and analog circuits.

I would like to express my appreciation to all my friends at colleagues at the BWRC for their camaraderie and late night chats, especially Andrew and Nathan for answering all my dumb circuits questions.

To my family, I say thank you for everything you have done to help me reach this point.

And last, but not least, I would like to thank Claire for sticking by me all this time. Your support was invaluable and appreciated more than you can ever know.

Chapter 1

Introduction

Microwave imaging refers to the use of microwaves to capture images of real-world objects. While conventional optical imaging uses waves in the optical wavelengths to capture images, microwave imaging uses waves at microwave and millimeter-wave (mm-wave) frequencies.

While many types of microwave imaging exist, this work investigates active backscatter microwave imaging using an antenna array. In this type of imaging, one or more antennas in the array illuminate the scene with a radio-frequency (RF) signal. Part of this signal is reflected back to the other antennas, which record both the amplitude and phase of the reflected signal. These reflected RF signals are then processed to form an image of the scene. This imaging technique is also known as microwave holography, as images are formed by capturing the *whole* (*holo* in Ancient Greek) wave, i.e. both the amplitude and the phase.

The main focus of this work is capturing three-dimensional (3-D) images of indoor environments using microwave imaging. Since the most interesting objects in an indoor environment are arguably people, a large portion of this dissertation is dedicated to characterizing the effectiveness of this technique for imaging people.

While microwave imaging is not a new technique [1], few microwave imagers have been built to date that are able to create high-resolution images in an indoor environment. This is mainly due to the high cost of the large number of antennas and radio transceivers required to build such a system. However, the recent increase in commercial production of portable wireless devices has led to the availability of multi-GHz RF transceiver devices at very low cost.

Looking forward, we believe it may soon be commercially viable to build wall-size antenna arrays for microwave imaging. These arrays could be built by embedding the antennas and transceivers into large flexible sheets of material, such as wallpaper. For example, a large array of antennas could be printed using conductive ink [2] and connected to bare die RF transceivers embedded directly within the wallpaper, as in Figure 1.1. Such a system could be mounted unobtrusively within any room in a building, enabling applications such as gesture recognition for controlling multimedia devices or health monitoring. In most cases, it is expected that the resulting 3-D images will be consumed by machine rather than a human, most likely using a machine-learning algorithm to detect features and anomalies.
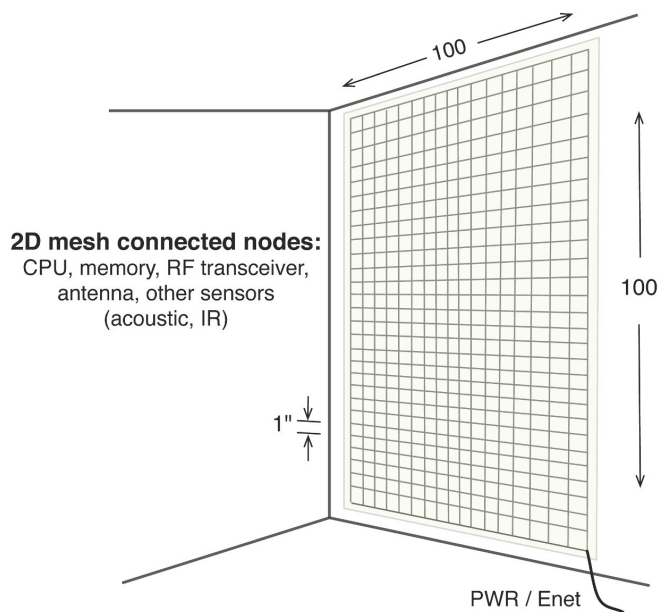
Figure 1.1: eWallpaper: an array of thousands of computing and sensing devices embedded into wallpaper, all connected using wires printed from conductive ink.

Image courtesy of John Wawrzynek

While conventional radar is technically a form of active backscatter microwave imaging, it is typically employed to image large objects in outdoor environments. Therefore, many of the techniques used in radar are not applicable for creating high-resolution images in a small indoor environment. While this will be discussed more in the next chapter, the main differences between the microwave imaging discussed here and conventional radar relate to the relationship between the size of the antenna array, the distance to the objects being imaged and the wavelength of the RF signal. Furthermore, radar creates 2-D images while this work is concerned with 3-D imaging. Therefore, for the sake of this discussion, radar will be considered separate to microwave imaging.

Since the underlying algorithms of microwave imaging are well-known [1] [3], this dissertation instead attempts to:

1. characterize the effect of antenna array and RF system parameters on resulting image quality, and

2. use these results to find ways to reduce system cost, such as by using noisy, low-power components or reducing the number of antennas through sparse-array techniques.

The rest of this chapter will present in more detail the mechanics of how microwave imaging works. This is followed by a discussion of the applications that microwave imaging enables, as well as the main challenges hindering microwave imaging from becoming a commonplace technology.

1.1 How Does Microwave Imaging Work?

Figure 1.2 highlights the many similarities between optical imaging, using a digital camera, and microwave imaging, using an antenna array. In the case of optical imaging, the sun provides a source of light that illuminates the object of interest. The light waves reflect off the object and are scattered in all directions. The scattered waves are then focused by a lens before being captured by an array of phototransistors, commonly known as CMOS or CCD sensor arrays. It is important to note that the phototransistor array records only the intensity of the light at each pixel, and not the phase.

(a) Optical imaging

(b) Microwave imaging
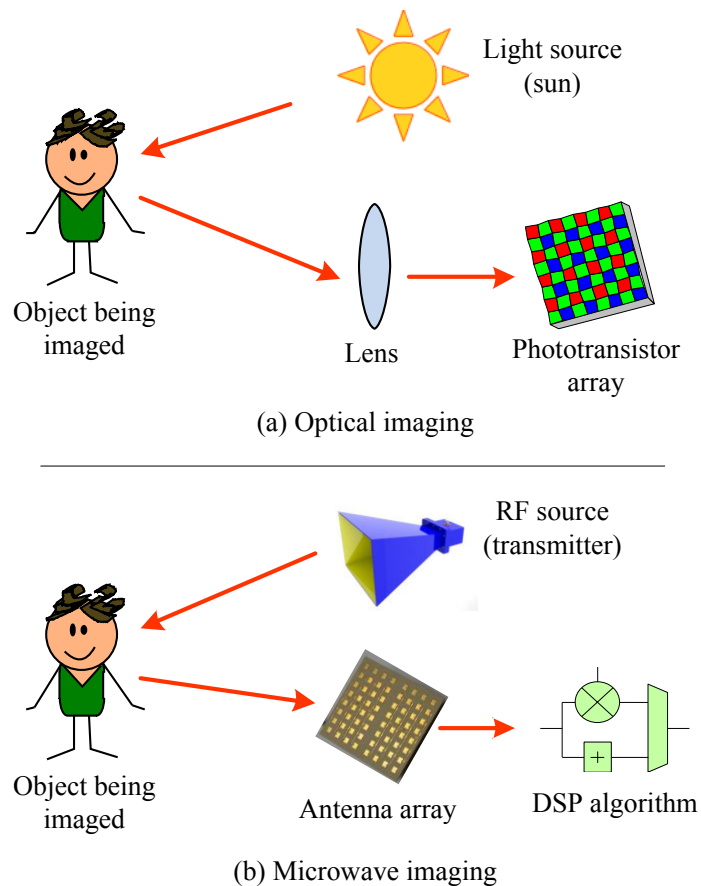
Figure 1.2: Comparison between optical imaging and microwave imaging.

Antenna array image taken from http://radarandlaserforum.com/showthread.php/3480-STIR-Plus-Vertical

Likewise, microwave imaging requires the object of interest to be illuminated by a source of microwaves, usually a radio transmitter. The radio waves reflect off the object of interest and are again scattered. While RF lenses for focusing the microwaves do exist, they are still experimental and fairly bulky (see [4] for an overview of microwave lenses). Therefore, rather than using a lens, the scattered waves are instead recorded directly by an array of

antennas. Since the radio receivers connected to each antenna record both the magnitude and phase of the scattered microwaves, digital signal processing can be used to refocus the scattered microwaves and form an image of the object.

If the object of interest is illuminated at multiple different microwave frequencies, and the reflected microwaves are captured at each of these frequencies using a 2-D antenna array, it is possible to refocus the microwaves at multiple depths (one depth point per frequency), allowing a 3-D image of the scene to be reconstructed.

1.2 Why is Microwave Imaging Interesting?

Microwave imaging makes possible many applications that are either difficult or not possible to achieve using optical imaging. For most of these applications, the advantage of microwave imaging over optical imaging stems either from the ease with which it can form 3-D images, or from its resilience to changing light conditions.

The primary applications that we foresee for microwave imaging include:

- **Indoor positioning of people:** there has been much interest lately in determining the position of a person inside a building for navigation purposes, such as finding your way around a shopping mall. The main techniques currently used include RF beacon triangulation [5] and WiFi fingerprinting [6]. However, if a 3-D image of the room can be generated, and the people within the image detected using a feature-recognition algorithm, then their position within the building can be precisely determined.

- **User identification and tracking in the smart home:** the obvious extension of the above application is to integrate this technology into the "smart home". The antennas could be integrated into a wallpaper-like material (such as in Figure 1.1) and placed on the walls in multiple rooms of the house. An integrated computing system could then identify individual residents from their body shape or gait, and track them as they move from room to room. One could imagine this leading to a scenario where your favorite radio or TV station follows you, jumping from media device to media device, as you move around.

- **Hand gesture recognition:** if a home contains arrays of antennas for microwave imaging, then this system can be used for not only tracking the occupants, but also creating 3-D images of their hands for gesture recognition. This system could therefore allow a person to control multimedia devices and appliances in their home with simple hand gestures. The antenna arrays could even be integrated directly into the appliances themselves.

- **Health monitoring:** by continuously imaging a person, physiological changes in their body, which are often an early indication of health problems, can be detected. Examples of such health monitoring applications are tracking long-term changes in

posture, resting heart rate or respiratory rate. The motion of a person's chest due to the beating of their heart and respiration of their lungs causes a Doppler shift in the reflected RF signal when imaging the person. This Doppler shift can be measured and used to calculate their heart and respiratory rate [7] [8]. Another simple application would be to detect when a person falls and is unable to get up.

- **Security:** microwave imaging is already present in some airports in the form of *millimeter wave scanners* for concealed weapon detection. The current devices use a linear antenna array that is mechanically swept to create a 2-D antenna array. These mechanical devices could be replaced with a fixed 2-D antenna mounted on the walls of the airport corridors that are continuously scanning for concealed weapons.

The microwave imaging techniques and systems developed in this dissertation will target the first three applications, as we believe that they will have the most impact on everyday life in the future.

1.2.1 Competing technologies

Microwave imaging is not the only technology available for capturing 3-D images of objects and people in an indoor environment. In fact, some of the applications mentioned in the previous section are already served by other technologies, but many of these have their own drawbacks. A comparison between microwave imaging and competing technologies is therefore given in Table 1.1.

The first three competing technologies are all optical in nature, and hence provide high resolution. Structured light, such as used in the Microsoft Kinect, is a technique whereby a speckle pattern is projected onto the scene and depth is computed from the deformation of this speckle pattern. This technique can provide high-resolution images, but does not work well in bright light [9].

If two optical cameras, placed a known distance apart, image the same scene, they will record the scene from two different perspectives. The relative shift, i.e. the disparity, of a single point in the scene between the two camera perspectives can be calculated, allowing the depth of that point can be computed. Disparity 3-D imaging can also generate high-resolution images, but often gives noisy depth measurements [10].

LIDAR generates high-resolution images by spinning a laser range finder so that it measures the distance from the LIDAR unit to every point in the scene. Unfortunately, most LIDAR units are bulky, expensive and power hungry.

On a smaller scale, single-chip ultrasound and microwave arrays have been built for imaging. Sonichip [11] uses beamforming techniques to sweep an ultrasound beam over the scene, imaging it. However, due to the high attenuation of ultrasound in air, the range is very limited. Project Soli [1], a radar transceiver on a chip, is used for hand gesture recognition,

---

[1]https://atap.google.com/soli/

Table 1.1: Comparison between different 3-D imaging technologies

Imaging Technology	Example	Resol. @1m	Range	Problems
Structured light	Microsoft Kinect [9]	2mm	3m	Does not work in bright light, bulky
Disparity measurement	Dual optical cameras [10]	2mm	5m	Computationally expensive, noisy depth measurements
LIDAR	ScanLook [1]	40mm	100m	Very bulky, expensive and power hungry
Ultrasound beamforming	SoniChip [11]	130mm	1m	Low resolution, limited range due to high signal attenuation in air
Radar Doppler measurement	Google Project Soli [2]	N/A	< 0.5m	No actual imaging, just range and Doppler measurements
Microwave imaging	This work at 20GHz	20mm	> 5m	Resolution too low to recognize faces

[1] https://www.lidarusa.com/scanlook_trex.html
[2] https://atap.google.com/soli/

but does not actually image the scene. Instead it only takes range, reflectivity and Doppler measurements and matches these against a known patterns to detect different hand gestures.

Microwave imaging does provide better range than many of the competing technologies, works in all light conditions, and can be made very compact through the use of printed antennas. Microwave imaging does, however, suffer from lower resolution than all optical solutions, as the achievable resolution is limited to half the wavelength of the RF carrier frequency. Therefore, microwave imaging is best suited to large indoor environments where only moderate resolution is required, such as locating people or recognizing gestures and postures.

1.3 Cost and Power: the Challenges of Microwave Imaging

The main challenge preventing the commercialization of microwave imaging systems today is the high cost of building large antenna arrays. Since the received RF power and phase needs to be recorded at each antenna, the antenna outputs cannot simply be summed as in a phased array; instead, each antenna requires its own receiver. This dissertation therefore investigates two approaches to making microwave imaging systems affordable:

1. Since each voxel (a 3-D pixel) in the output image is calculated by integrating over

all antenna/receiver samples, the noise in each sample is reduced through averaging. Therefore, fairly noisy (and hence low-cost) components can be used for the receiver circuit. Furthermore, this averaging also means that a low power RF transmitter can be used to illuminate the scene, further reducing the cost.

2. Conventional microwave imaging requires antennas to be placed less than a wavelength apart in a regular grid to sample the reflected waves. However, if the characteristics of the scene are known a-priori, then not all antennas are required. The array can be depopulated by randomly removing antennas, and the missing samples can be recovered using a compressive sensing algorithm. The resulting sparse antenna array has a lower cost than a dense array.

Another concern of microwave imaging that is frequently mentioned is total system power consumption. Fortunately, the above two cost reduction techniques will also reduce the power consumption of each RF transmitter and receiver, as well as reducing the total number of transmitters and receivers required, hence lowering overall power consumption.

Furthermore, microwave imaging systems provide a simple mechanism for motion detection via a Doppler measurement. Since the Doppler measurements can be made using just a few antennas, most of the array can be turned off during periods of inactivity in the room, reducing power consumption. Then, when motion is detected, the entire array can switch on to provide full-resolution imaging.

1.4 Contribution of this Work

This work makes a number of contributions to the field of 3-D microwave imaging, with an emphasis on improving the commercial feasibility of such imaging systems. In particular, the following novel research is presented:

- New variations of the range migration algorithm that allow 3-D images to be captured using independent transmit and receive antenna arrays.

- A new 3-D Doppler imaging algorithm that allows simultaneous imaging and velocity measurements within the array near-field.

- New experimental characterization of the effect of radio transceiver and antenna array design on image quality. Little to no experimental characterization of 3-D microwave imaging systems has been done previously.

- A new figure of merit quantifying the efficiency with which these systems are able to form images. This lead to a novel methodology for designing energy- and cost-efficient microwave imaging systems.

- A new compressive sensing algorithm for 3-D microwave imaging that allows images to be formed using sparse antenna arrays. Previous work had required the scene to be spatially sparse (i.e. mostly empty), but this new algorithm has no such requirement.

- A novel hardware and software architecture for building compact, modular real-time 3-D microwave imaging systems.

1.5 Structure of the Dissertation

The next chapter provides a mathematical formulation of the range migration algorithm (RMA), the signal processing algorithm used for most microwave imaging systems. Chapter 2 also describes a number of variations on the basic algorithm, some of which are novel. To characterize the effect of algorithm variation, antenna array parameters and RF circuit design on the quality of images produced by microwave imaging systems, a configurable microwave imaging testbed was built, as described in Chapter 3. Chapter 4 provides the results of these characterization experiments.

As mentioned earlier, the cost and power of a microwave imaging system can be reduced by using low power, noisy transmitter and receiver circuits. The relationship between energy consumption, cost and image quality is explored in Chapter 5, as well as some guidelines for producing cost-, size- and energy-efficient microwave imaging systems.

Chapter 6 investigates the use of sparse antenna arrays and compressive sensing for microwave imaging. Chapter 7 then briefly discusses two other possible techniques for microwave imaging: timed arrays and interferometry. Finally, a prototype for a real-time microwave imaging system was built. The guidelines for designing such a system, as well as the finished prototype, are presented in Chapter 8.

Chapter 9 provides a summary of the work that was completed for this dissertation, as well as discussing ways to extend this work further in the future.

Chapter 2

3-D Microwave Imaging Algorithms for Dense Antenna Arrays

This chapter describes an efficient algorithm for capturing 3-D images of a scene using a planar antenna array. The obvious approach for imaging a scene would be to operate the antenna array as a phased array, and raster sweep the resulting narrow RF beam over the scene, such as is often done in radar [12, ch. 10]. However, for indoor imaging, most of the objects of interest lie within the array near-field, where it is difficult to form a directive beam [13].

The next obvious approach would be to use synthetic aperture radar (SAR) algorithms for imaging, such as are used for satellite imaging of the earth. Unfortunately, most SAR algorithms cannot be used for the same reason that beamforming cannot be used. The SAR algorithms assume that the reflected RF wave is planar by the time it reaches the receiving antenna array. For indoor imaging where the objects are close to the array, this planar assumption cannot be made and the curvature of the reflected wavefront needs to be taken into account.

Therefore, the most commonly used algorithm for microwave imaging is the range-migration algorithm (RMA), as it not only takes into account the wavefront curvature, but can also be computed efficiently. This efficiency comes from the fact that the RMA uses the Dix approximation, i.e. only direct reflections are considered and multipathing is ignored. This approximation allows the algorithm to be expressed using Fourier transforms and computed using fast Fourier transforms (FFTs). The RMA is also known as the backward-wave reconstruction algorithm [14], as it forms an image by coherently integrating the reflected wave over a synthesized aperture, and then back-projecting it into the scene. The RMA is derived here from first principles for multiple different antenna array configurations.

2.1 Review of Existing Work on the Range Migration Algorithm

The range migration algorithm has its origins in acoustic imaging. It was first used in geological surveying applications [15], where acoustic waves are used to image underground objects. It was also used in its early days for ultrasound medical imaging [14].

The RMA first appeared in its modern form for radar imaging, where a linear antenna array was used to create 2-D images [16] [17]. Unfortunately, 2-D images are not very useful for detecting people in a 3D environment, and so has limited applicability to this work. The algorithm has since been extended to capturing 3-D images using a 2-D planar antenna array [1] [3], primarily for hidden weapon detection.

The conventional 3-D RMA assumes a planar rectangular antenna array of colocated transmit and receive antennas, with antennas spaced less than a wavelength apart. This arrangement is the easiest to analyze and generally produces the highest resolution images. A variant of this algorithm is MIMO (multiple-input, multiple-output) RMA, where independent transmit and receive antenna arrays can be used. MIMO RMA was first developed for 2D microwave imaging by Soumekh [18], and later extended to 3-D imaging with separate planar antenna arrays by both the author of this dissertation, and Zhuge and Yarovoy [19] (with the latter publishing first by a few months).

Conventional (colocated) RMA and MIMO RMA differ not only in antenna placement, but also in how the reflected wave is sampled. For colocated RMA, every antenna is both a transmitter and a receiver. When a particular antenna transmits, only that same antenna will sample the reflected RF wave; all other antennas remain idle (note that, in practice, colocation is approximated by having the nearest neighboring antenna act as the receiver). The original antenna then becomes idle and the next antenna in the array becomes the transmitter. This process will repeat until all antennas have transmitted.

However, when an antenna transmits in the MIMO case, all receiver antennas in the array will simultaneously sample the received waveform. This process is repeated for each of the transmitters.

Although the MIMO algorithm allows independent transmit and receive antenna arrays, the individual array elements still need to be placed less than a wavelength apart. A common MIMO implementation is to have a large receive antenna array with a smaller transmit array in the center, as shown in Figure 2.1. There are two special cases of the MIMO algorithm that will be investigated further here: X-MIMO and single-transmitter MIMO. In the X-MIMO configuration, the transmit antennas form a linear array on the vertical axis, while the receive antennas form a linear array on the horizontal axis, creating a cross or rotated-X pattern. The single-transmitter case has a large 2D array of receivers with a single transmitter placed at the center, with this arrangement being first published by this dissertation's author.

The RMA variants described above are illustrated graphically in Figure 2.1 and will be derived in this chapter.

A novel Doppler extension of the RMA will also be introduced. Rather than extending
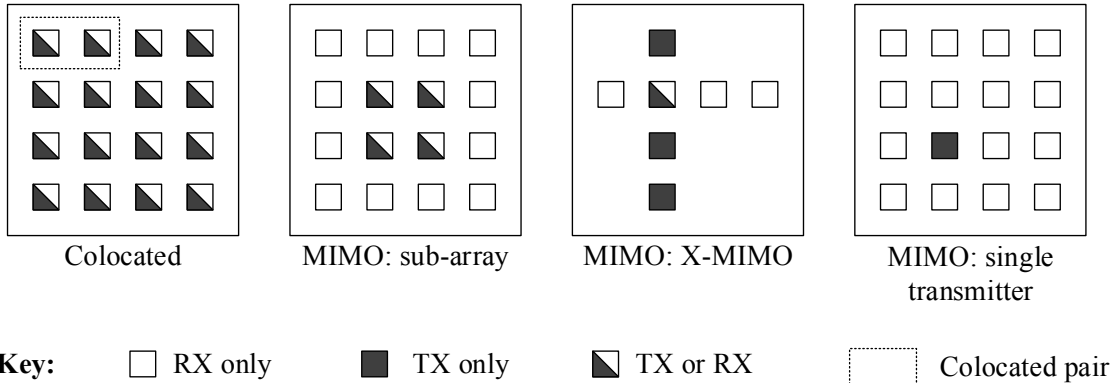
Figure 2.1: Antenna array configuration for the different RMA variants, showing the relative positions of the transmit and receive antennas

the RMA to a new array architecture, the Doppler extension enables Doppler measurements to be made using one of the existing antenna arrays described above. This Doppler algorithm calculates the velocity of every voxel in the resulting 3-D images. This information allows a velocity map to be overlaid on the 3-D image of the scene, so that the speed of each object in the scene can be determined. This is particularly useful for gesture recognition, as it enables a person's hands to be imaged while simultaneously determining the speed at which each of their fingers is moving.

2.2   Variables and Coordinate System

Figure 2.2 establishes a unified coordinate system to aid in the explanation and derivation of the different RMA variants. This coordinate system, as well as the common variables, are defined as follows:

- The antenna array lies in the xy-plane at $z = Z_0$.

- The transmitter transmits a continuous wave (CW) at frequency ω (rad/s), that is discretely stepped from ω_{min} to ω_{max}.

- $f(x, y, z)$ is the reflectivity function of the scene, i.e. the image we are trying to recreate. Note that "imaging the scene" actually means finding the function f that defines how well each point in the scene reflects microwaves.

- $s(x_a, y_a, \omega)$ is the complex reflection recorded at antenna position (x_a, y_a, Z_0) and at frequency ω, when both the transmitting and receiving antennas are colocated.

- $s(x_t, y_t, x_r, y_r, \omega)$ is the complex reflection recorded at receiving antenna position (x_r, y_r, Z_0) for the MIMO algorithm, when the antenna at position (x_t, y_t, Z_0) transmits at frequency ω.

- $k = \frac{\omega}{c}$ is the wavenumber of the transmitted signal.

- k_x, k_y, k_z are the spatial frequency variables of x, y, z.
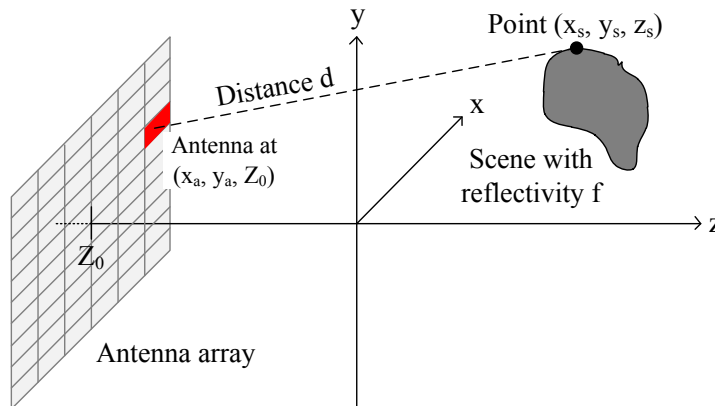
Figure 2.2: Scene geometry for the derivation of the range migration algorithm

2.3 Colocated Range Migration Algorithm

Only two antennas in the array are active in the colocated algorithm at any one time: the transmitting antenna and its neighboring receive antenna. A continuous-wave (CW) signal is transmitted by the transmitter, which reflects off objects in the scene and this reflection is coherently recorded by the neighboring receiver. This is repeated for each frequency step from ω_{min} to ω_{max}. After recording reflections $s(x_a, y_a, \omega)$ at all frequencies, the next two antennas in the array operate as the transmit/receive pair and the process is repeated.

The colocated algorithm assumes that the transmitting and receiving antennas are colocated (i.e. in the exact same position), but in practice colocation is approximated by having neighboring antennas act as a transmit/receive pair. Therefore, a common technique is to take position (x_a, y_a) as the position halfway between the neighboring antennas.

2.3.1 Derivation of the colocated range migration algorithm

The round-trip phase delay from transmit/receive antenna at (x_a, y_a, Z_0) to point reflector in the scene at co-ordinate (x, y, z) is:

$$2k \times d, \text{ where distance } d = \sqrt{(x - x_a)^2 + (y - y_a)^2 + (z - Z_0)^2} \qquad (2.1)$$

Attenuation effects due to path loss are ignored in the colocated range migration algorithm, as they are difficult to handle and have little effect on the resulting image quality [3].

Therefore, if the point reflector at co-ordinate (x, y, z) has reflectivity $f(x, y, z)$, the response s recorded at the antenna at frequency ω will be:

$$s(x_a, y_a, \omega) = f(x, y, z) \times e^{-j2k\sqrt{(x-x_a)^2+(y-y_a)^2+(z-Z_0)^2}} \tag{2.2}$$

By regarding the scene as a collection of point reflectors, the combined reflection recorded at antenna (x_a, y_a, Z_0) is obtained by integrating (2.2) over the scene:

$$s(x_a, y_a, \omega) = \iiint_{scene} f(x, y, z) \times e^{-j2k\sqrt{(x-x_a)^2+(y-y_a)^2+(z-Z_0)^2}} dx\,dy\,dz \tag{2.3}$$

The square-root in the exponential term in (2.3) makes the expression difficult to invert to obtain $f(x, y, z)$. Fortunately, the exponential term describes a spherical wave, which can be expressed as a sum of plane waves [20], again ignoring amplitude effects:

$$e^{-j2k\sqrt{(x-x_a)^2+(y-y_a)^2+(z-Z_0)^2}} = \iint e^{-j(k_{x_a}(x-x_a)+k_{y_a}(y-y_a)+k_z(z-Z_0))} dk_{x_a} dk_{y_a} \tag{2.4}$$

By combining (2.3) and (2.4) and rearranging the order of the integrals, we obtain:

$$s(x_a, y_a, \omega) = \iint \left[\iiint_{scene} f(x, y, z) \times e^{-j(k_{x_a}x+k_{y_a}y+k_z z)} dx\,dy\,dz \right]$$
$$\times e^{jk_z Z_0} e^{j(k_{x_a}x_a+k_{y_a}y_a)} dk_{x_a} dk_{y_a} \tag{2.5}$$

The inner triple integral represents the 3D spatial Fourier transform of $f(x, y, z)$, while the outer double integral can be expressed as the 2D inverse Fourier transform with respect to (k_{x_a}, k_{y_a}). We therefore rewrite (2.5) as:

$$s(x_a, y_a, \omega) = FT_{2D}^{-1} \left\{ FT_{3D} \left\{ f(x, y, z) \right\} e^{jk_z Z_0} \right\} \tag{2.6}$$

Inverting the Fourier transforms, we can reconstruct the original scene using:

$$f(x, y, z) = FT_{3D}^{-1} \left\{ \Phi \left\{ FT_{2D} \left\{ s(x_a, y_a, \omega) \right\} \right\} e^{-jk_z Z_0} \right\} \tag{2.7}$$

where the inner 2D Fourier transform is from (x_a, y_a) space to (k_{x_a}, k_{y_a}) space, and the outer 3D inverse Fourier transform is from (k_x, k_y, k_z) space to (x, y, z) space. To make the domains of these Fourier transforms compatible, $\Phi\{\cdot\}$ is the Stolt transform [21] from $(k_{x_a}, k_{y_a}, \omega)$ space to (k_x, k_y, k_z) space, according to:

$$\begin{aligned} k_x &= k_{x_a} \\ k_y &= k_{y_a} \\ k_z &= \sqrt{4\frac{\omega^2}{c^2} - k_x^2 - k_y^2} \end{aligned} \tag{2.8}$$

2.3.2   Implementation details

The Stolt transform is only valid where $4\frac{\omega^2}{c^2} \geq k_x^2 + k_y^2$, as this is required for the radiation condition. In practice, (2.7) is solved using discrete Fourier transforms. Therefore, the Stolt transform is implemented as an interpolation from one discrete co-ordinate system to the other. Since the mapping is non-linear and restricted (due to the radiation condition), multiple data points in the (k_{xa}, k_{ya}, ω) space may map to the same coordinate in (k_x, k_y, k_z) space, and should be averaged [22], while some coordinates in (k_x, k_y, k_z) space may not have any samples mapped to them and must be zero filled.

To most effectively fill the (k_x, k_y, k_z) space with usable data, it was found useful to oversample in the k_z axis before applying the Stolt transform, so that number of non-zero data points remains the same after the transform. This oversampling is especially advantageous when the antennas are less than half a wavelength apart.

When capturing real data, the receiving antenna does not usually connect directly to the ADC, but rather via a cable and/or components. Therefore, the phase delay introduced by these components must be removed before processing. Assuming the cable has length L_{cab} and propagation velocity v_{cab}, the phase delay of the cable is given by:

$$\theta_{cab} = \frac{\omega L_{cab}}{v_{cab}} \tag{2.9}$$

To remove this phase delay, we simply modify the colocated range-migration algorithm as follows:

$$f(x, y, z) = FT_{3D}^{-1} \left\{ \Phi \left\{ FT_{2D} \left\{ s\left(x_a, y_a, \omega\right) e^{j\theta_{cab}} \right\} \right\} e^{-jk_z Z_0} \right\} \tag{2.10}$$

The completed colocated algorithm can therefore be expressed as the block diagram in Figure 2.3.

2.4   MIMO Range Migration Algorithm

While the equations described thus far assume colocated transmit and receive antennas, bistatic RMA variants have been developed for 3D imaging with independent MIMO-like transmit and receive planar antenna arrays. Three MIMO cases will be derived here:

1. A rectangular transmit array containing $\sqrt{N} \times \sqrt{N}$ transmit antennas and a separate rectangular receive array containing $\sqrt{M} \times \sqrt{M}$ antennas

2. A rectangular array of receive antennas with a single transmit antenna placed at the center of the array

3. An X-MIMO array, containing a linear array of transmit antennas on one axis and a linear array of receive antennas on the other axis
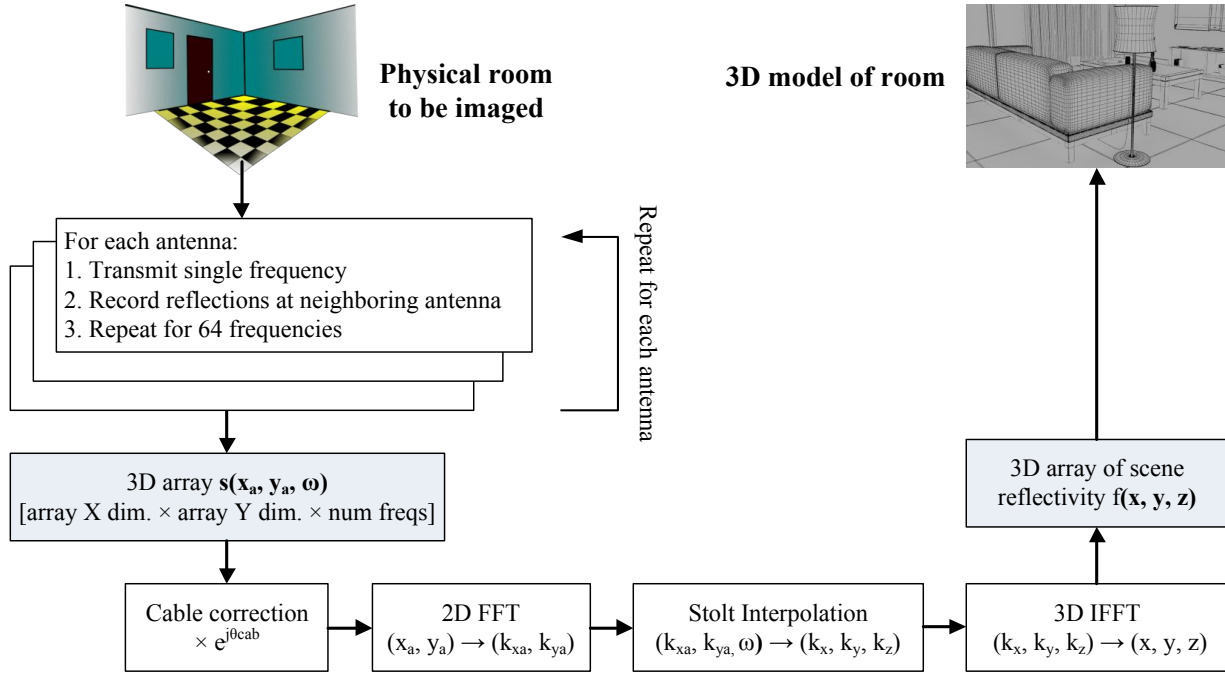
Figure 2.3: Block diagram for the colocated RMA

2.4.1 N-transmitter M-receiver MIMO algorithm

When an antenna in the transmitting array transmits at frequency ω, every antenna in the receive array simultaneously records the reflected response that they receive. This process is repeated for each transmitting antenna, and the resulting responses are recorded as $s(x_t, y_t, x_r, y_r, \omega)$, where (x_t, y_t, Z_0) is the position of the transmitting antenna and (x_r, y_r, Z_0) is the position of the receiving antenna.

If the scene contains a single point reflector at position (x, y, z) with reflectivity $f(x, y, z)$, the signal recorded back at the receiving antennas will be:

$$s(x_t, y_t, x_r, y_r, \omega) = \frac{f(x, y, z)}{R_t R_r} \times e^{-jkR_t} \times e^{-jkR_r} \tag{2.11}$$

where $R_t = \sqrt{(x - x_t)^2 + (y - y_t)^2 + (z - Z_0)^2}$ is the distance from the transmitter to the point reflector, and $R_r = \sqrt{(x - x_r)^2 + (y - y_r)^2 + (z - Z_0)^2}$ is the distance from the point reflector back to the receiving antenna. The exponential terms therefore represent the phase delay from the transmit antenna to the point reflector and back to the receive antenna. The decrease in amplitude due to path loss is included in (2.11), as it can be handled efficiently in this case. Note that s is the phase and amplitude of the received signal (in volts or field strength), and not power; hence the distance is not squared. To get the response for the entire scene, integrate over all space:

$$s(x_t, y_t, x_r, y_r, \omega) = \iiint\limits_{scene} \frac{f(x,y,z)}{R_t R_r} \times e^{-jkR_t} \times e^{-jkR_r} dxdydz \qquad (2.12)$$

Again, the exponential terms can be expressed as sums of plane waves [20], such as:

$$
\begin{aligned}
\frac{e^{-jkR_t}}{R_t} &= \frac{e^{-jk\sqrt{(x-x_t)^2+(y-y_t)^2+(z-Z_0)^2}}}{\sqrt{(x-x_t)^2+(y-y_t)^2+(z-Z_0)^2}} \\
&= \frac{1}{k_{z_t}} \iint e^{-j\left(k_{x_t}(x-x_t)+k_{y_t}(y-y_t)+k_{z_t}(z-Z_0)\right)} dk_{x_t} dk_{y_t}
\end{aligned}
\qquad (2.13)
$$

Substituting (2.13) in (2.12) for both R_t and R_r:

$$
\begin{aligned}
s(x_t, y_t, x_r, y_r, \omega) = \iiint\limits_{scene} f(x,y,z) &\times \frac{1}{k_{z_t}} \times \iint e^{-j\left(k_{x_t}(x-x_t)+k_{y_t}(y-y_t)+k_{z_t}(z-Z_0)\right)} dk_{x_t} dk_{y_t} \\
&\times \frac{1}{k_{z_r}} \times \iint e^{-j(k_{x_r}(x-x_r)+k_{y_r}(y-y_r)+k_{z_r}(z-Z_0))} dk_{x_r} dk_{y_r} dxdydz \quad (2.14)
\end{aligned}
$$

Rearranging the integrals, we obtain:

$$
\begin{aligned}
s(x_t, y_t, x_r, y_r, \omega) = \iiiint &\left[\iiint\limits_{scene} f(x,y,z) e^{-j\left(\left(k_{x_t}+k_{x_r}\right)x+\left(k_{y_t}+k_{y_r}\right)y+\left(k_{z_t}+k_{z_r}\right)z\right)} dxdydz \right] \\
&\times \frac{e^{jk_z Z_0}}{k_{z_t} k_{z_r}} e^{j\left(k_{x_t} x_t+k_{y_t} y_t+k_{x_r} x_r+k_{y_r} y_r\right)} dk_{x_t} dk_{y_t} dk_{x_r} dk_{y_r} \quad (2.15)
\end{aligned}
$$

Noting that the triple inner integral represents a 3-D Fourier transform, and the four outer integrals represent a 4-D inverse Fourier transform, we can write:

$$s(x_t, y_t, x_r, y_r, \omega) = FT_{4D}^{-1} \left\{ FT_{3D} \left\{ f(x,y,z) \right\} \frac{e^{jk_z Z_0}}{k_{z_t} k_{z_r}} \right\} \qquad (2.16)$$

given that $k_x = k_{x_t} + k_{x_r}$, $k_y = k_{y_t} + k_{y_r}$, $k_z = k_{z_t} + k_{z_r}$. By inverting the Fourier transforms, the original scene is obtained:

$$f(x,y,z) = FT_{3D}^{-1} \left\{ \Phi \left\{ FT_{4D} \left\{ s(x_t, y_t, x_r, y_r, \omega) \right\} k_{z_t} k_{z_r} \right\} e^{-jk_z Z_0} \right\} \qquad (2.17)$$

where the inner 4D Fourier transform is from (x_t, y_t, x_r, y_r) to $(k_{x_t}, k_{y_t}, k_{x_r}, k_{y_r})$ and the outer inverse 3D Fourier transform is from (k_x, k_y, k_z) to (x, y, z). The Stolt transform $\Phi\{\cdot\}$ is therefore used to map from $(k_{x_t}, k_{y_t}, k_{x_r}, k_{y_r}, \omega)$ space to (k_x, k_y, k_z) space, according to:

$$\begin{aligned}
k_x &= k_{x_t} + k_{x_r} \\
k_y &= k_{y_t} + k_{y_r} \\
k_z &= k_{z_t} + k_{z_r} = \sqrt{\frac{\omega^2}{c^2} - k_{x_t}^2 - k_{y_t}^2} + \sqrt{\frac{\omega^2}{c^2} - k_{x_r}^2 - k_{y_r}^2}
\end{aligned}$$

$$(2.18)$$

2.4.2 Single transmitter MIMO algorithm

The single-transmitter algorithm has just one transmitting antenna, while all other antennas simultaneously act as receivers. The expression for this case is derived by combining Callow *et al.*'s approach [23] to 2D single-transmitter imaging with (2.17).

Since there is only one transmitter at the center of the array, x_t and y_t are both constants equal to 0. Similarly, the spatial frequency variables k_{x_t} and k_{y_t} also become zero. Equation (2.17) therefore simplifies to

$$f(x, y, z) = FT_{3D}^{-1} \left\{ \Phi \left\{ FT_{2D} \left\{ s(x_r, y_r, \omega) \right\} \right\} k_z e^{-jk_z Z_0} \right\} \tag{2.19}$$

where Stolt transform Φ now interpolates from $(k_{x_r}, k_{y_r}, \omega)$ space to (k_x, k_y, k_z) space.

2.4.3 The X-MIMO algorithm

Figure 2.1 illustrates the antenna arrangement for the X-MIMO algorithm: the transmitting antennas are arranged in a linear array along the y axis, while the receiving antennas form a linear array on the x axis. The obvious advantage of this arrangement is that it only requires $2N$ antennas, instead of N^2 antennas, for an $N \times N$ array. The disadvantage is that the achievable resolution is lower, as will be discussed later.

Since the transmitting antennas are arranged in a vertical line, $x_t = 0$. Similarly, $y_r = 0$ for the receiving antennas. With these variables constant, (2.17) simplifies to

$$f(x, y, z) = FT_{3D}^{-1} \left\{ \Phi \left\{ FT_{2D} \left\{ s(y_t, x_r, \omega) \right\} k_{z_t} k_{z_r} \right\} e^{-jk_z Z_0} \right\} \tag{2.20}$$

In this case, the Stolt transform Φ interpolates from $(k_{x_r}, k_{y_t}, \omega)$ space to (k_x, k_y, k_z) space according to:

$$\begin{aligned}
k_x &= k_{x_r} \\
k_y &= k_{y_t} \\
k_z &= k_{z_t} + k_{z_r} = \sqrt{\frac{\omega^2}{c^2} - k_{y_t}^2} + \sqrt{\frac{\omega^2}{c^2} - k_{x_r}^2}
\end{aligned}$$

$$(2.21)$$

Interestingly, the equation for the single transmitter and X-MIMO cases look very similar to (2.7), the equation for the colocated range migration algorithm. The main differences are in how the variables are calculated for the Stolt transform.

2.5 Doppler Range Migration Algorithm

Any object that moves during imaging will cause the reflected RF wave to be shifted in frequency (i.e. a Doppler shift). The velocity of the object can be determined by measuring this Doppler shift. A novel Doppler RMA was therefore designed to incorporate this Doppler shift measurement into the colocated RMA. This new algorithm produces both a deblurred 3D image of the room and a map of how fast each voxel is moving. This motion information aids applications such as activity detection, gesture recognition and fall tracking in the elderly.

The following additional variables are defined:

- R is the distance from antenna at position (x_a, y_a, Z_0) to point reflector at position (x, y, z).

- $m(x, y, z)$ is the velocity (m/s) of the point reflector at position (x, y, z).

- $\psi(x, y, z)$ is the Doppler shift caused by a moving point reflector at position (x, y, z).

- v is the velocity variable (m/s).

- ω_d is the Doppler shift variable (Hz).

- $m'(x, y, z)$ is the final velocity map, produced by the algorithm.

These variables and coordinate systems are also illustrated in Figure 2.4. Even though just a single point reflector is shown, the algorithm will compute the velocity of every point in the scene simultaneously. For the sake of simplicity, a colocated array is assumed, but, in practice, any array architecture can be used.
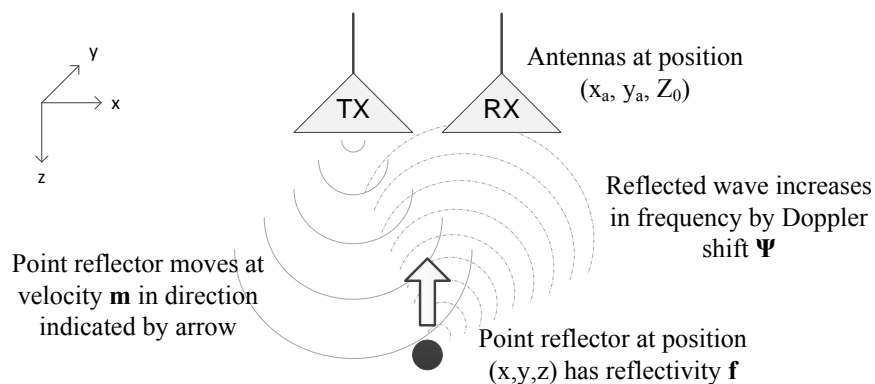
Figure 2.4: The variables and coordinate system used for the Doppler imaging

The received reflected signal, which has been Doppler shifted, is mixed with the transmit signal at each antenna to downconvert it to baseband. After this downconversion, the Doppler shift appears as a low frequency tone. Multiple samples need to be collected over

time to calculate the frequency of this tone. The signal at antenna at position (x_a, y_a, Z_0)
for transmit frequency ω is therefore given by:

$$s(x_a, y_a, \omega, t) = \iiint_{scene} f(x, y, z)e^{j\psi(x,y,z)t}e^{-j2kR}dx\,dy\,dz \qquad (2.22)$$

where distance $R = \sqrt{(x - x_a)^2 + (y - y_a)^2 + (z - Z_0)^2}$ and $\psi(x, y, z)$ is the Doppler shift.
Taking the Fourier transform with respect to time gives:

$$s(x_a, y_a, \omega, \omega_d) = \iiint_{scene} f(x, y, z)\delta(\omega_d - \psi(x, y, z))e^{-j2kR}dx\,dy\,dz \qquad (2.23)$$

where δ is the impulse function. An object at initial position (x, y, z), moving with velocity
$m(x, y, z)$, will cause a Doppler shift $\psi(x, y, z)$, given by:

$$\psi(x, y, z) = \frac{2m(x, y, z)\omega}{c} \qquad (2.24)$$

Since the Doppler shift is measured across many carrier frequencies ω, the effect of ω
on the Doppler shift needs to be removed by interpolating from ω_d-space (Hz) to v-space
(velocity, m/s) according to

$$v = \frac{\omega_d c}{2\omega} \qquad (2.25)$$

$$\therefore s(x_a, y_a, \omega, v) = \iiint_{scene} f(x, y, z)\delta(v - m(x, y, z))e^{-2jkR}dx\,dy\,dz \qquad (2.26)$$

The above expression gives the reflected signal recorded at antenna position (x_a, y_a, Z_0)
in terms of carrier frequency ω and object velocity v. If velocity v is set to a constant v_i,
the expression gives the response of the scene as if it only contained the objects that are
moving at velocity v_i, and these objects appeared stationery during imaging. $s(x_a, y_a, \omega, v)$
can therefore be regarded as a set of reflectivity responses $s_i(x_a, y_a, \omega)$, one for each possible
velocity v_i. The standard range migration algorithm, (2.7), is then run independently on
each s_i to generate a set of images $f_i(x, y, z)$, with each image showing the objects that are
moving at velocity v_i. The combined reflectivity image of the entire scene is given by:

$$f'(x, y, z) = \max_i f_i(x, y, z) \text{ , computed for each voxel.} \qquad (2.27)$$

The final velocity map m', giving the velocity of each and every point in the scene, is

$$m'(x, y, z) = v_{j(x,y,z)} \text{ , where } j(x, y, z) = \arg\max_i f_i(x, y, z) \qquad (2.28)$$

again computed on each voxel. The above two equations can be summarize by saying that
the algorithm produces a set of 3-D images, one for each discrete velocity. Each voxel will

appear in every 3-D image, but we only use the value of the voxel from the image in which it is the brightest (maximum), as this represents the true magnitude of that voxel. Furthermore, the velocity of that voxel comes from knowing in which 3-D image it was the brightest.

Figure 2.5 illustrates this Doppler algorithm graphically.

2.6   Comparison of RMA Variants

A number of RMA variants have been presented in this chapter. The differences in these variants can have a large effect on theoretical image resolution, time required to collect a single frame of data and computational complexity. These differences are shown in Table 2.1.

The 3-D image resolution in the xy-plane, achievable by each algorithm, can be approximated by [3] [19]

$$Resolution_{x,y} = \frac{\lambda_c R}{L_t + L_r} \qquad \text{[meters]} \qquad (2.29)$$

where λ_c is the wavelength of the RF carrier at the center frequency, R is the distance from the array to the center of the scene being imaged, L_t is the length of the transmit antenna array along one axis, and L_r is the length of the receive array along the same axis. This approximation holds true as long as R is of the same magnitude as, or larger than, L.

Table 2.1: Comparison between variants of the range migration algorithm

RMA Variant	Image Resol.	Data Collection Time	Computational Complexity
Colocated	$\frac{\lambda_c R}{2L}$	$N_x N_y N_f t_d$	$O\left(N_x N_y N_f \log\left(N_x N_y N_f\right)\right)$
N_{TX} M_{RX} MIMO	$\frac{\lambda_c R}{L_t + L_r}$	$N_{x_t} N_{y_t} N_f t_d$	$O\left(N_{x_t} N_{y_t} N_{x_r} N_{y_r} \log\left(N_{x_t} N_{y_t} N_{x_r} N_{y_r}\right)\right)$
Single TX MIMO	$\frac{\lambda_c R}{L}$	$N_f t_d$	Same as colocated
X-MIMO	$\frac{\lambda_c R}{L}$	$N_y N_f t_d$	Same as colocated
Doppler	N/A	$\max\left(t_{imaging} N_t, \frac{c}{2 f_c v_{min}}\right)$	$N_t \times O\left(\text{imaging alg.}\right)$

In Table 2.1, N_x and N_y are the number of antennas in the array in the x and y directions respectively. N_{x_t} and N_{y_t} are the number of transmitting antennas in those same directions. N_f is the number of unique frequencies that are used, while t_d is the transmitter dwell time at each frequency. f_c is the center transmit frequency, while v_{min} is the smallest velocity that the user would like to measure using the Doppler algorithm.

For a given physical array size, the colocated algorithm will produce the highest resolution images. This is because all antennas act as both transmitters and receivers, resulting in the transmit array and receive array each being equal to the physical array size. The result is that the array aperture is actually twice the physical array size, in each dimension. For the

MIMO algorithms, one of either the transmit array or the receive array will typically be smaller than the physical array size, resulting in lower resolution.

The MIMO algorithms are able to image the scene faster than the colocated algorithm, as the MIMO algorithms contain fewer transmitters than the colocated algorithm (where the number of transmitters is always equal to the total number of antennas in the array). Since the transmitters transmit sequentially, one after the other, fewer transmitters means faster imaging time. The single transmitter MIMO algorithm is the fastest, requiring just N_f bursts from the single transmitter to capture the entire scene.

Since the Doppler algorithm requires many time samples to be captured at each CW frequency, the data collection time is the nominal imaging time for the base imaging algorithm, multiplied by the number of time samples collected. However, if very slow velocities are to be measured (and hence small Doppler shift frequencies), frequency and transmitter interleaving can be used so that the array is not idle between time samples. In this case, the time required to image the scene is usually determined by the period of the lowest Doppler frequency that must be measured.

The computational complexity of the colocated algorithm, the single transmitter algorithms and the X-MIMO algorithm is dominated by the 3-D inverse fast-Fourier transform (IFFT). This IFFT is performed at the end of the algorithm to transform the data from the (k_x, k_y, k_z) domain to the spatial (x, y, z) domain.

The computational complexity of the N-TX M-TX MIMO algorithm is usually dominated by the 4-D FFT that is performed just after capturing the data. This 4-D FFT makes the N-TX M-TX MIMO algorithm the most computationally-expensive. The exception is when the size of either the transmitting or receiving array is very small, in which the final 3-D IFFT will again dominate. Regardless, this MIMO algorithm still collects the largest amount of samples.

Since the Doppler algorithm runs the base imaging algorithm once for each measured velocity, the total computation time is the time for the base imaging algorithm multiplied by the number of time samples collected.

In summary, if array footprint is important, then the colocated RMA will produce the highest resolution images for a given array extent (size). However, if minimizing the required number of antennas is more important for cost reasons, then the X-MIMO algorithm is a better option. The X-MIMO algorithm uses just $2N$ antennas (versus N^2), but at the loss of half the image resolution. Finally, the single transmitter MIMO algorithm images the scene the fastest, resulting in the highest video frame rate, but again with only half the image resolution. Therefore, the system designer needs to consider all the application requirements before selecting the algorithm that is best suited for the imaging task.

Physical room containing moving objects

For each antenna:
1. Transmit single frequency
2. Record reflections at neighboring antenna *over many time samples*
3. Repeat for 64 frequencies

Repeat for each antenna

4D array $s(x_a, y_a, \omega, t)$
[array X dim. × array Y dim. × num freqs × num time samples]

1D FFT w.r.t. time
$(x_a, y_a, \omega, t) \rightarrow (x_a, y_a, \omega, \omega_d)$

Interpolate from Doppler-shift-space to velocity-space
$(x_a, y_a, \omega, \omega_d) \rightarrow (x_a, y_a, \omega, v)$

Regard 4D matrix as stack of 3D matrices
$s(x_a, y_a, \omega, v) \rightarrow s_i(x_a, y_a, \omega)$

Run RMA on each 3D matrix
$s_i(x_a, y_a, \omega) \rightarrow f_i(x, y, z)$

At this point, a set of 3D images is generated, one for each possible velocity

For each voxel:
Take max over all 3D images

max value

argmax

3D image of room **Velocity map of room**

Figure 2.5: The Doppler RMA for generating both 3-D images and velocity maps

Chapter 3

Experimental Setup for Evaluation of Microwave Imaging Algorithms

The previous chapter introduced the range migration algorithm (RMA) and its variants. While researching these imaging algorithms, it was found that little attempt has been made thus far to characterize the performance of the algorithms in a real-world setting. Most publications on 3-D RMA either just perform simulation [24], do no analysis of the experimentally-obtained images [19] [25] [22], or just provide a brief analysis of the resolution of one or two images [1] [3].

The next two chapters will therefore attempt to characterize the performance of different variants of the 3D RMA in the real world, experimentally analyzing the effect that transmit power, array size and configuration, and transceiver component selection have on image resolution and quality. This chapter focuses on the design of a generic microwave imaging testbed that can be used to evaluate and compare these algorithms in an objective manner.

3.1 Physical Infrastructure

3.1.1 Array of antennas

It will be shown in the next chapter that an array containing at least 64×64 antennas is required to image a human hand at sufficient resolution for gesture recognition. While a fixed 2D antenna array of 4096 antennas could have been built, it would have been difficult to vary the antenna array size, antenna spacing and transmitter/receiver placement to determine the resulting effect on image quality. Furthermore, building such an array would have been expensive and risky at the beginning of this research endeavor. A more flexible approach was therefore taken.

Since the range-migration algorithm does not perform analog beamforming, but instead digitally combines the recorded reflections from each antenna in post-processing, just a single transmit antenna and a single receive antenna is used. These two antennas are mechanically

scanned across a 2D aperture, using a XY table as shown in Figure 3.1, to emulate a 2D
antenna array. For the colocated RMA, the antennas are placed in a single antenna housing
and moved together, while the two antennas are moved independently of each other for the
other RMA variants. Both configurations are shown in Figure 3.2.
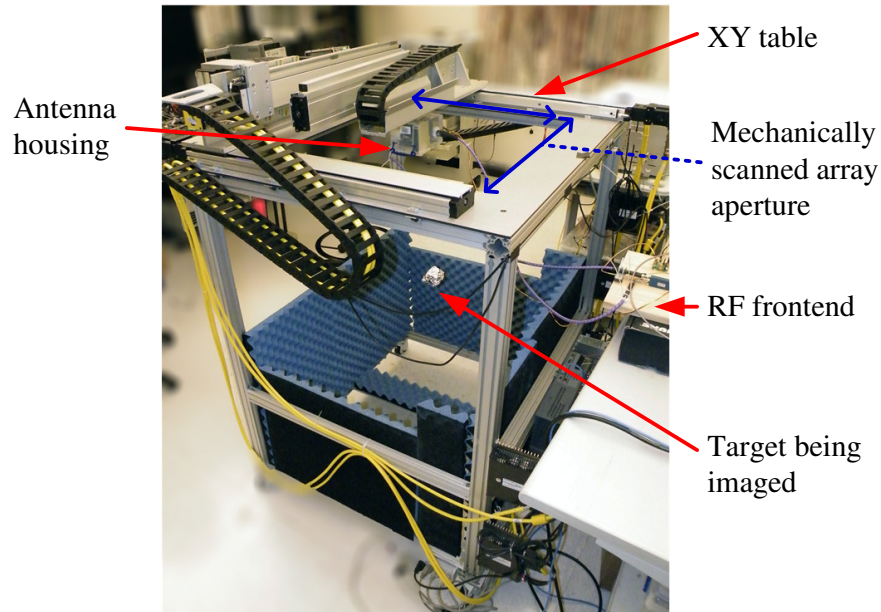
Figure 3.1: The XY-table and antenna setup used for imaging experiments.

For most experiments, a 80x80 array was emulated, requiring the antennas to be moved
through 6400 different discrete positions. The objects being imaged are placed beneath the
antennas. The XY table and antenna configuration is illustrated in Figure 3.3. Once the
antennas have been moved to all the virtual antenna positions and the reflections recorded,
the image reconstruction algorithms process the data. While this approach does have the
limitation that the scene cannot change as the antennas move from one position to another,
this would obviously not be the case for a real system. It must be emphasized that the
real system is envisioned to consist of thousands of antennas placed in optimum locations
rather than having just two antennas mechanically scanned between the antenna locations.
The advantage of the testbed is that it allows any planar antenna array configuration to be
emulated without rebuilding the array.

To enable the imaging of moving objects, a linear actuator is mounted vertically beneath
the antennas. The linear actuator allows objects to be moved in a precisely repeatable way for
each antenna position. The linear actuator moves objects at a predetermined velocity while
the RF reflections are recorded at the antennas, which are kept stationery. The antennas
are then moved to the next position within the 2D array, the object is moved back to its
original position, and the next set of samples are recorded. While this method is slow, it
does allow accurate characterization of the Doppler algorithm.

<div align="center">(a)   (b)</div>
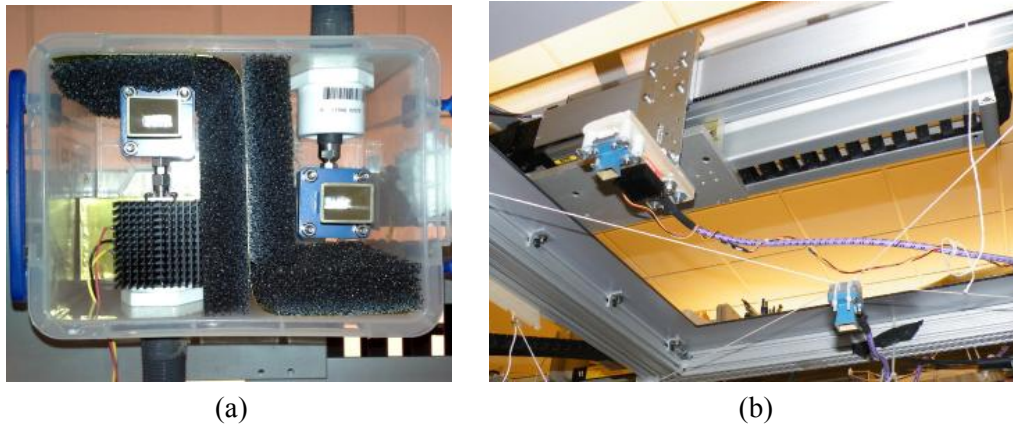
Figure 3.2: (a) The antenna housing for the colocated experiments, as viewed from the underside. The receiving horn antenna and low-noise amplifier are on the left of the housing, while the transmitting antenna is on the right. The horn antennas are painted blue. (b) The placement of the horn antennas for the single-transmitter experiment, as viewed from beneath the XY table. The transmitting horn antenna is fixed in the center, while the receiving horn antenna scans across the 2D aperture.
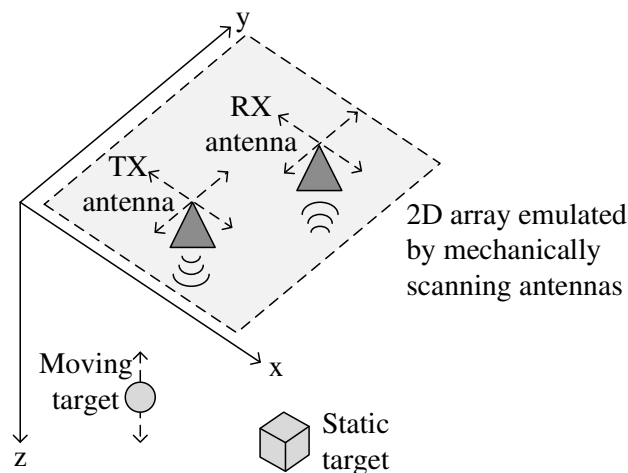
Figure 3.3: The testbed configuration. Both the TX and RX antenna are moved around in the XY plane to emulate a large 2D antenna array.

3.1.2 RF frontend

The RF frontend is a simple direct-conversion receiver circuit, built from commercial off-the-shelf modules. Figure 3.4 shows a photo of the frontend, with the accompanying circuit diagram in Figure 3.5. While the signal generator that drives the frontend can be used to generate a chirp and hence transmit all desired frequencies simultaneously, the testbed transmitter instead operates in stepped continuous wave (CW) mode. In this mode, the

received signal that reflects off objects in the scene is of the same frequency as the transmitted signal, resulting in a 0 Hz (i.e. DC) baseband signal. Since an I/Q mixer is used, both the amplitude and phase of this DC signal can be measured with low sample-rate ADCs.
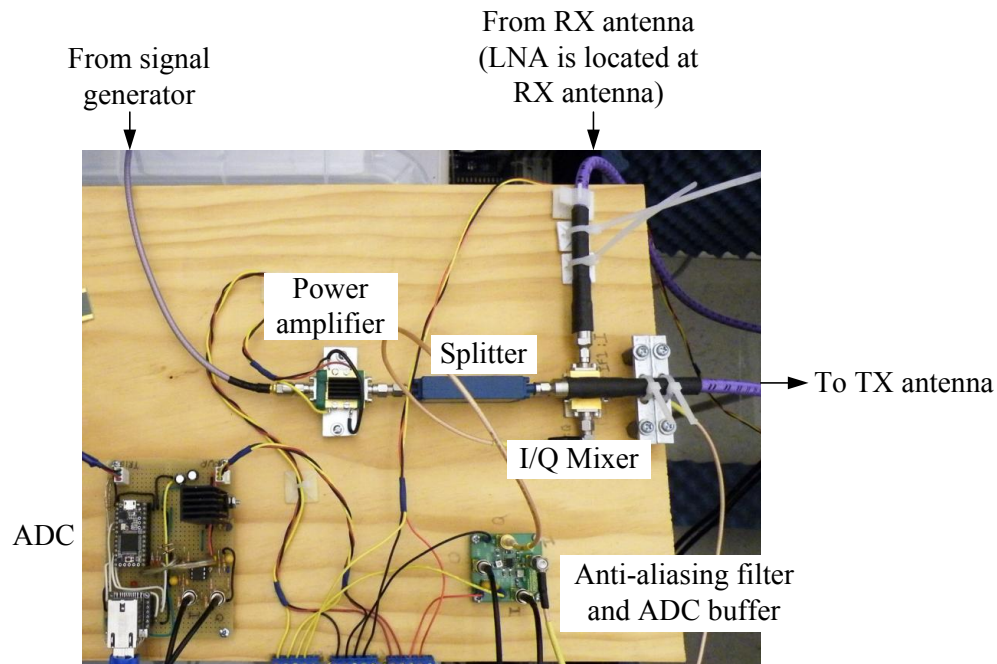
Figure 3.4: Photo of the RF transceiver frontend, built from commercial modules
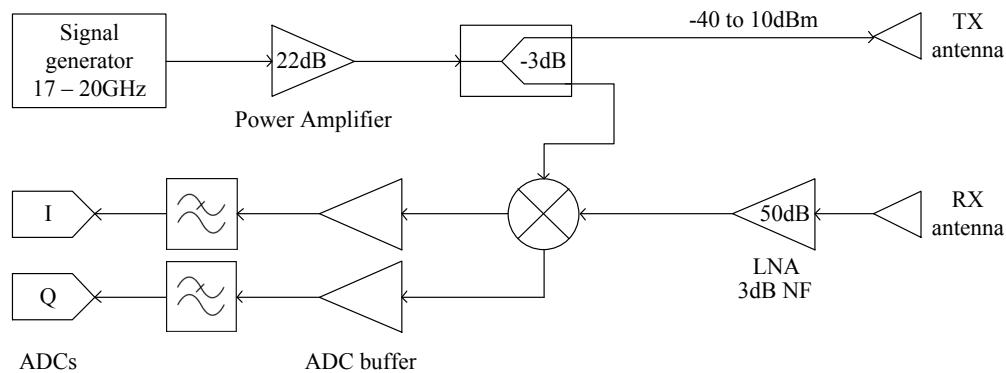
Figure 3.5: Circuit diagram of RF transceiver frontend

The main advantages of this design are that (a) it allows the magnitude and phase of the reflected signal to be directly measured without further post-processing (b) a very simple RF frontend and slow ADCs can be used. Having a simple RF frontend circuit is important, as it will allow the frontend to be cheaply and easily integrated onto a single chip in the future. The disadvantage of this design is that the signal is mixed down to DC and hence is

susceptible to flicker noise. Fortunately, due to the large size of the antenna array, most of the flicker noise averages out in the imaging algorithm.

The performance specifications for the RF frontend are:

- Operating frequency: 17 to 20 GHz

- Transmit power: Variable from -40 dBm to +10 dBm

- Receive gain: 40dB (LNA gain less cable and mixer losses)

- Receive noise figure: 3dB (the receiver noise figure is dominated by the LNA, due to the high gain of the LNA)

3.2   Design of Antennas for Microwave Imaging

While the RF frontend generates the RF signals, antennas are required to actually illuminate the scene with the signal and capture the reflected waves. Three different antenna designs were evaluated to determine their effect on image quality: a horn antenna, a patch antenna and a Vivaldi antenna.

The main requirements for the antennas are:

1. Low-cost: a large number of antennas are required, and so keeping the cost of each antenna low is important to reducing overall system cost

2. Wide bandwidth: as will be shown later, depth resolution is directly proportional to RF bandwidth

3. Wide beam angle: a single transmitting antenna needs to be able to illuminate the entire scene
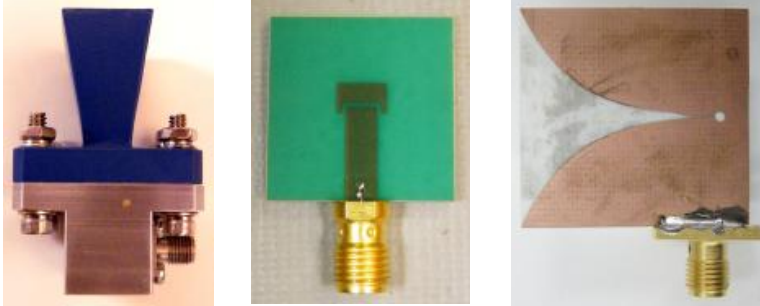
The horn is the only commercial antenna; the patch and Vivaldi antennas are simple PCB antennas that can be fabricated at extremely low cost. These last two antennas were custom designed for the testbed using Ansys HFSS[1] software. The parameters of these three antennas are summarized in Figure 3.6, and will be discussed further in the next few sections.

3.2.1   Horn antenna

A 10 dB standard gain horn antenna was used as a reference antenna. Although commercial horn antennas are not low-cost, they are wide bandwidth and do have good, well-known beam pattern characteristics. The horn antenna was therefore used as a reference antenna against which the other antennas were compared.

While higher gain horn antennas were available, the horn with the lowest gain was purchased, as it provided the widest beamwidth (55°).

---

[1]http://www.ansys.com/products/electronics/ansys-hfss

	(a)	(b)	(c)
Frequency Range (GHz)	15-22	17-19.5	15-20
Gain (dBi)	10	6	7
Return Loss (dB)	20	10	15
Dimensions (mm)	53 x 34 x 34	20 x 24	31 x 30

Figure 3.6: Antennas used in the testbed, along with measured performance parameters: (a) Pasternack PE9853-SF-10 commercial horn antenna (b) low-cost PCB patch antenna (c) low-cost Vivaldi antenna

3.2.2 Patch antenna

A patch antenna consists of a rectangular patch and ground plane, typically on opposite sides of the same PCB, with a dielectric in between. If a custom PCB is to be built for the RF frontend, then the patch antenna can be incorporated into this PCB at negligible additional cost. While FR4 is a common glass-fiber dielectric used in many PCBs, the glass fibers can cause spatial variations in the dielectric constant of the board, making it less suitable for high-frequency applications [26]. The PCB patch antenna was therefore designed using Rogers RO4003C, a low-cost woven-glass/ceramic hybrid dielectric.

The patch antenna was designed in Ansys HFSS, a 3-D high-frequency electromagnetic field solver, as shown in Figure 3.7. The patch antenna was designed to operate in the 17 to 22 GHz band, as this is the bandwidth of the RF frontend circuit. Although the radiating patch element is only 3.2 mm long and 5.3 mm wide, the antenna PCB is significantly larger to accommodate the feeding trace and SMA connector.

Since the impedance at the edge of a patch antenna is usually quite large (188 Ω in this case), and most RF components and cables have 50 Ω characteristic impedance, feeding a patch antenna can be difficult. An attempt was made to use a quarter-wave impedance transformer to match the two impedances, but this resulted in very limited bandwidth. Fortunately, the input impedance of a patch antenna decreases as one moves from the edge of the antenna towards the center. Therefore, the feed was inset by 0.7 mm to ensure 50 Ω matching. Bandwidth was further improved by capacitively-coupling the feed trace to the patch at this inset point [27], using a small gap of 0.4 mm.
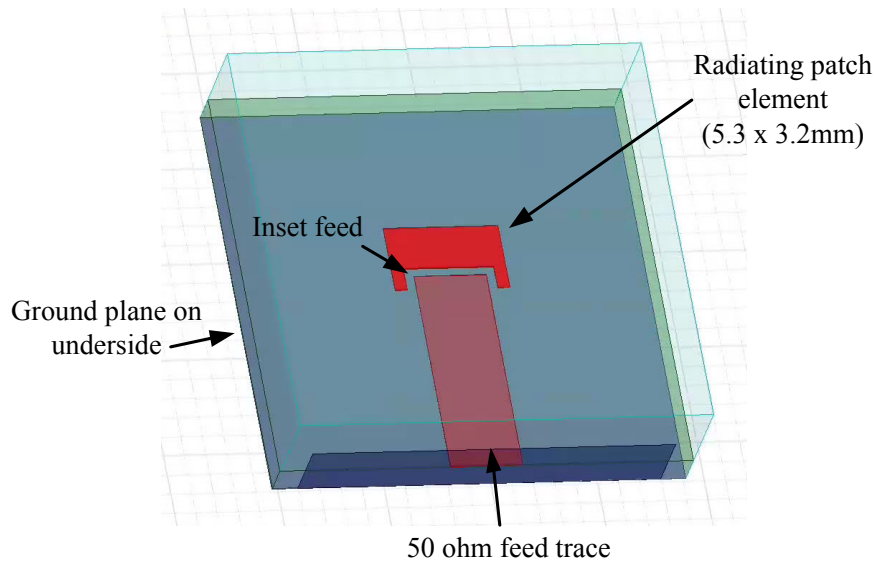
Figure 3.7: Model for the patch antenna design in HFSS
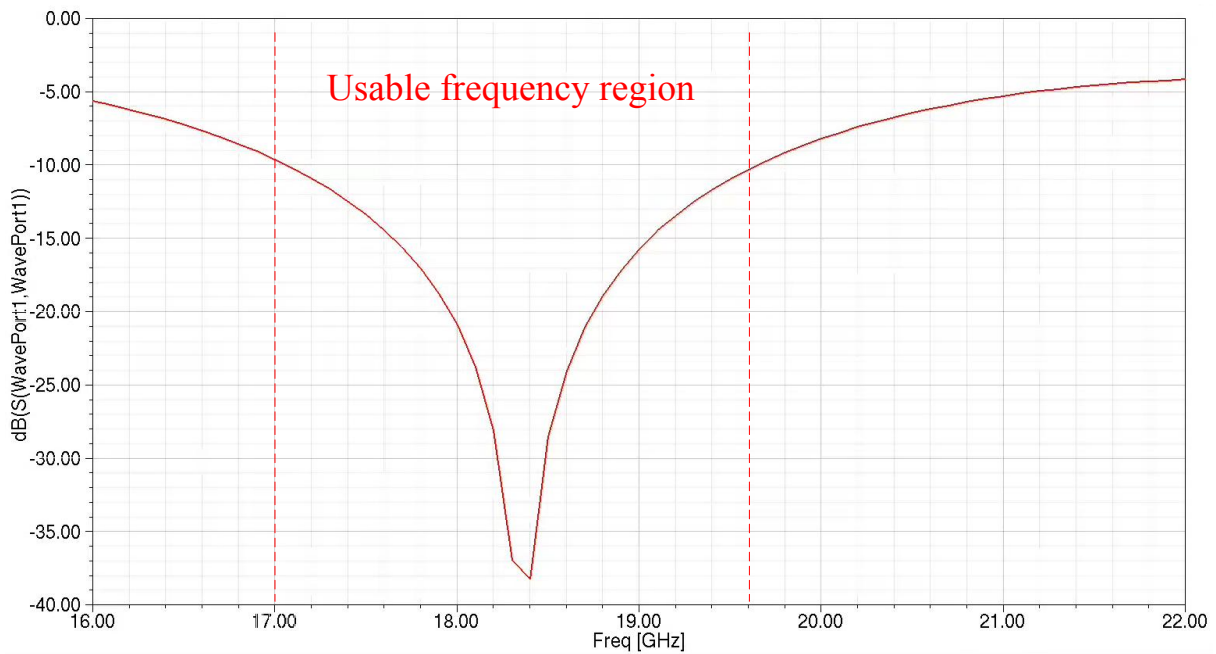
Figure 3.8: Simulated S11 (return loss) for the patch antenna. The antenna is tuned to
18.4 GHz with a 2.6 GHz bandwidth.

The patch antenna was fabricated by a commercial board house. Figure 3.8 shows that
the S_{11}(i.e. return loss) is better than 10 dB from 17 GHz to 19.6 GHz, resulting in a 2.6
GHz bandwidth. Figure 3.9 shows the simulated beam pattern in E- and H-planes. Note

that patch antennas are broadside radiators, meaning that the peak radiation is normal to
the PCB surface. This figure shows that the 3dB-beamwidth exceeds 75° in both planes,
which is one of the main advantages of patch antennas.
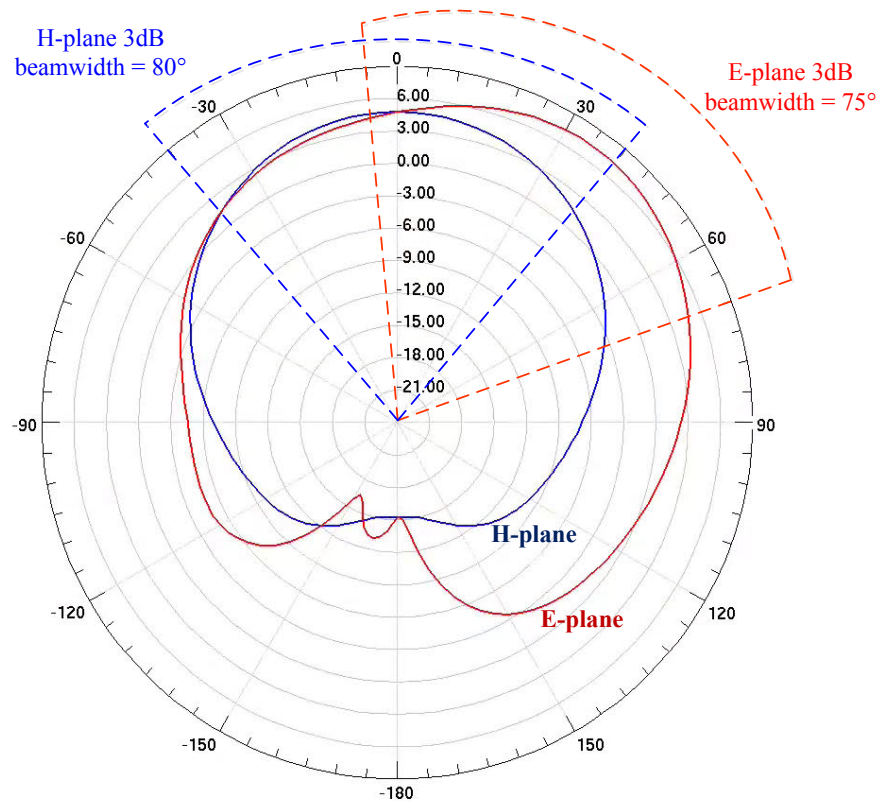
Figure 3.9: Simulated beam pattern for the the patch antenna. The red curve indicates the
beam pattern along the E-plane (i.e. parallel to the feed), while the blue curve indicates
the beam pattern in the H-plane (i.e. perpendicular to the feed direction).

The phase center of an antenna is the *apparent* source of the radiation. If an antenna
transmits a continuous wave, the wave should have the same phase at all points on a sphere
that is centered on the antenna phase center. The phase center error refers to how much
the measured phase varies, depending on the direction of measurement. Alternatively, it can
be regarded as the asymmetry in the phase response of the antenna. Microwave imaging
relies on measuring the phase distance from the phase center of the antenna to each point
in the scene. Therefore, it is important that the phase center error is as small as possible,
otherwise it will introduce errors into the measurements. One concern with patch antennas
is that they typically have large phase center errors due to the fringing fields [28] [29]. The
standard deviation of the phase center error of this patch antenna was simulated and found
to be 37°, which is of some concern.

3.2.3   Vivaldi tapered slot antenna

Due the concerns regarding the limited bandwidth and phase center variation of the patch
antenna, a second PCB antenna was also designed. The Vivaldi antenna is a type of tapered
slot antenna that typically has very large bandwidth [30]. It can also be simply manufactured
from a two-layer PCB. Figure 3.10 shows the Vivaldi antenna that was designed in HFSS
specifically for microwave imaging. The tapered slot is the gap on the top layer between the
copper conductors.

The Vivaldi antenna is fed by a 50 Ω microstrip trace on the bottom layer. When this
trace crosses the slot in the top layer, the energy couples to the slot through the dielectric.
The feed trace is terminated with a radial stub.

On the top layer, the wave, which has been coupled to the narrowest part of the slot, now
propagates along the widening slot until the slot is half a wavelength wide. At this point,
the wave begins to radiate [31]. The taper is therefore divided into a propagation zone and
a radiation zone.

Vivaldi antennas are end-fire antennas, as the radio wave radiates from the edge of the
PCB where the slot is widest. The peak gain is in the plane of the PCB and in the direction
of the taper, rather than normal to the PCB, as was the case with the patch antenna.

The antenna shown in Figure 3.10 uses an exponential taper profile. It has been shown
that the taper profile has a strong influence on gain, beamwidth and bandwidth [32]. This
taper was therefore carefully tuned to give the largest bandwidth and beamwidth. The
tapered slot is 24 mm long. It is 0.15 mm wide at the narrowest point, broadening to 30 mm
at the PCB edge.
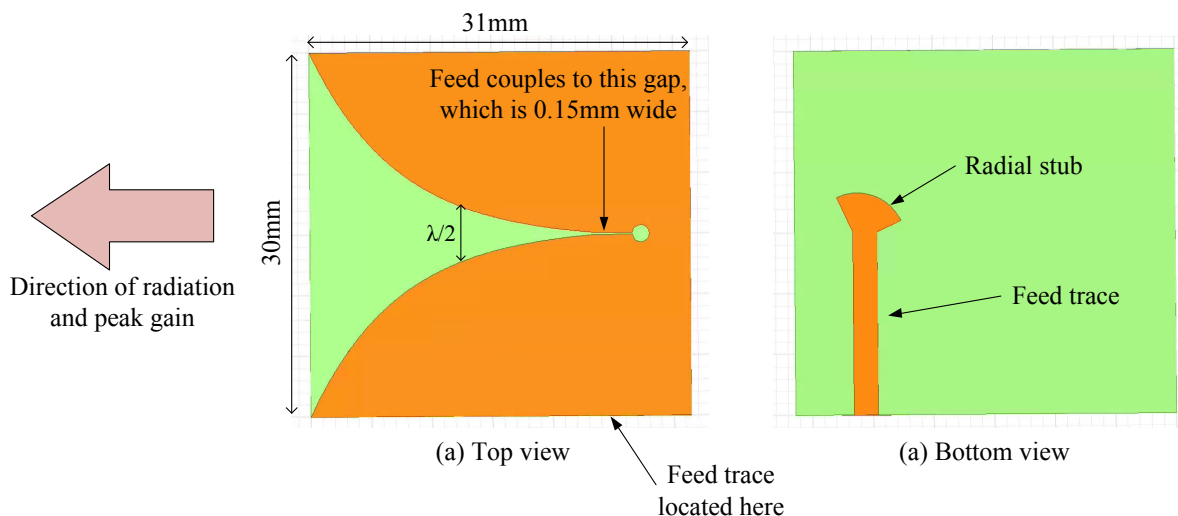
Figure 3.10: The HFSS model for the Vivaldi antenna. Green indicates PCB dielectric,
while orange indicates copper.

Figure 3.11 shows that the simulated return loss is better than 10 dB from 4.5 GHz to
21 GHz, resulting in a very large 16.5 GHz bandwidth. In the 17 to 20 GHz region in which

the antenna will be operated, both the return loss exceeds 14 dB. Figure 3.12 shows that the antenna has a peak gain of 6dB and a 3dB-beamwidth of 60°. To help better visualize the beam pattern, Figure 3.13 shows the gain pattern superimposed onto the 3-D model of the antenna. The red region indicates the direction of highest gain.
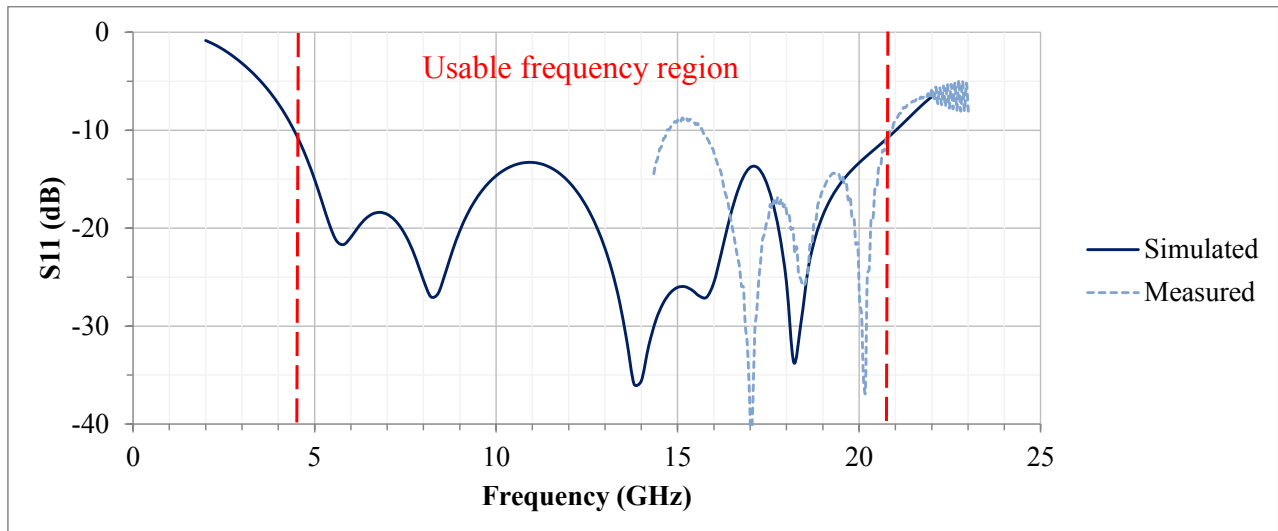
Figure 3.11: Simulated and measured S11 (return loss) for the Vivaldi antenna. The antenna exhibits a wide bandwidth, from 4.5 GHz to 21 GHz.

After simulating in HFSS, the physical antenna was built by milling it from a sheet of copper-clad Rogers RO4003C dielectric material. While this could have been done by a PCB house, it was much faster to do this using a small bench-top computer-controlled mill. The finished antenna is shown in Figure 3.6, while Figure 3.11 shows that the measured return loss meets or exceeds the simulated return loss in the 17 to 20 GHz band of interest. It is only below this band that the performance of the fabricated antenna was worse than simulation, most likely due to the low accuracy of the milling machine.

3.3   Characterization Phantoms and Metrics

While the experimental setup described thus far will allow objects to be imaged, the effect of transmit power, array configuration and choice of RMA on image quality needs to be characterized. Standardized imaging phantoms were therefore created to allow direct comparisons between different imaging configurations. The resulting images are evaluated using two metrics: image resolution and image signal-to-noise ratio (SNR).

3.3.1   Standard imaging phantoms

A brass phantom consisting of a set of metal strips with decreasing spacing, as shown in Figure 3.14(a), was used to measure image resolution. The resolution of the imaging system
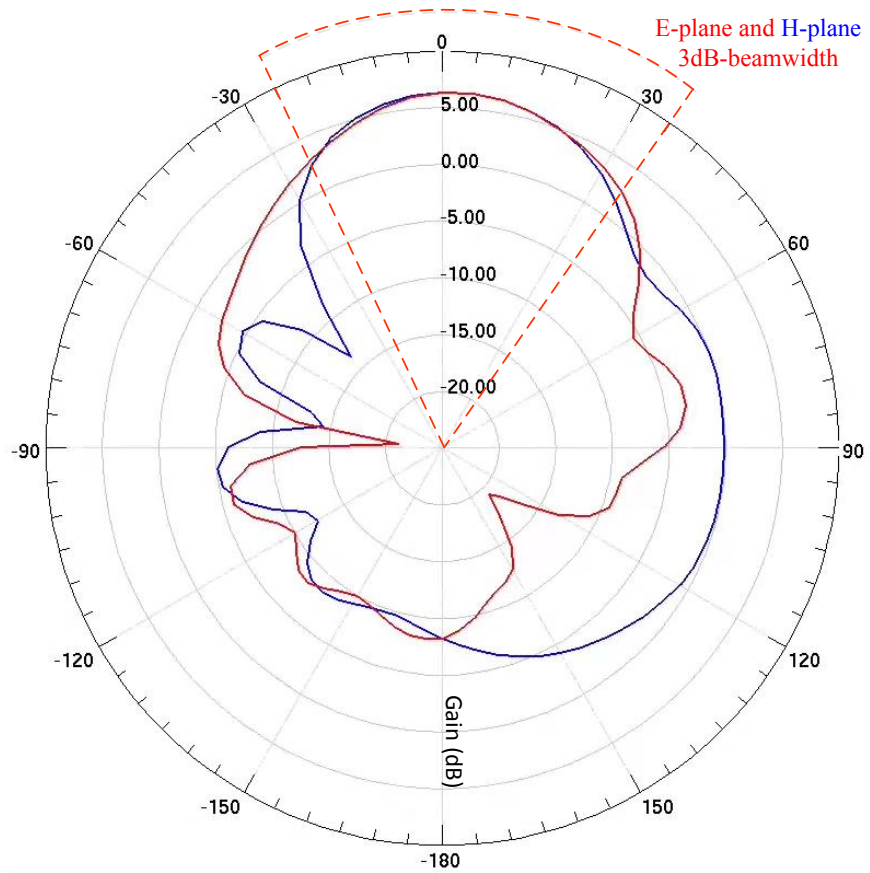
Figure 3.12: Simulated antenna radiation pattern for the Vivaldi antenna. The red plot
shows the antenna gain in the H-plane, while the blue plot shows the gain in the H-plane.
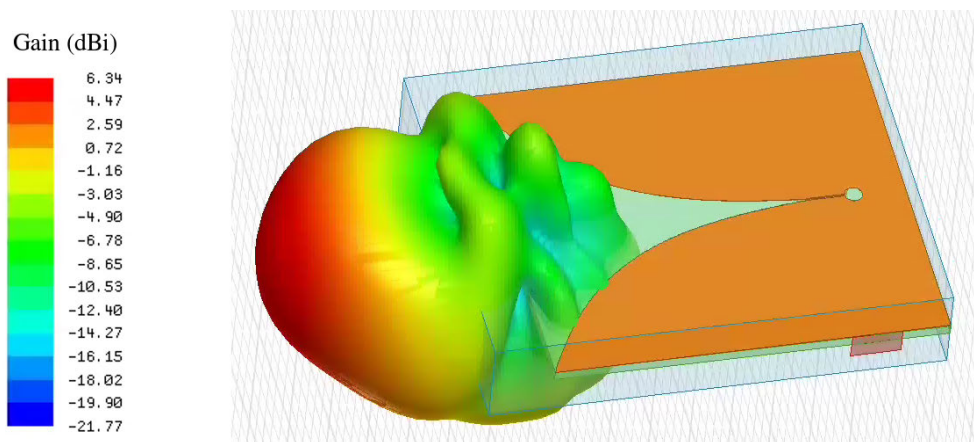
Figure 3.13: 3-D beampattern simulation for the Vivaldi antenna. Red indicates the
direction of highest gain.

is easily found by determining the smallest space between strips that can be resolved in the captured images. A similar phantom was built using strips of pig skin to determine if object material affects image quality.

To evaluate the usefulness of these microwave imaging systems for hand gesture recognition, a human hand phantom was also created. A phantom was used in place of a live hand due to the many hours that the imaging testbed takes to capture a single image. Furthermore, the hand phantom ensures repeatability and prevents unwanted motion during imaging. The hand phantom, also shown in Figure 3.14, was created using a layer of pig muscle, covered with a thin layer of pig fat and finally covered with pig skin. The entire stackup was then cut out in the exact shape of a statistically average-sized human hand.

Pig tissue was used due to its similarity to human tissue. To be completely accurate, the blood vessels and bones should also have been included. However, HFSS simulations showed that the blood vessels are too small to have any effect on the images, while the overlying layers of fat and muscle attenuate most of the signal before it reaches the bone. Therefore, omitting the bone and blood vessels had minimal effect on the results.

(a)   (b)   (c)
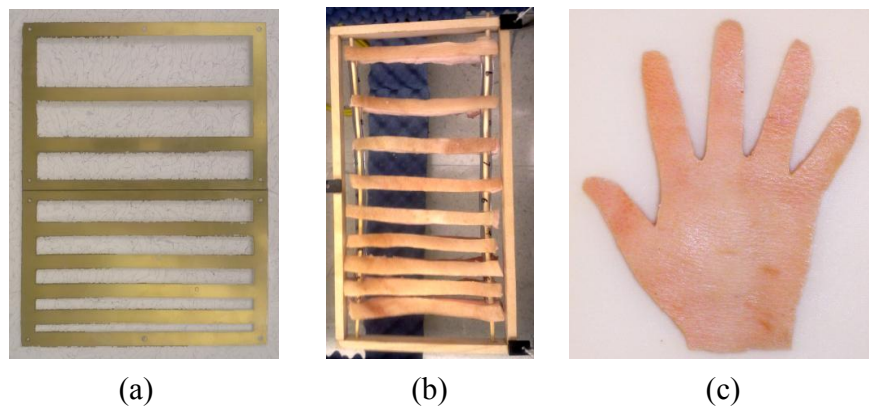
Figure 3.14: Standard imaging phantoms. (a) Brass resolution phantom (b) Skin resolution phantom (c) Human hand phantom

3.3.2   Calculation of imaging performance metrics

After imaging the phantoms, the image resolution and image SNR of the resulting images is calculated. The technique for measuring image resolution was described above. To precisely determine if two closely spaced metal strips are resolvable, the 50% amplitude criterion was used, i.e. the intensity of the voxels representing the metal strips must be at least double the intensity of the voxels representing the gap between the strips.

The SNR of the images was calculated using [33]

$$SNR_{image} = \frac{\mu_{object} - \mu_{bg}}{\sigma_{bg}} \tag{3.1}$$

where μ_{object} is the average intensity of the voxels containing the object of interest, μ_{bg} is the average intensity of the background, and σ_{bg} is the standard deviation of the background. Since the image SNR is an intensity ratio, typically between 1 and 50, and not a power ratio, it is not usually given in decibels. Note that the numerator is simply the contrast between the object of interest and the background. A simple adaptive thresholding operation was used to separate the object voxels from the background voxels, for the purpose of this calculation.

3.4 Conclusion

The imaging testbed, imaging phantoms and image quality metrics outlined in this chapter will allow different antenna array and RF circuit configurations to be compared. Furthermore, it will also allow the quality of the images produced by the different RMA variants to be characterized.

Three different antennas were also described, and their effect on resulting image quality will be characterized in the next chapter. While the horn antenna is too expensive to be used in a large antenna array, it does provide a good reference. The patch antenna provides the widest beamwidth (75°), but has less than 3 GHz bandwidth and large phase center variations. The Vivaldi antenna has a slightly narrower beam (60°), but many GHz of bandwidth. The next chapter will determine which antenna is the best fit for microwave imaging.

Chapter 4

Characterization Results

The algorithms outlined in Chapter 2 are evaluated using the testbed described in the previous chapter. In particular, the effect of antenna array size and pitch; RF transmit power and bandwidth; antenna design; and target material on image resolution and SNR is characterized for each algorithm.

Unless stated otherwise, most results were obtained using the following testbed configuration:

- Two horn antennas were mechanically moved on the XY table to emulate an array of 80×80 antennas

- The horn antennas were moved in increments of 5 mm $(\frac{\lambda}{3})$, emulating an array with 5 mm antenna pitch

- The transmitter stepped from 17 to 20 GHz, in 23.4 MHz steps

- The metal resolution phantom was imaged at a distance of 0.5m from the antenna array

Figures 4.1 and 4.2 show typical 3D images that these algorithms are able to produce, for both stationary and moving objects.

4.1   Effect of RF Transmit Power and RMA Variant

Figure 4.3 shows the influence of RF transmit power on image SNR. Note that image SNR is given as a ratio, rather than in decibels. With an image SNR of 10 being the lowest usable image quality, it was found that all three imaging algorithms were able to produce usable images at transmit powers as low as -30 dBm. Below -30 dBm, the images were no longer recognizable. Increasing transmit power causes a correlated increase in image SNR, until saturation.
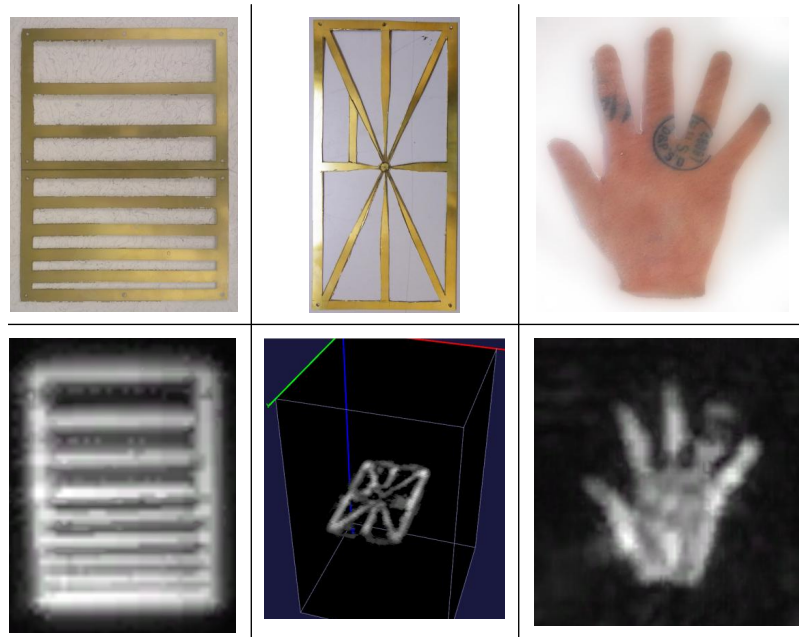
Figure 4.1: *Top left:* brass phantom used for resolution experiments. *Top center:* another brass imaging phantom. *Top right:* human hand phantom. *Bottom row:* 3D microwave images of the phantoms, shown either as a 2D image using maximum intensity projection (*left* and *right*) or as a 3D image (*center*).
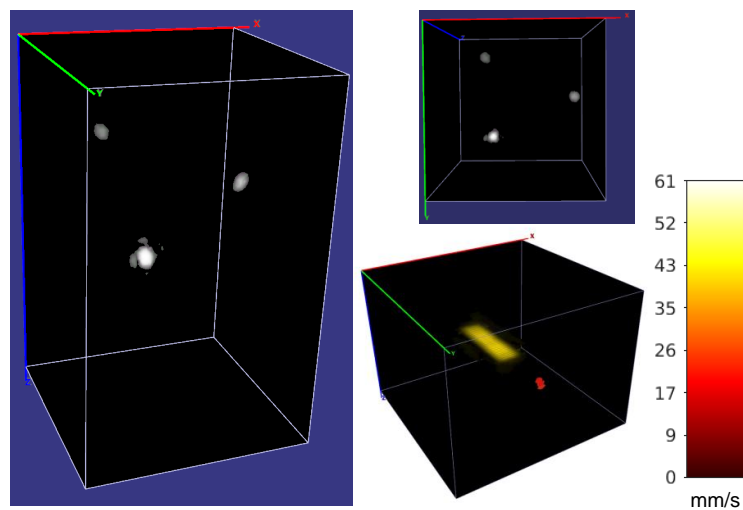
Figure 4.2: 3D microwave images generated by the testbed. *Left:* microwave image of three 40 mm diameter balls, placed 400 mm apart in an equilateral triangle arrangement. *Top right:* Top view of the three balls. *Bottom right:* A 3-D Doppler image of a rectangular metal plate and a smaller aluminum ball, moving up at 45 mm/s and 20 mm/s respectively.

The single-transmitter MIMO algorithm produced the highest image SNR for a given transmit power, due to the object being imaged always lying within the main gain lobe of the centrally-located transmit antenna. Although the Doppler and colocated algorithms produced similar image SNR results, the Doppler algorithm performed slightly better due to the additional time samples collected.

Figure 4.4 shows that transmit power has little to no influence on image resolution, provided that the minimum image SNR was met. This result is expected, as resolution is determined primarily by array aperture and not transmit power. Both the colocated and Doppler algorithms delivered an average resolution of 12.5 mm over the power range, closely matching the 10 mm theoretical resolution provided by an array of this size (see Table 2.1). The single transmitter algorithm provides a resolution of 20 mm, as expected due to a smaller effective aperture of having only one transmitter. The theoretical resolution is also 20 mm in this case.

The N-TX M-RX MIMO algorithm was tested with a small number of transmitting antennas and performed identically to the single-transmitter algorithm, again as predicted by the theory; hence, its curve is not shown. Due to time constraints, the X-MIMO algorithm was only characterized at a single transmit power level, -3 dBm. At this power level, the X-MIMO algorithm produced images with a resolution of 20 mm (as predicted by Table 2.1) and a SNR of 36. This SNR lies between that achieved by the colocated and single transmitter algorithms.

With the target sitting 0.5 m in front of the array, 12.5 mm resolution translates to 1.4° angular resolution, while 20 mm resolution translates to 2.3°.
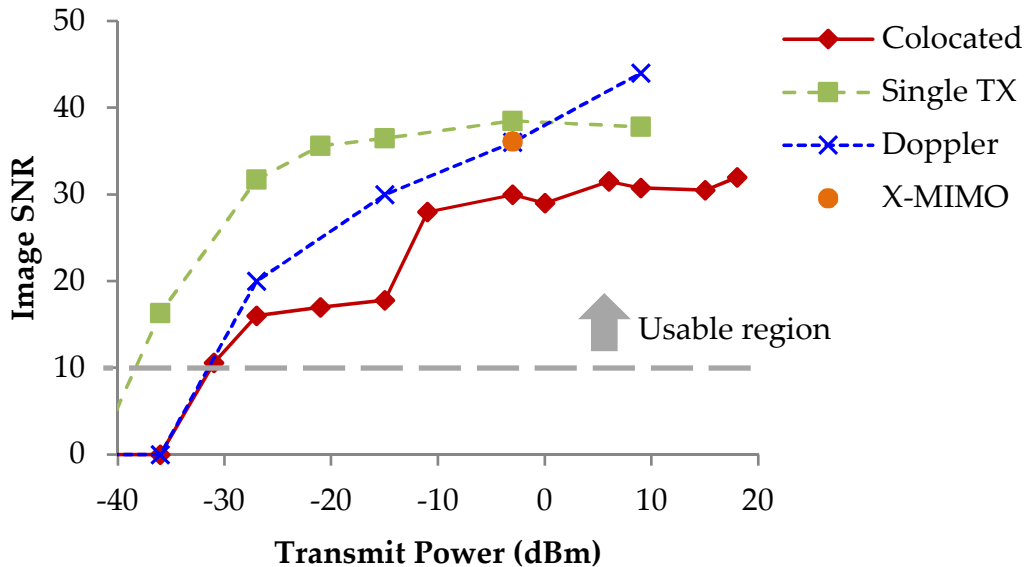
Figure 4.3: Increasing transmit power improves image SNR for all RMA algorithms

The colocated algorithm provides slightly better resolution at transmit power levels above 0 dBm than below, which was not expected. At power levels above 0 dBm, the image is
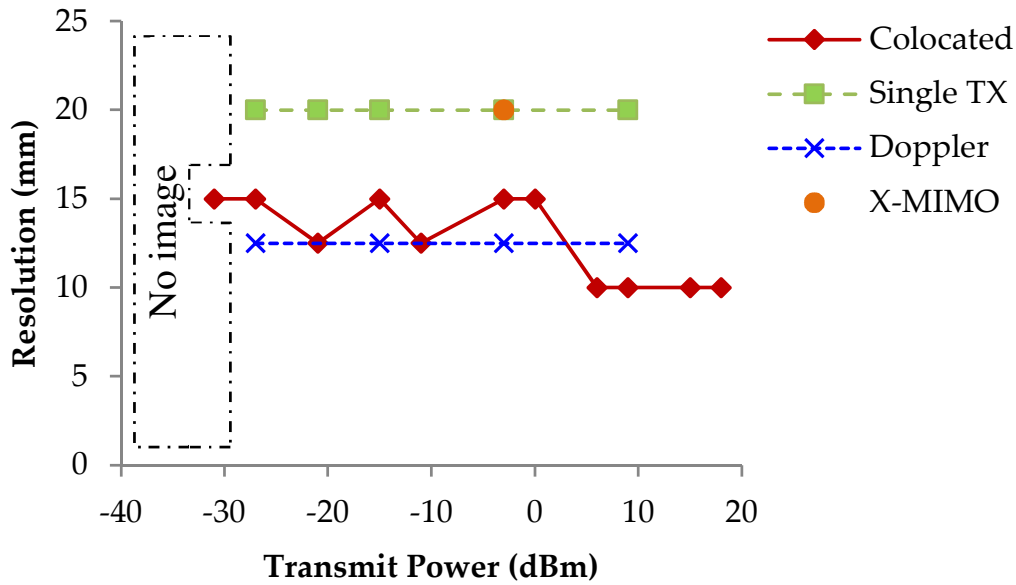
Figure 4.4: Comparison of the image resolution achieved by the different RMA algorithms as the transmit power is varied

essentially noise free. Once power drops below 0 dBm, image starts becoming noisier (see Figure 4.3). This additional noise means that the 10 mm slit in the brass resolution phantom, which was previously barely resolvable, can no longer be resolved, decreasing effective image resolution. Note that the resolution provided by the antenna aperture remains constant, but the apparent resolution in the final images degrades from the theoretical best.

4.2 Effect of Size of Antenna Array

The size of the 2-D antenna array (i.e. number of antennas per side) has the largest influence on the quality of the three-dimensional images, as shown in Figure 4.5. The theoretical curve was derived from Equation 2.29 in Chapter 2 for the colocated RMA.

At small array sizes, the resolution is directly proportional to the array size. At larger array sizes, the resolution becomes limited to half the RF wavelength, due to diffraction limits. At 20 GHz, this half wavelength limit is 7.5 mm. It should also be noted that the measured resolution matches well with the theory.

It was mentioned in Chapter 1 that this dissertation will focus on using microwave imaging to image people within a room, specifically for 3-D positioning and hand gesture recognition applications. In these cases, a resolution of 10 mm or less is required to resolve individual human fingers for gesture recognition. Figure 4.5 therefore indicates that an array of at least 60×60 antennas is required.

In terms of image SNR, increasing the array size results in a nearly proportional increase in image SNR. This increase in image SNR occurs because larger arrays provide more noise
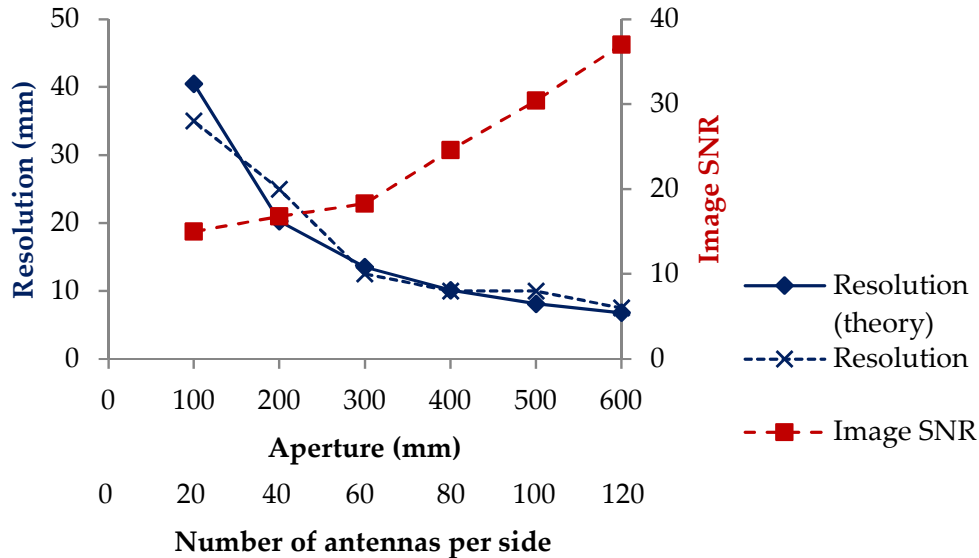
Figure 4.5: The influence of antenna array size on image quality, with a fixed 5 mm antenna pitch

reduction through averaging.

All these array size measurements were made using a transmit power of 6 dBm. Even though the colocated RMA was used to generate the data in Figure 4.5, the same trends were seen for all the RMA variants.

4.3   Effect of Antenna Spacing

Uniform antenna arrays are conventionally built with antennas placed half a wavelength $\left(\frac{\lambda}{2}\right)$ or less apart. However, if cost of the array is a concern, Figure 4.6 shows that antennas can be placed up to 0.9λ apart without sacrificing image quality. This increase in antenna spacing allows a larger aperture to be built with fewer antennas.

Once the antennas are placed more than a wavelength apart, the array grating lobes cause aliasing, making image recovery impossible. The amplitude of the grating lobes, relative to the main lobe, averaged over the entire scene and array aperture, was calculated via simulation and is shown in Figure 4.7 for each antenna spacing. The two figures show that even though moderate grating lobes exist at 0.9λ antenna spacing, the imaging algorithm averages them out.

However, if image quality is more important than cost, reducing antenna spacing from $\frac{\lambda}{2}$ to $\frac{\lambda}{6}$ can improve image SNR by up to 33% due to oversampling.
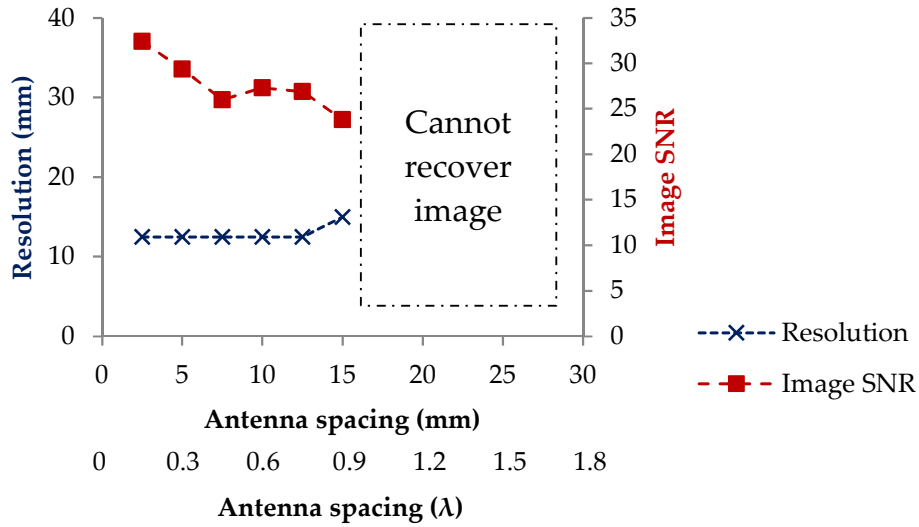
Figure 4.6: Effect of antenna spacing on image quality when aperture is fixed
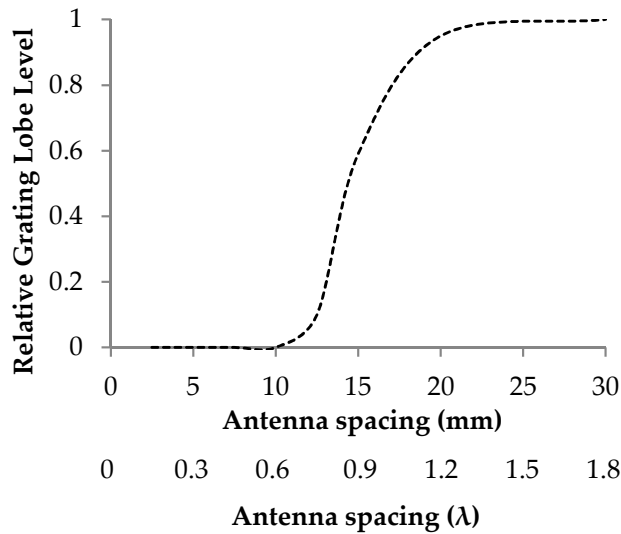
Figure 4.7: Effect of antenna spacing on grating lobes (simulation)

4.4 Resiliency to Defective Antennas

When large antenna arrays are built, it is expected that a small percentage of antennas will fail. It is therefore important that the image quality degrades gracefully with antenna failures. The effect of dead antennas on image resolution and SNR was determined by setting the responses of randomly-chosen antennas to zero. It is important that antenna failures occur randomly, as a regular pattern of failed antennas will cause grating lobes similar to those discussed in Section 4.3.

Figure 4.8 shows that with 30% of the antennas dead, the image resolution increases from 10 mm to 12.5 mm and the image SNR decreases by just 11%. Therefore, provided the system knows which antennas have failed and can zero out their responses, the colocated RMA can tolerate up to 30% antenna failure with minimal effect on image quality. However, above 30% antenna fail rate, the image quality rapidly worsens. When more than 80% of the antennas have failed, images can no longer be formed.
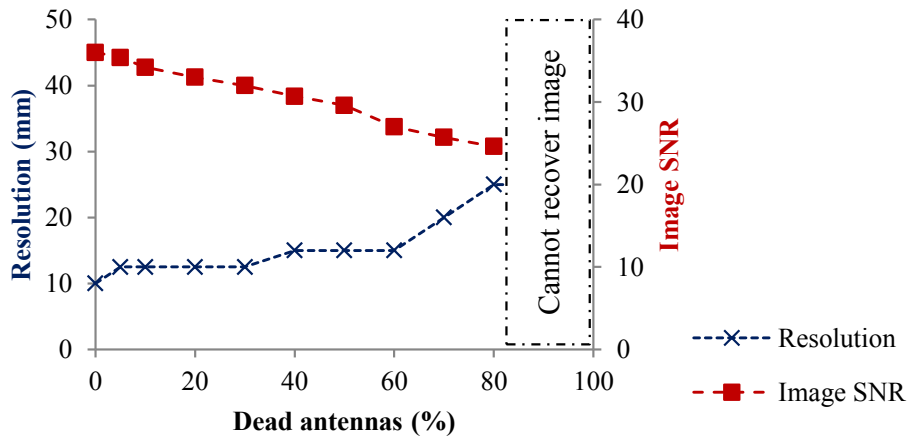
Figure 4.8: Effect of dead antennas on image quality

The single-transmitter MIMO and X-MIMO algorithms exhibited similar failure profiles, with the exception that the lone transmitter in the single-transmitter array must not fail for the system to continue functioning.

4.5   Effect of Antenna Selection

Most of the results presented in this paper were obtained using commercial horn antennas. Since these relatively expensive antennas are not ideal for low-cost imaging systems, custom PCB antennas, which can be manufactured extremely cheaply in volume, were designed and fabricated as an alternative. The three antennas, shown in Figure 3.6, were evaluated and their relative performance is compared in Table 4.1. Since it is the relative performance that is of interest, the results have been normalized to 10 mm resolution and an image SNR of 1.0 for the horn antenna.

There was little variation in image SNR, with the horn images being slightly less noisy. This result is due to the horn having a better return loss than the other two antennas, and hence being better matched to the receiver low-noise amplifier (LNA), giving a higher RF SNR at the receiver. The patch antenna had poor resolution due to the large phase center errors associated with patches [34]. The Vivaldi antenna, however, produced high resolution images due to its wide beamwidth and high return loss over a large bandwidth, making it an excellent candidate for low-cost microwave imaging systems.

Table 4.1: Comparison of different antennas for imaging

Antenna	Norm. Resolution	Norm. Image SNR
Horn	10 mm	1
Patch	15 mm	0.94
Vivaldi	8 mm	0.95

4.6 Effect of RF Bandwidth

It is well known that the depth resolution of the microwave imaging system is given by $\frac{c}{2B}$, where B is the RF bandwidth [3]. Using the imaging testbed, the RF bandwidth was varied from 500 MHz to 3 GHz and the resolution and image SNR measured. The depth resolution measured at each bandwidth matched the theoretical value to within 10%. Furthermore, increasing the number of frequency samples with the bandwidth caused an increase in image SNR.

4.7 Effect of Surface Material

To determine the effect of the surface material of the object being imaged, pig-skin phantoms were also imaged. Figure 4.9 shows that imaging the skin resulted in slightly better image resolution and SNR, when compared with the metallic phantom. This is because microwaves reflect in a diffuse manner off skin, making the reflected signal easier to capture, while the reflection is specular for metallic objects. These results mean that any image quality metric, that was obtained using the brass resolution phantom, will only be improved upon when imaging a human body instead.
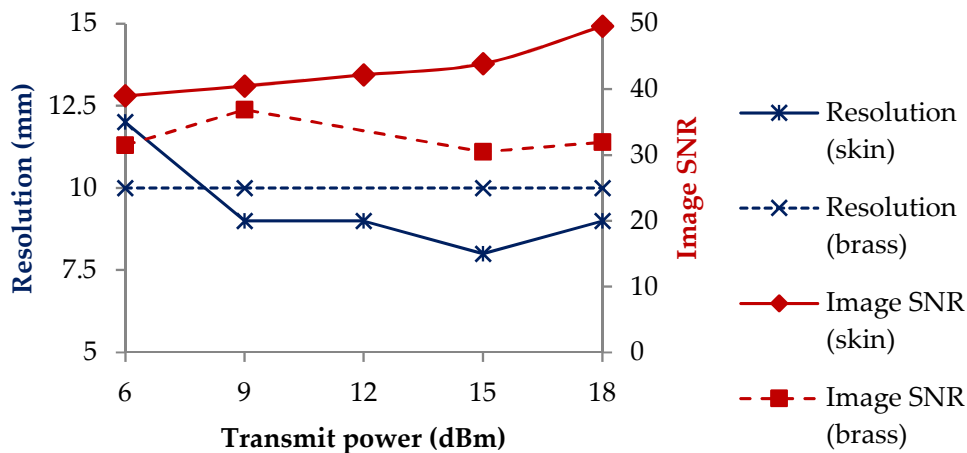
Figure 4.9: Effect of target material on image resolution and SNR

4.8   Effect of Clock Jitter

Since clock synchronization can be challenging in large arrays, the effect of clock jitter on image quality was simulated in software. Each RF clock edge, at each antenna, was delayed or advanced by a random amount of time, selected from a zero-mean Gaussian distribution. It was found that if the standard deviation of the jitter, also known as the RMS jitter, was 20% of the RF clock period (i.e. 72°), just a 12% decrease in image SNR occurred. Since the clock jitter is assumed to be independent at each transceiver, the impact of the jitter is reduced by the averaging effects of the large array, allowing the microwave imaging algorithms to cope with such large clock jitter. However, once the RMS jitter was increased to 40% of the clock period, no image could be recovered.

4.9   Accuracy of Velocity Measurements

The velocity of the linear actuator, used to move objects for the Doppler imaging experiments, was precisely controlled using internal feedback sensors. The accuracy of the velocity measurements, provided by the Doppler imaging algorithm, can therefore be determined by comparing these measurements to the velocity programmed into the linear actuator. The velocity measurements of the Doppler algorithm were found to be accurate within 5% over a range of typical human velocities (40 to 100 mm/s). The Doppler imaging algorithm enables this high level of accuracy by combining measurements from a range of carrier frequencies.

4.10   Conclusion

The effect of RMA variant, transmit power, antenna array size, antenna spacing, antenna design, RF bandwidth, surface material, RF SNR and clock jitter on image quality has been characterized. The main findings can be summarized as follows:

- A transmit power as low as 1 µW can be used when the objects being imaged are at a distance of 0.5 m from the array.

- Transmit power has no effect on image resolution.

- The colocated and Doppler range migration algorithms were able to produce images with a resolution of 12.5 mm at a distance of 0.5 m, when an array of 80×80 antennas was used. The single transmitter algorithm, X-MIMO and M-TX N-RX MIMO algorithm, when M is small, produced images with resolution that was twice as large in millimeters (i.e. worse). All resolution measurements agreed well with the theoretical values in Table 2.1.

- Increasing the antenna array size produces a proportional improvement in image resolution, until the half-wavelength resolution limit is reached. The measured relationship

between array size and image resolution matches well with the theoretical relationship given in Table 2.1.

- Increasing antenna array size also results in a correlated increase in image SNR. Therefore, antenna array size is extremely important.

- Antennas cannot be placed more than 0.9λ apart, otherwise image aliasing occurs.

- The imaging algorithms can handle up to 30% randomly-located antenna failures with minimal effect on image quality.

- The Vivaldi antenna produced the best images, due to its wide beamwidth and bandwidth. The patch antenna performed the worst, due to its phase center variations.

- The depth resolution achieved matched the theoretical value of the speed of light divided by twice the bandwidth.

- Human skin can be imaged particularly well in the 20 GHz band, due to the diffuse reflection of the microwaves off the skin.

- Clock jitter up to 20% of the clock period can be tolerated, with minimal effect on image quality.

The relationship between receiver RF SNR and image quality, and how this relationship affects cost and power consumption, will be explored more in the next chapter.

Chapter 5

Energy and Cost Analysis

The first two experiments of Chapter 4 showed that transmit power directly affects image SNR, but has little effect on image resolution (Figures 4.3 and 4.4). These experiments were, in effect, varying the RF SNR at the receive antenna. As shown by Figure 5.1, doubling the transmit power will result in double the power being captured at the receive antenna, assuming the scene remains constant. Since the thermal noise generated by the low-noise amplifier (LNA) is signal independent, double the signal power will be present at the LNA output, while the noise remains the same. The result will therefore be double the SNR at the receiver.
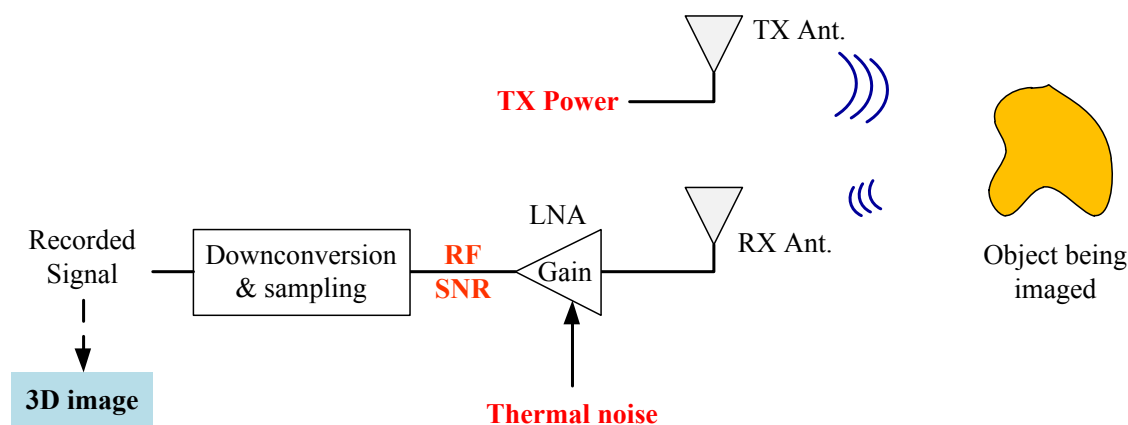
Figure 5.1: The RF SNR at the receiver is determined by the transmit power and LNA NF

The other parameter affecting the SNR at the receiver is the LNA noise figure (NF), assuming that the LNA NF dominates the NF of the entire receive chain. Doubling the noise figure will result in double the noise generated by the LNA, and hence halving the RF SNR. In both cases, the change in RF SNR will result in a change in image SNR, as shown in Figure 5.2. The data for this figure was obtained using a sophisticated software simulation that models external noise, component noise, path loss, reflective losses, and component non-linearities. This software simulation is discussed in more detail in Section 5.2. Note

that the image SNR in Figure 5.2 is converted to decibels using $20 \log(SNR)$, as image SNR is an intensity ratio and not a power ratio. This calculation agrees with the fact that the RMA takes, as input, the complex voltage measured at each antenna, rather than the power.

The simulation shows that the colocated imaging algorithm produces good, high resolution images for an RF SNR of -15 dB or higher. In the linear region, $\mathrm{SNR_{image}(dB)} \approx \mathrm{SNR_{RF}} + 30$ dB, due to array gain less component and algorithm noise. The image SNR is therefore directly proportional to the receiver RF SNR.
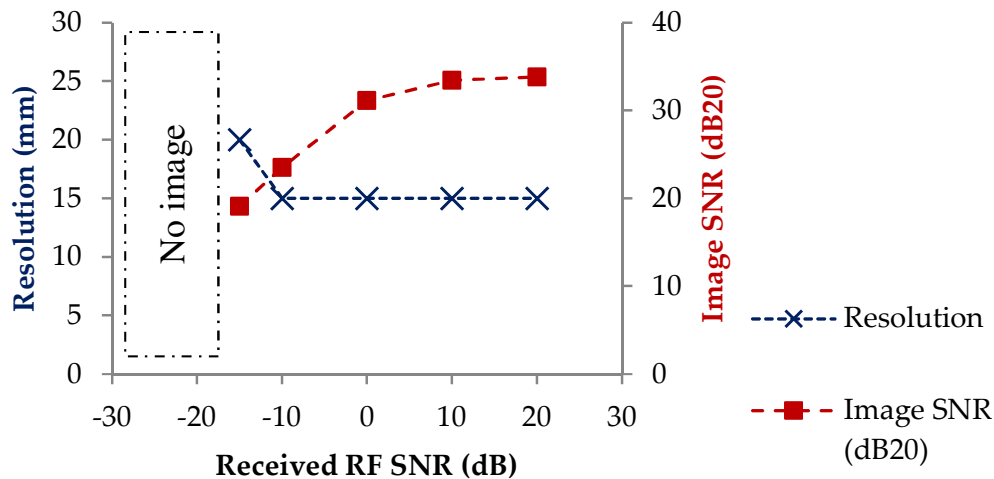
Figure 5.2: Simulation results showing the effect of RF SNR on image quality

Since both the transmit power and the NF of the receiver affect RF SNR, improving either one will improve image SNR. However, increasing transmit power or decreasing LNA noise figure will increase power consumption, assuming a given transceiver topology and technology process. This result suggests a trade-off between image SNR and power consumption.

This trade-off is very important, as high-resolution imaging systems require large numbers of microwave transceivers, which can result in high power consumption. To make these large arrays viable, power consumption needs to be reduced as much as possible without sacrificing image quality. In fact, transmitting at very high power levels usually offers little advantage over more moderate transmit levels, as the maximum image quality is often be limited by ADC quantization noise.

While there has been much research into low-power systems for wireless communications, such as [35] and [36], with performance being characterized by standard metrics such as power consumption per range or energy (Joule) per bit, the author is not aware of any such investigations for microwave imaging systems. This chapter therefore performs an analysis of how antenna and transceiver parameters affect energy consumption. Furthermore, a novel figure of merit for specifying the energy efficiency of microwave imagers will be introduced and used to develop a methodology for designing energy efficient imaging systems.

This chapter focuses on the effect that transmit power and LNA NF have on energy consumption and image SNR. The effect on resolution is mostly ignored, as it was shown in the previous chapter (and above in Figure 5.2) that receiver RF SNR has no effect on image resolution, provided that the image SNR is high enough to actually form a useful image. This lower bound on the usable image SNR is usually around 10 (20dB). All the experiments in this chapter will therefore include the restriction that the image SNR must be above this minimum required level to actually form recognizable images, hence allowing image resolution to be ignored.

While the goal of this chapter is energy reduction, cost reduction is important too. However, cost is difficult to model as it varies greatly with the technological breakthroughs, market trends and production volume. Fortunately, the results shown in this chapter for energy reduction also hold true for cost reduction. Reducing the transmit power levels or building a noisier LNA will not only reduce energy consumption, but also make these devices cheaper to manufacture.

5.1   A New Figure of Merit for Energy Efficiency of Imaging Systems

The goal is to operate the imaging system in such a way that image quality is maximized while energy consumption is minimized. This can be expressed as maximizing the ratio of image quality to energy consumption. To aid in this goal, a new figure of merit (FOM) is defined for microwave imaging systems:

$$FOM = \frac{SNR_{image} \times N_{voxels}}{E} \quad [SNR/Joule] \tag{5.1}$$

where SNR_{image} is the image SNR, N_{voxels} is the number of voxels in the image and E is the energy required to form the image. This new figure of merit describes how efficiently an imaging system can create a microwave image of a given size and image quality. Since E, the energy consumption of the system, is dependent on the total number of antennas and hence voxels in the output image, placing N_{voxels} in the numerator normalizes this energy to that required to capture a single voxel. The metric can therefore also be viewed as the image SNR that the system is able to generate per Joule of energy expended per voxel in the image. The figure of merit does not include resolution, as Figure 5.2 showed that resolution is not affected by RF SNR and hence power consumption.

The previous chapter showed that image SNR is determined primarily by transmit power, number of antennas, receiver noise and external noise. The energy consumed is determined by the number of transmitters and receivers, the power consumption of each transmitter and receiver, and the integration time. Furthermore, both the image SNR and energy consumption are influenced by the choice of imaging algorithm.

It is also clear that the target or scene being imaged will influence the image SNR (see Figure 4.9, for example), and hence the figure of merit. However, the figure of merit should

evaluate the imaging system only and be independent of the scene. While the figure of merit could be modified to compensate for the effect of the scene (such as including terms for the distance to and radar cross section of each object in the scene), it was instead decided that a "standard scene" would be used when evaluating the figure of merit. The standard scene was chosen to be a metallic sphere, 0.1 m in diameter, placed 1 m in front of the imaging array.

5.2 Modelling the Energy/Image Quality Trade-off

Since image SNR is a complex, non-linear function of parameters such as transmit power, number of antennas, receiver noise and external noise, developing a closed-form expression for image SNR is not tractable. Furthermore, it is not feasible to experimentally determine the effect of all these parameters on image SNR, due to the difficulty in accurately varying external and receiver noise in the real world. Therefore, a MATLAB software simulation was used, in place of the imaging testbed, to measure image SNR over a range of these parameters. The architecture of the noise model is shown in Figure 5.3. It models all the transmitters, path losses, reflecting objects in the scene, external interference, noise sources and component variation to calculate received signal power and received noise. This simulated received signal plus noise is then fed into one of the microwave imaging algorithms for processing. The parameters associated with each component of the noise simulation is shown below the dotted line in Figure 5.3. Due to the large number of parameters, only the underlined parameters were varied for the simulations, while the rest were set to nominal values based on lab measurements.

Unlike image SNR, the energy required to form the image can be calculated analytically from the experimental parameters. The power consumed by the transmitter is determined primarily by the power amplifier (PA). Assuming the PA has efficiency η, the power required for a single transmission is:

$$P_{PA} = \eta \cdot P_{TX} \tag{5.2}$$

where P_{TX} is the transmit power. Since passive mixers and low-speed ADCs can be used at the receiver, the LNA dominates the receiver power consumption. As a first order approximation, the noise figure of an LNA is inversely proportional to its bias current squared [37]. Since power consumption is directly proportional to bias current squared, the LNA's power consumption is related to its noise figure via:

$$P_{LNA} = \frac{\alpha}{NF_{LNA}} \tag{5.3}$$

where α is a device technology parameter. Furthermore, the noise figure of the entire receive chain is determined primarily by the LNA's noise figure, due to its high 50 dB gain. We can therefore assume that the component noise at the receiver can be completely characterized by the LNA noise figure.
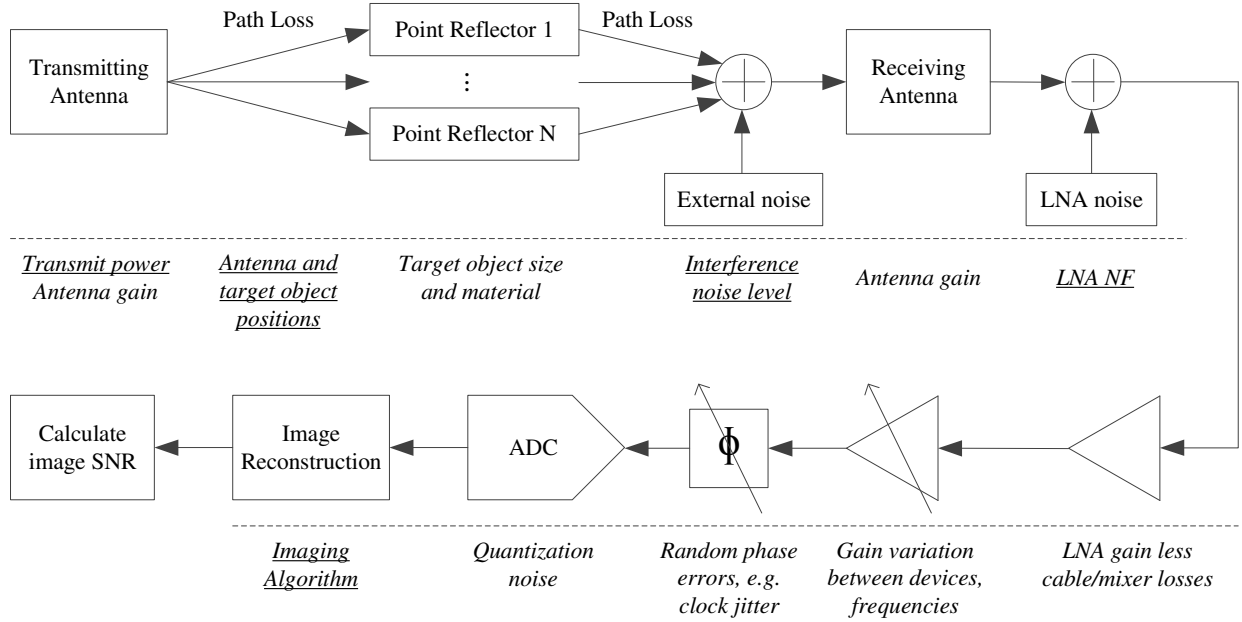
Figure 5.3: The architecture of the noise and energy simulation model. Underlining indicates the parameters that were varied during the simulations.

Expressions for the total energy required to form an image can therefore be given for the different RMA algorithms, where N_{ant} is the total number of antennas, N_f is the number of frequency steps and T_{int} is the amount of time spent transmitting, receiving and then integrating each frequency step at the receiver.

$$E_{coloc} = \left(\eta \cdot P_{TX} \cdot N_{ant} \quad + \quad \frac{\alpha}{NF_{LNA}} \cdot N_{ant} \right) \cdot N_f \cdot T_{int} \tag{5.4}$$

$$E_{STX} = \left(\eta \cdot P_{TX} \quad + \quad \frac{\alpha}{NF_{LNA}} \cdot N_{ant} \right) \cdot N_f \cdot T_{int} \tag{5.5}$$

$$E_{XMIMO} = \left(\eta \cdot P_{TX} \cdot \sqrt{N_{ant}} \quad + \quad \frac{\alpha}{NF_{LNA}} \cdot N_{ant} \right) \cdot N_f \cdot T_{int} \tag{5.6}$$

Note that the single-transmitter algorithm clearly uses the least energy, as each frequency step is only transmitted once. In the X-MIMO case, the array is assumed to contain $\sqrt{N_{ant}}$ transmitters and $\sqrt{N_{ant}}$ receivers, for a total of $2\sqrt{N_{ant}}$ antennas.

5.3   Results of Energy and Cost Analysis

The results of the energy and SNR simulations are presented in this section. As explained previously, transmit power and LNA noise figure are the parameters that most affect energy

consumption. The transmit power was therefore varied from -30 dBm to 6 dBm, and the LNA noise figure from 3 dB to 51 dB, while the figure of merit was computed at each operating point. For these simulations, PA efficiency η was set to 0.1 and LNA parameter α was set to 0.16 W so that they matched devices used for the experiments in Chapter 4.

The power configuration that produced the best figure of merit for five different scenarios is shown in Figure 5.4. The scenarios included different array sizes, imaging algorithms, distance from array to target sphere and amounts of external interference. The scenarios are labeled as follows:

Name	Array Size	Algorithm	Target Distance	Interference
80×80	80×80	Colocated	1m (standard)	None
80×80 0.5m	80×80	Colocated	0.5m	None
80×80 interf.	80×80	Colocated	1m (standard)	-90 dBm
160×160	160×160	Colocated	1m (standard)	None
80×80ST	80×80	Single TX	1m (standard)	None
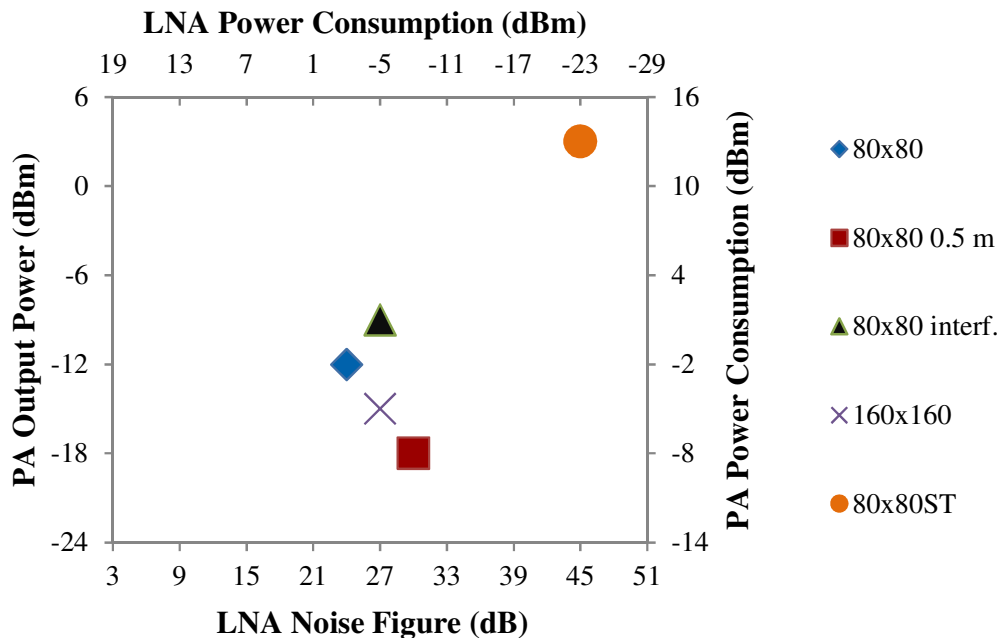
Figure 5.4: Optimum power operating point for different scenarios

The 80×80 configuration produced its best figure of merit with -12 dBm transmit power and a LNA noise figure of 24 dB. While the noise figure may seem high, the noise generated by the different LNAs is uncorrelated and adds incoherently. Therefore, after processing, the SNR improves by a factor proportional to the number of antennas [38]. At the optimum operating point, each transmit PA consumes -2 dBm power and each LNA consumes -2 dBm. It is not coincidence that the best figure of merit is obtained when the

transmitter and receiver consume equal power. In low-power wireless systems, it is well known that the most power efficient way to achieve a certain link margin is to distribute the power evenly between the transmitter and receiver [39]. The same argument can be made here for microwave imaging systems.

While external interference has been mostly ignored thus far in this dissertation, it is a concern in real-world systems. Any external RF transmitter in the same, or nearby, frequency bands will cause interference. When external interference is added (80×80 *interf.*), the optimum figure of merit is obtained by increasing the transmit power and decreasing the LNA noise figure to compensate for this interference and maintain the same RF SNR at the receiver, while evenly distributing the power consumption between PA and LNA.

If the distance between the antenna array and target sphere is halved (80×80 *0.5m*), the combined path loss decreases by 12 dB. With the extra 12 dB margin, the simulation shows that the optimum figure of merit is achieved by decreasing the transmit power by 6 dB and increasing the LNA noise figure by 6 dB, as expected. This result highlights the importance of using a standard scene when evaluating the figure of merit, as the distance to the target has a large effect.

If the array is increased in size to 160×160 antennas, the $4\times$ increase in the number of antennas gives an extra 6 dB array gain. The results show that this extra gain allowed the transmit power to decrease by 3 dB and the LNA noise figure to increase by 3 dB, resulting in 3 dB less power consumption per transceiver.

The last simulated scenario was the single transmitter algorithm ($80 \times 80 ST$). The transmitter transmits once only, and this signal is shared by all the receivers. The most energy efficient approach is therefore to increase the transmit power and to decrease the power consumption at receivers, such that the power consumption of the single transmitter is equal to the combined power consumed by all the receivers. Consequently, the transmitter consumes N^2 more power than each receiver, for an NxN array. This relationship is illustrated by the optimum figure of merit being achieved, in this case, with a 3 dBm transmit power and a 45 dB noise figure for the LNAs.

It should be mentioned that to prevent the search algorithm setting the image SNR so low that the images became useless, the image SNR was constrained to 10 or higher during the search process.

Figure 5.5 shows the energy required to compute a single voxel for each scenario, when operating at the best figure of merit. Halving the distance to the target results in 4x less energy consumption. This result makes sense, as the 80×80 *0.5m* operated with 6 dB lower transmit power and 6 dB higher noise figure. The addition of external interference requires 25% more energy.

The 160×160 array, interestingly, requires only half as much energy to compute a voxel as the 80×80 array. This is because the PA and LNA both operate at half the power, and even though there are more transceivers, the energy consumption is normalized per voxel.

Theoretically, the single transmitter should consume N=80 times less energy than the colocated algorithm, but the simulations showed a $160\times$ reduction, due to the simulation step size.
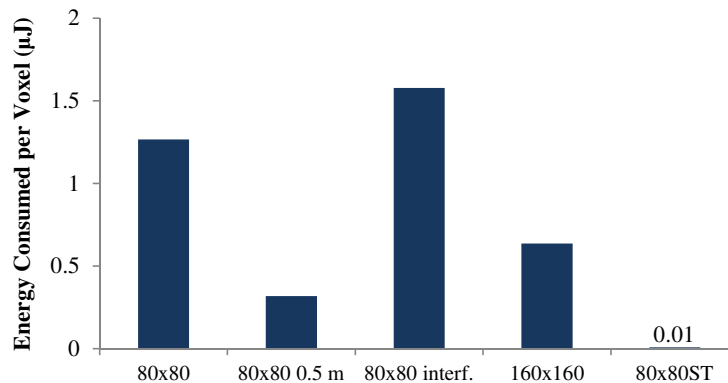
Figure 5.5: Optimum energy consumption for different array configurations

Finally, Figure 5.6 shows how the figures of merit compare for the different scenarios. Even though the single transmitter algorithm produces lower resolution images than the colocated algorithm, it is much more energy efficient, as the single transmitter simultaneously transmits to all the receivers. Furthermore, larger arrays have higher figures of merit than smaller arrays. Specifically, the figure of merit is proportional to the number of antennas per side of the array. Lastly, external interference and longer distances between array and scene can degrade the figure of merit.
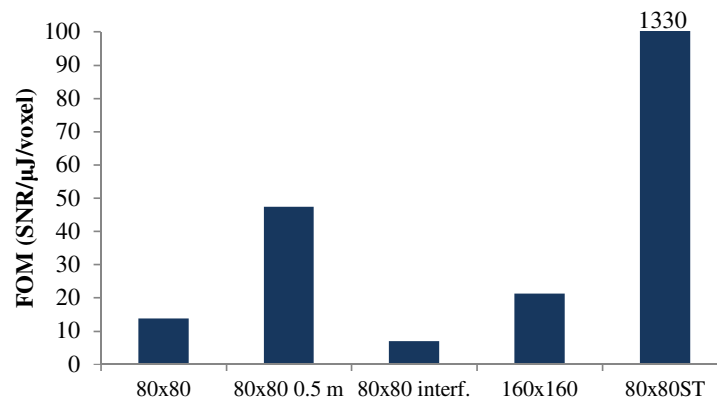
Figure 5.6: Optimum figure of merit for different array configurations

5.4   Design Methodology for Energy and Cost Efficient Arrays

The results shown here suggest a methodology for designing energy- and cost-efficient antenna array systems for microwave imaging.

1. The required image resolution directly specifies the array aperture, as characterized in Figure 4.5. Furthermore, large arrays are more energy efficient, as shown in Figure 5.6.

2. The minimum required image SNR should be determined based on the desired application. Decreasing the required image SNR to this level permits a lower RF SNR, and in turn a lower transmit power and a higher noise figure for the LNAs (see Figures 4.3 and 5.2). Using Figure 5.2, the RF SNR required to meet this image SNR can be determined.

3. The transmit power and LNA noise figure can then be calculated to achieve this RF SNR, while ensuring that the transmitter and receiver consume equal power. This second requirement is essential for ensuring energy efficiency. The calculation can be performed using standard path loss and radar cross-section formulas.

4. If significant RF interference is expected, the transmit power can be increased slightly and the noise figure decreased slightly to accommodate the interference.

5. To further reduce cost, the antennas can be placed more than $\frac{\lambda}{2}$ apart without significant image quality loss (but less than 0.9λ), reducing the number of required transceivers.

6. PCB antennas, such as Vivaldi antennas, can be used in place of horn antennas, as they are significantly cheaper and work just as well.

5.5   Conclusion

It has been shown that microwave imaging systems can be built using low-power transmitters and low-power (and hence noisy) receivers. Using low power transmitter and receiver components will reduce both the power consumption and cost of the system.

To determine the optimum power levels for the transmitters and receivers, a novel figure of merit has been introduced. This figure of merit quantifies how efficiently these systems can compute a single voxel in the final 3-D image. The colocated RMA algorithm achieved the best figure of merit with a -12 dBm transmit power and a 24 dB LNA noise figure. In this configuration, the transmitter and receiver consumed equal energy,

The single transmitter algorithm was found to be most energy efficient with a single high power transmitter and many low power receivers. In all cases, it was found that the figure of merit could be improved by increasing the array size or changing from the colocated to single transmitter algorithm.

Combining all these results lead to a methodology for designing antenna arrays that are both energy and cost efficient. The relationships between antenna configuration, image quality and energy consumption that were characterized allow the designer to trade off image quality with cost, while still building a system that is as energy efficient as possible.

Chapter 6

Sparse Antenna Arrays and Compressive Sensing

Although microwave imaging enables the many useful applications discussed in Chapter 1, few large-scale 3-D microwave imaging systems have been built to date. This lack of real-world imaging systems is primarily due to cost reasons. A large antenna aperture is required for good image resolution, and most image reconstruction algorithms, including the range migration algorithm (RMA), require that the antennas be placed in a rectangular grid array with sub-wavelength spacing. Chapter 4 showed that violating this requirement typically results in grating lobes and poor image quality [40]. A large number of antennas and radio transceivers are therefore required for these systems. It has previously been shown that an array of at least 64×64 antennas is needed for the hand gesture-recognition applications, requiring over 4000 antennas and radio transceivers.

The previous chapter showed that the cost of these systems can be reduced by designing each antenna and transceiver to be as low-cost as possible, through the use low-power and low-quality components. This chapter, however, takes a different approach. Instead of making each antenna/radio transceiver cheaper, the number of antennas required to achieve a specific image resolution can be reduced. This reduction is achieved using a sparse array, also known as a thinned array, with the same aperture, and hence providing the same imaging resolution, as a fully-populated array, but containing fewer antennas. If the existing fully-populated two-dimensional array contained $N \times N$ antennas, then the proposed sparse array will contain $M \ll N^2$ antennas, randomly placed within the existing array aperture.

It was shown (see Figure 4.6) that the standard RMA algorithm requires antennas to be placed on a dense regular grid with sub-wavelength spacing, otherwise grating lobes occur, causing image aliasing. Therefore, a different imaging algorithm needs to be used to reconstruct the images. A novel compressive sensing (CS) image reconstruction algorithm was therefore developed for use with these sparse antenna arrays.

While 3-D microwave imaging using fully-populated planar arrays has been well researched [1] [3] [19], imaging using sparse antenna arrays has been less well investigated. There has been some work into using sparse linear arrays and CS to capture 2-D images

for radar applications [41] [42]. In these cases, the scene was assumed mostly empty except for one or two aircraft or other objects which occupy only a few pixels in the image. Prior attempts to use CS with sparse planar antenna arrays for 3-D imaging [43] again assumed that the scene being imaged is sparse in the spatial domain. Unfortunately, this assumption, that the environment is mostly sparse except for a few point reflectors, cannot be made for indoor imaging applications where the environment is cluttered with multiple large objects.

It will, however, be shown in this chapter that these complex indoor scenes can be transformed into the wavelet domain where they do have sparse representations, allowing CS reconstruction to be performed.

While there has been some work into sparse array imaging using techniques other than CS, such as using an aggregate point scatterer basis function [44], these approaches are beyond the scope of this dissertation.

6.1 Overview of Compressive Sensing

This section gives a brief overview of compressive sensing. For a more complete explanation and tutorial, please see [45] and [46].

Compressive sensing allows a compressible signal g to be captured and reconstructed when the average sampling rate is below the Nyquist threshold [47]. A compressible signal is one where the information rate is much less than the signal bandwidth.

Let w be the representation of signal g (of length N) in the Ψ domain. g is compressible, or sparse, if there exists some domain Ψ in which most of the coefficients of w are zero, or can be set to zero without perceived loss in signal quality. If w has K non-zero coefficients, then g and w are said to be K-sparse.

The measurement of signal g is performed by correlating it with a set of measurement vectors $\{\Phi_j\}_{j=1}^{M}$. Each correlation gives a single measurement m_j. If the measurements are noisy with a standard deviation of σ, the original signal can be reconstructed by solving the following optimization problem:

$$\min_{g'} \|\Psi^* g'\|_{l1} \text{ subject to } \|m - \Phi g'\|_{l2} \leq \sigma, \tag{6.1}$$

where Ψ^* is the transform into the domain where g is sparse and m is a vector containing all the measurements m_j.

It has been shown [48] that if the mutual coherency between Φ and Ψ^* is small, the optimization problem will converge, with high probability, to correct solution g when only a small number of measurements $M < N$ are made. The lower bound on M is determined by K, the number of non-zero coefficients of w. The lower bound on M is usually given as:

$$M \geq cK \log(N/K) \tag{6.2}$$

where c is a small constant [47].

6.2 Compressive Sensing for Microwave Imaging

The proposed compressive-sensing algorithm for microwave imaging attempts to recover a 3-D image of an indoor environment from discrete radio frequency samples, collected using a sparse planar antenna array. It is based on the general algorithm described in Section 6.1, and hence the same variables will be used. The particular meaning of the variables, in this case, is as follows:

- g is the 3D image to be recovered.

- Vector m contains the complex voltage samples recorded at each antenna at multiple radio frequencies.

- Φ is the sampling function that describes how the reflected radio waves are sampled.

- Ψ^* is the sparsifying transform. In this case, the wavelet transform will be used.

6.2.1 Sampling the scene

The scene must first be illuminated with a microwave signal before it can be sensed. One or more antennas in the array transmit a continuous wave (CW). This wave reflects off objects in the scene and these reflections are received by other antennas in the array. The magnitude and phase of the reflected wave is recorded at each antenna as a complex voltage and stored in vector m. Once all the antennas have recorded the backscattered signal, the transmitting antenna will then transmit the next frequency ω_i in a set of frequencies $\{\omega_i\}_{i=1}^{N_f}$. If there is more than one transmitting antenna, the process is repeated for each transmitter.

Standard 3-D microwave imaging algorithms, including the RMA, assume that the antennas are placed in a fully-populated, rectangular grid with regular sub-wavelength spacing and that the frequency steps w_i are equally spaced [3]. The CS algorithm makes the same assumption, with the exception that only a fraction of the possible antenna locations are actually populated; and only a fraction of the frequency steps are actually transmitted and sampled. This array architecture is illustrated in Figure 6.1. To ensure that the CS sampling function is incoherent to the sparsifying function, the antenna locations and frequency steps used are chosen randomly. The backscattered wave is therefore randomly undersampled in both space and frequency.

The antenna array and scene geometry is shown in Figure 6.2. The antenna array lies in the xy-plane at $z = Z_0$, and contains at least one transmitting antenna and any number of receiving antennas. The reflectivity of point (x, y, z) in the scene is given by function $f(x, y, z)$. The distance from antenna at location (x_a, y_a) to point (x_s, y_s, z_s) in the scene is given by:

$$d(x_a, y_a, x_s, y_s, z_s) = \sqrt{(x_a - x_s)^2 + (y_a - y_s)^2 + (Z_0 - z_s)^2}. \tag{6.3}$$
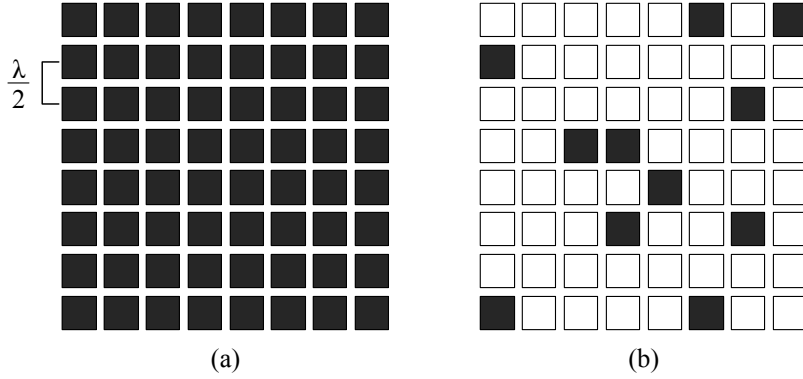
Figure 6.1: (a) Fully-populated antenna array (b) Sparse array with randomly-placed antennas, where the black squares indicate actual antenna locations
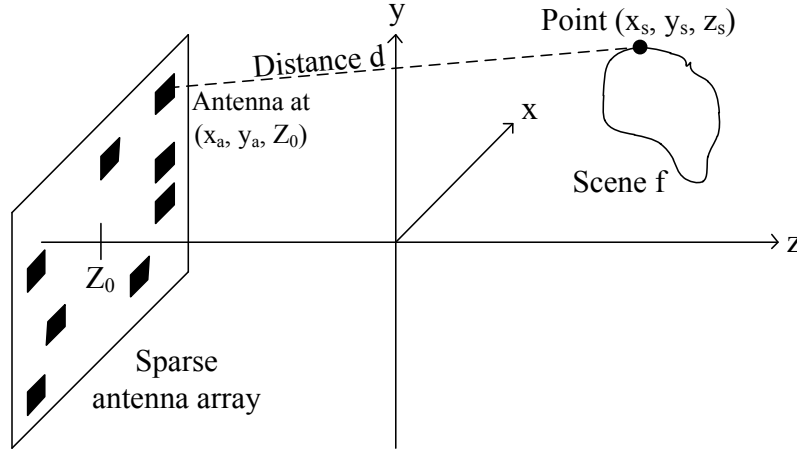
Figure 6.2: The geometry of the sparse antenna array and the scene being imaged

The sampling matrix, Φ, describes the relationship between the scene being imaged and the backscatter radio-frequency (RF) samples. Assume that the scene consists of a single point reflector at position (x_s, y_s, z_s) with reflectivity $f(x_s, y_s, z_s)$. The reflected RF signal m, measured at antenna at location (x_r, y_r, Z_0), when antenna at location (x_t, y_t, Z_0) transmits at frequency ω_i, is then given by:

$$m_{point}(x_r, y_r, x_t, y_t, \omega_i) =$$
$$\frac{f(x_s, y_s, z_s)}{d(x_t, y_t, x_s, y_s, z_s)d(x_r, y_r, x_s, y_s, z_s)k_i} \times e^{-jk_i(d(x_t, y_t, x_s, y_s, z_s)+d(x_r, y_r, x_s, y_s, z_s))} \quad (6.4)$$

Since m represents the voltage, and hence electric field strength, at each receive antenna, the denominator term in (6.4) takes into account the attenuation in received field strength with distance from point reflector. The exponential term gives the round-trip phase delay

and wavenumber $k_i = \omega_i/c$, where c is the speed of light. Constants have been omitted. Note that this expression looks very similar to the formula that was used for the received signal $s(x_a, y_a, \omega)$ in the derivation of the RMA.

By regarding any complex scene f as a collection of point reflectors, the signal received for any arbitrary scene can be found by integrating over the scene:

$$m(x_r, y_r, x_t, y_t, \omega_i) =$$
$$\iiint_{scene} \frac{f(x, y, z)}{d(x_t, y_t, x, y, z)d(x_r, y_r, x, y, z)k_i} \times e^{-jk_i(d(x_t,y_t,x,y,z)+d(x_r,y_r,x,y,z))}dxdydz \quad (6.5)$$

If the 3D scene to be imaged is discretized into voxels, the integrals in (6.5) can be replaced with summations. Furthermore, if the resulting 5-D measurement matrix $m[x_r, y_r, x_t, y_t, \omega_i]$ is vectorized to form a single vector $m[a]$ of M backscatter measurements, and the 3-D matrix $f[x, y, z]$, representing the scene, is vectorized to a single vector $f[b]$ where $b = 1..N$, then (6.5) can be expressed as:

$$m[a] = \sum_{b=1}^{N} \frac{f[b]}{d_t[a,b]d_r[a,b]k[a]} \times e^{-jk[a](d_t[a,b]+d_r[a,b])} \qquad \text{for } a = 1..M, b = 1..N \quad (6.6)$$

In the equation above, M is the total number of measurements made at all antennas and frequencies; and N is the total number of voxels in the 3-D scene being imaged. $f[b]$ is the reflectivity of the scene at point b. $d_t[a,b]$ is the distance from the transmitting antenna used in measurement a to point b in the scene, $d_r[a,b]$ is the distance back to the receiving antenna and $k[a]$ represents the microwave frequency used for measurement a.

The entire expression can now be written as a matrix-vector multiplication:

$$m = \Phi f, \quad (6.7)$$

where measurement matrix Φ contains a row for each measurement at each antenna and frequency, and a column for each point in the scene. Element $\Phi_{a,b}$ at location (a, b) in matrix Φ is given by:

$$\Phi_{a,b} = \frac{e^{-jk[a](d_t[a,b]+d_r[a,b])}}{d_t[a,b]d_r[a,b]k[a]}. \quad (6.8)$$

These equations are for the general MIMO case, where any antenna may be arbitrarily designated a transmitter or a receiver. Simplifications can be made for single transmitter imaging systems by setting x_t and y_t constant; and for colocated systems (where the receiving antenna is placed immediately adjacent to the transmitting antenna) by replacing variables x_t and y_t with x_r and y_r.

6.2.2 Sparsifying the image

Although the scene may contain many objects, and hence not be sparse in the spatial domain, the surface of each object is typically made from a single material. Each object therefore appears as a solid surface with uniform intensity when imaged in the microwave spectrum. Such piecewise-constant images of real-world objects are known to be sparse in the wavelet domain [49]. The discrete wavelet transform is therefore used as the sparsifying transform, Ψ^*.

The CS algorithm for microwave imaging can therefore be summarized as solving the following optimization problem

$$\min_{f'} \|wavelet\{f'\}\|_{l1} \text{ subject to } \|m - \Phi f'\|_{l2} \leq \sigma, \tag{6.9}$$

where f' is the estimate of the vectorized 3-D scene, m contains the backscatter measurements, Φ is given in (6.8) and σ is the standard deviation of the RF noise at the receiver. Since each row of Φ represents a randomly selected antenna or frequency, it can be shown that Φ is incoherent to the wavelet transform Ψ^* [48], ensuring stable image recovery.

Besides being able to handle sparse antenna arrays much more efficiently and accurately than the range migration algorithm, the compressive algorithm also has the advantage of being able to handle multistatic systems where multiple transmitters are spaced multiple wavelengths apart.

6.3 Experimental Setup

6.3.1 Antenna array

The same antenna array setup that was described in Chapter 3 is used here for the CS experiments. The XY-table was used to mechanically move a single transmit antenna and a single receive antenna to each of the random antenna locations. In this way, a large sparse antenna array was emulated using just two physical antennas.

Since the Vivaldi antenna was found to be the best-performing antenna in Chapter 4, it was used for all the CS experiments. The XY-table and two Vivaldi antennas used to emulate the sparse array are shown in Figure 6.3. Again, it must be emphasized that the XY-table was used merely for evaluation purposes; the final system would use the same image reconstruction algorithm but with a fixed sparse array of a few hundred randomly placed antennas. The RF frontend connected to these two antennas is the same as was shown previously in Figure 3.5.

6.3.2 Performance metrics

To compare the quality of images produced by sparse antenna arrays to those produced by fully-populated arrays, the image signal-to-noise ratio (SNR) and image resolution were

Linear actuators to move antennas

Receive antenna

Transmit antenna

Resolution phantom being imaged
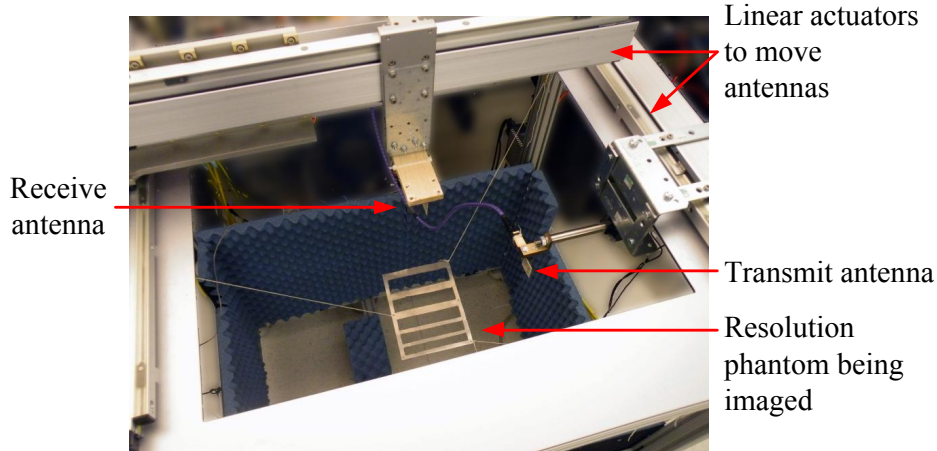
Figure 6.3: The antenna array emulator.

measured for different array configurations.

6.3.3 Implementation of the reconstruction algorithm

The proposed CS reconstruction algorithm was implemented in MATLAB, using the SPGL1 library [50] to solve the optimization problem. This library takes as input the Φ and Ψ matrices (i.e. the matrix given by (6.8) and the MATLAB function for the wavelet transform), the vector m of antenna measurements, and the noise parameter σ. The library returns the recovered image of the scene.

The algorithm used by the SPGL1 solver

Although an understanding of how SPGL1 solves the compressive sensing optimization problem is not required, some insight into its inner workings does aid in optimizing performance. This section will therefore outline, at a high level, how compressing-sensing problems are solved in general, as well as how the SPGL1 library works.

Most compressive-sensing problems are expressed as a type of basis pursuit problem. The original basis pursuit problem can be described as finding a *sparse* solution x to an under-determined set of equations $Ax = b$, where matrix A is of size $m \times n$ with $m \ll n$. The problem can therefore be expressed as finding the minimum l_1-norm of an under-determined least-squares problem. A common approach to solving basis pursuit is to use convex optimization to solve the following the problem [51]

$$\min_x \|x\|_{l1} \text{ subject to } Ax = b \tag{6.10}$$

If the data is noisy, then the constraint is relaxed to become $\|Ax - b\|_{l2} \leq \sigma$, giving

$$\min_x \|x\|_{l1} \text{ subject to } \|Ax - b\|_{l2} \leq \sigma, \tag{6.11}$$

Equation (6.11) is known as basis pursuit denoising (BPDN) and is the form taken by most compressive sensing problems. Since (6.1), which was originally given for compressive sensing, does not exactly match the form of the basis pursuit problem, it is often recast as follows to allow it to be solved using a BPDN solver:

$$\min_{G'} \|G'\|_{l1} \text{ subject to } \|\Phi\Psi G' - m\|_{l2} \leq \sigma \tag{6.12}$$

where G' is the representation of g' in the domain where it is sparse, and Ψ is the inverse Ψ^* transform. It is useful to note that the BPDN problem can be posed in three related forms:

$$\textbf{BP}_\sigma \textbf{ form: } \min_x \|x\|_{l1} \text{ subject to } \|Ax - b\|_{l2} \leq \sigma \tag{6.13}$$

$$\textbf{QP}_\lambda \textbf{ form: } \min_x \|Ax - b\|_{l2} + \lambda\|x\|_{l1} \tag{6.14}$$

$$\textbf{LS}_\tau \textbf{ form: } \min_x \|Ax - b\|_{l2} \text{ subject to } \|x\|_{l1} \leq \tau \tag{6.15}$$

These three forms are only equivalent for very specific values of constants σ, λ and τ. Chen and Donoho [51], however, showed that if A is orthogonal, then converting between the first two forms is trivial. Therefore, a common approach used by many CS solvers is to require that A is orthogonal and then convert the standard CS equation (6.1) to the QP_λ form (6.14). The advantage of the QP_λ form is that it is a convex quadratic programming problem for which many efficient algorithms already exist, such as iteratively reweighted least squares [52] or gradient projection [53].

The approach used by SPGL1 is to solve the basis-pursuit denoising problem BP_σ by instead solving a sequence of related LS_τ problems (6.15). The reasoning is that the LS_τ form of the BPDN problem can be computed more efficiently than the BP_σ form [50].

The SPGL1 algorithm attempts to find the value of τ that will result in the LS_τ form of the problem having the same optimal solution as the BP_σ form, for the specified value of the noise parameter σ. The algorithm starts by guessing a value of τ, and then loops through the following steps:

1. Solve LS_τ for the most recent estimate of τ, using spectral gradient projection.

2. The calculation of LS_τ, in the step above, also gives the value of σ that would result in BP_σ having the same optimal solution as LS_τ for the current value of τ. If this value of σ is below the desired noise threshold, then the algorithm can stop. Otherwise, continue to next step.

3. Use a modified version of Newton's method to find a better approximation of root τ for the next iteration.

4. Go to step 1.

The optimal solution to the LS_τ problem, solved in step 1 of the last iteration of the loop above, is also the optimal solution to the desired BPDN problem.

6.4 Compressive Sensing Results

The array emulator was used to evaluate both fully-populated and sparse antenna arrays with an aperture of 320 mm × 320 mm. The fully-populated array contained 64 × 64 antennas (4096 antennas total). Sparse arrays with the same aperture, but consisting of 1024, 400 and 160 antennas were also emulated, representing 25%, 10% and 4% array densities, respectively. The following microwave imaging algorithms were compared:

- *RMA:* The RMA was evaluated as a baseline, with colocated transmit and receive antennas. For the array of 1024 antennas, zero filling in the missing antenna locations generally gave better results than decreasing the array aperture. This is because the random antenna placement helps to mitigate some of the grating lobes that typically result from running the RMA algorithm on sparse arrays. For the smallest arrays of 400 and 160 antennas, a combination of aperture reduction and zero filling was used to achieve best results.

- *Coloc CS:* The CS algorithm was evaluated on random sparse antenna arrays with colocated transmit and receive antennas. When an antenna transmits, only the antenna closest to it records the backscatter.

- *MIMO CS:* The CS algorithm was used with a sparse array where each receive antenna records backscatter from all other transmitters. Nine transmitters were used, evenly distributed throughout the array, for the 1024 and 400 element arrays. The sparsest array of 160 antennas consisted of 80 transmit antennas on one diagonal of the array and 80 receive antennas on the other, just like the X-MIMO configuration.

The phantoms in Figure 6.6 were imaged using both RMA and CS algorithms. While true 3-D images were captured, 2-D projections of these images are shown. These phantoms were placed at a distance of 0.5 m from the antenna array. It is clear that the CS algorithm is able to generate acceptable images of these phantoms with 400 antennas or less, while the RMA algorithm requires a dense 64 × 64 array of 4096 antennas.

Figure 6.4 shows the image resolution that can be obtained by each of these imaging algorithms and array sizes, when the scene is 0.5 m from the array. The *MIMO CS* algorithm produced images with a 12.5 mm resolution with as few as 160 antennas. The *Coloc CS* achieved 15 mm resolution with 1024 antennas and 25 mm resolution with 400 antennas.

The standard RMA algorithm produced similar resolution images, but required at least 1024 antennas. The proposed CS algorithm therefore produced higher resolution images with 6× fewer antennas than the standard RMA algorithm.
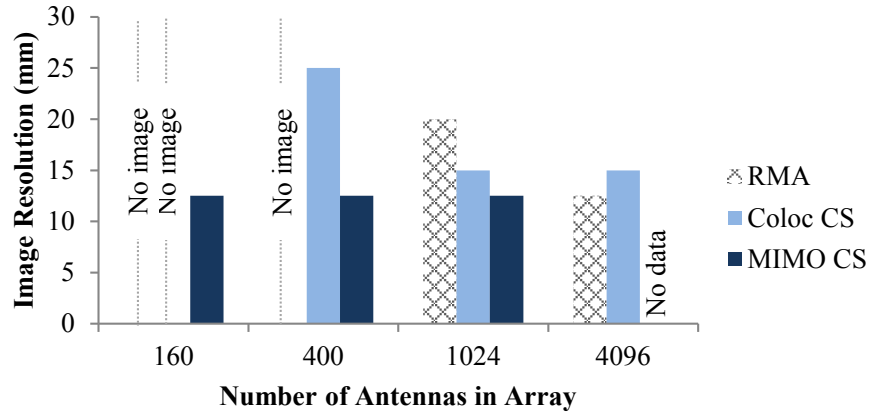
Figure 6.4: Image resolution achieved by each algorithm for different array sizes

Of interest is the 4096 antenna array, representing a fully populated array, which allows traditional microwave imaging to be used without grating lobe issues. Therefore, in this case, the exact solution determined by the RMA algorithm produced slightly higher resolution images than the approximate solution found by the CS approach.

As Chapter 5 showed that the RMA is able to work well at low transmit power levels, the CS algorithm was evaluated over a range of transmit powers. Figure 6.5 shows that while the RMA algorithm running on a dense array produced good images with a transmit power as low as -25 dBm, two of the three sparse array CS implementations were only able to operate down to -20 dBm. The reason that the CS implementations require higher transmit power is that sparse arrays contain fewer antenna elements than dense arrays, and hence have lower gain [54]. Even though the minimum power required for each radio transceiver increases by a factor of 3.2 (5dB) for the CS case, the number of transceivers decreases by at least a factor of 4, resulting in a net decrease in power consumption.

While the *MIMO CS* results for 1000 and 400 antennas produce similar image SNR results at each power level, the *MIMO CS* consistently produces images with a higher SNR, even though it uses fewer antennas. This is because the *MIMO CS 160* results were obtained using the X-MIMO array configuration (80 transmit antennas and 80 receive antennas), which produced more measurements than the other CS array architectures, and hence higher image SNR.

Interestingly, at higher transmit power levels, the CS algorithms produce images with a higher image SNR than the RMA algorithm, even though fewer antennas were used. This is because at higher transmit powers, the image SNR is limited by the image recovery algorithm, and not the received signal SNR. Hence, the decreased array gain has minimal effect.
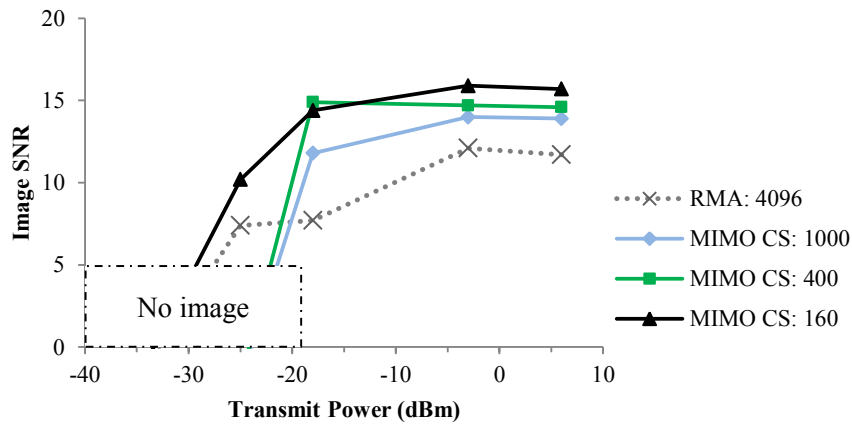
Figure 6.5: The effect of transmit power on image SNR

6.5 Computational Cost and Tuning Sensitivity

While the proposed CS algorithm has been shown to reduce the required number of antennas, it does have two drawbacks over the traditional range migration algorithm: computational cost and tuning parameter sensitivity. On average, a MATLAB implementation of the CS algorithm was $370\times$ slower than a MATLAB RMA algorithm, due to the computational complexity of the SPGL1 algorithm (it is iterative in nature) and the size of the sampling matrix Φ. Other l_1-norm minimization libraries were also investigated, but none performed better than SPGL1. Some, such as NESTA [55], performed significantly slower, while others, such as l1-MAGIC [47], were not able to handle complex numbers.

In practice, the CS algorithm would most likely be used in a real-time video imaging system. Therefore, the solver could be seeded with the previous video frame. Provided the images do not change significantly between video frames, seeding the algorithm with the previous video frame could substantially reduce computation time.

The quality of the produced images was also found to be sensitive to the noise parameter σ. While σ was manually tuned for the results presented here, an iterative tuning algorithm can be used for real-time online applications:

- Start by setting σ to its largest possible value, i.e. $\sigma = \|m\|_{l2}$, where m is the measurement vector.

- Decrease σ on each subsequent iteration frame until σ is made too small, usually indicated by the optimization solver suddenly requiring a large number of iterations to converge on a solution. At this point, σ should be increased slightly.

- Since SNR does not change much between subsequent video frames, only small changes should be required to σ from one frame to the next.
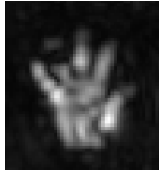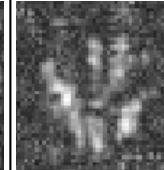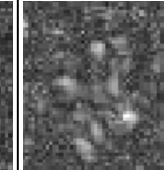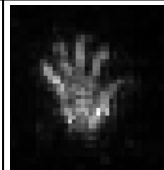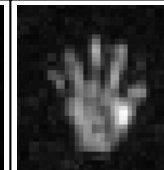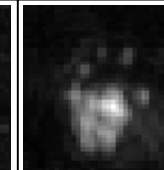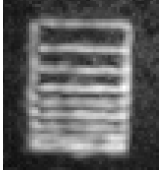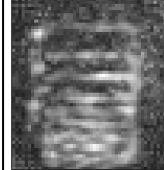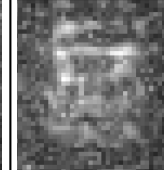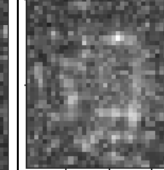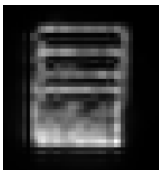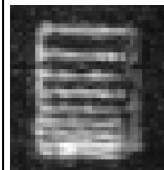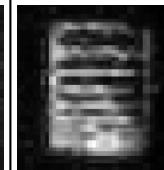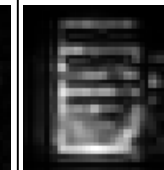
Figure 6.6: Comparison of 2-D projections of 3-D images obtained using the RMA algorithm and the proposed CS algorithm for various numbers of antennas. The human hand phantom is life-size, while the brass resolution tester is 200mm in length.

An alternative would be to use a homotopy algorithm for CS, such as [56] or [57], where each recovered video frame can be both used to seed recovery of the next frame and iteratively determine the optimal value for σ.

While it would have been advantageous to evaluate the optimizations discussed here, it was not possible due to the many hours that the motorized XY-table takes to gather the data for a single frame.

6.6   Conclusion

Although the RMA imaging algorithm is able to produce images from an antenna array as sparse as 25%, these images are noisy and blurry. The proposed CS algorithm was shown to produce images, without a loss in resolution or quality, with arrays with just 10% density. Furthermore, the CS algorithm produced usable images, with just minor reductions in quality, with antenna arrays with 4% density. This reduction in the number of antennas afforded by the CS algorithm translates into significant component cost and power consumption sav-

ings for microwave imaging systems. The CS algorithm also produces higher SNR images than the RMA algorithm at all but the lowest power levels.

The downside is the increased computational complexity of the CS imaging algorithm, which will increase the computational time and power required to form an image. This extra power required to compute the CS algorithm may offset the RF power savings from using fewer antennas. One solution would be to use specialized processing hardware (such as an ASIC or FPGA) to solve the proposed CS algorithm quickly with reduced power consumption.

Chapter 7

Timed Arrays and Radio Interferometry

Thus far, this dissertation has concentrated on imaging by measuring the phase distance between each antenna in an array and each point in 3-D space. However, two other approaches are often used for imaging instead: timed arrays and radio interferometry. Timed arrays form images by measuring the round-trip time delay between each antenna and each point in the scene, while interferometry forms images by correlating different antenna outputs and is typically used in radio astronomy to image astronomical objects. While neither of these techniques were found to be completely suitable for indoor 3-D imaging, they do share many similarities with phase-measurement-based microwave imaging, and hence are discussed here for completeness.

7.1   Timed Arrays

Timed arrays can be regarded as the time domain equivalent of phased arrays. They operate by transmitting ultra-short pulses in the time domain and measuring how long it takes the pulse to be reflected back, by the scene, to the receiving antennas. These ultra-short pulses have a very wide bandwidth, and so imaging systems using timed arrays are often known as ultra-wideband (UWB) imaging systems. Most existing UWB imaging systems have an operational frequency spanning, at least, 1 to 10 GHz [58] [59] [60].

Much like traditional imaging systems, the depth resolution of a timed-array imager is given by $\frac{c}{2B}$, where B is the bandwidth of the transmitted signal. Furthermore, the cross-range resolution of timed-array imagers is also inversely proportional to the bandwidth [61]. The bandwidth of these ultra-short pulses is primarily determined by their duration, rather than their edge rates. Therefore, higher bandwidth (and hence shorter pulse width) results in better image resolution in all dimensions.

Timed-array imagers typically work by transmitting a short pulse and measuring the delay and magnitude of the reflected pulse to determine distance to and reflectivity of an

object. To form a proper multi-pixel image, a narrow RF beam must first be formed and raster-scanned across the scene, while performing the distance measurement. Unfortunately, beamforming and steering cannot be implemented through phase shifting each antenna, due to the wide bandwidth of the transmitted pulse. Instead, beamforming on receive is achieved by delaying the output of each receive antenna by a specific amount before summing. A similar process can be used to beamform the transmitted signal. One of the advantages of timed arrays over phased arrays is that they are able to beamform within the near-field [62]. However, in this case, the beam is focused to a single point in the near field, rather than in a particular direction.

One of the main applications of timed arrays currently being investigated is high-resolution imaging for the detection of tumors in breast tissue [63] [64]. Timed arrays are particularly well suited to this application, as objects (i.e. tumors) need to be imaged with high resolution in the array near field.

7.1.1 How to form images

Timed-array imaging begins with transmitting an ultra-short RF pulse that has usually been shaped for a flat frequency-response across the entire bandwidth. This pulse reflects off objects in the scene and is received at the receiver antennas. Importantly, the pulse arrives at each receive antenna at a different time, depending on the round-trip delay from the transmit antenna to the object and back to each receive antenna.

If the scene contains multiple point reflectors, each antenna will receive a separate reflected pulse from each of these reflectors/objects. To separate out the reflected pulses from each of these objects, and hence form an image, the receive antenna array needs to form a narrow beam (i.e. beamform) and then raster-scan this beam across the scene. This beamforming can either be done in real-time in the analog domain, or post-sampling. The actual implementation of the receiver beamforming operation depends on whether the objects being imaged lie within the array near- or far-field.

- **Far-field beamforming:** To beamform in a particular direction in the far-field, the signal received at each antenna is delayed by an certain amount relative to the previous antenna. If the beam is to point at angle θ relative to array boresight, then each antenna output i is delayed by $\mathrm{delay}_i = id\sin(\theta)/c$, where d is the spacing between antennas and c is the speed of light [60]. This equation is the same as the one used in phased-array beamforming, with the phase offset instead expressed as a time delay. The delayed antenna outputs are then summed; hence this technique is often called delay-and-sum beamforming. The output of the summer is sampled at regular time intervals. The resulting stream of samples represent the reflectivity of the scene at increasing distances in the desired direction.

- **Near-field beamforming:** Near-field beamforming with timed arrays is also known as space-time beamforming [64], and focuses the received antennas on a single point

p, rather than in a particular direction. The propagation delay t_i from the transmit antenna to point p and back to each receiving antenna i is calculated. Let t_{max} be the maximum of all the delays t_i. The outputs of the receiving antennas are then appropriately delayed by $t_{max} - t_i$, so that the pulse reflected by point p reaches the end of each antenna's delay circuit at the same time. These delayed signals are then summed, and the output of the summer is then sampled at time t_{max} exactly. This approach ensures that only the reflection from point p is sampled. In practice, the output of the summer is usually time-gated so that a few samples before and after time t_{max} are recorded, allowing the output of the summer to be correlated with a prototype of the transmitted waveform (i.e. matched filtering). This process is repeated for every point p in the scene, with a unique set of time delays being calculated for every point. Note that near-field beamforming to a point is not possible with phased arrays; the cyclic nature of the signal phase results in multiple focal points in the near field.

These differences between phased arrays, far-field beamforming with timed arrays and near-field timed array beamforming is illustrated in Figure 7.1. For the types of applications and resolution requirements discussed thus far in this dissertation, a large timed array would be required, with all the objects lying within the array near field.
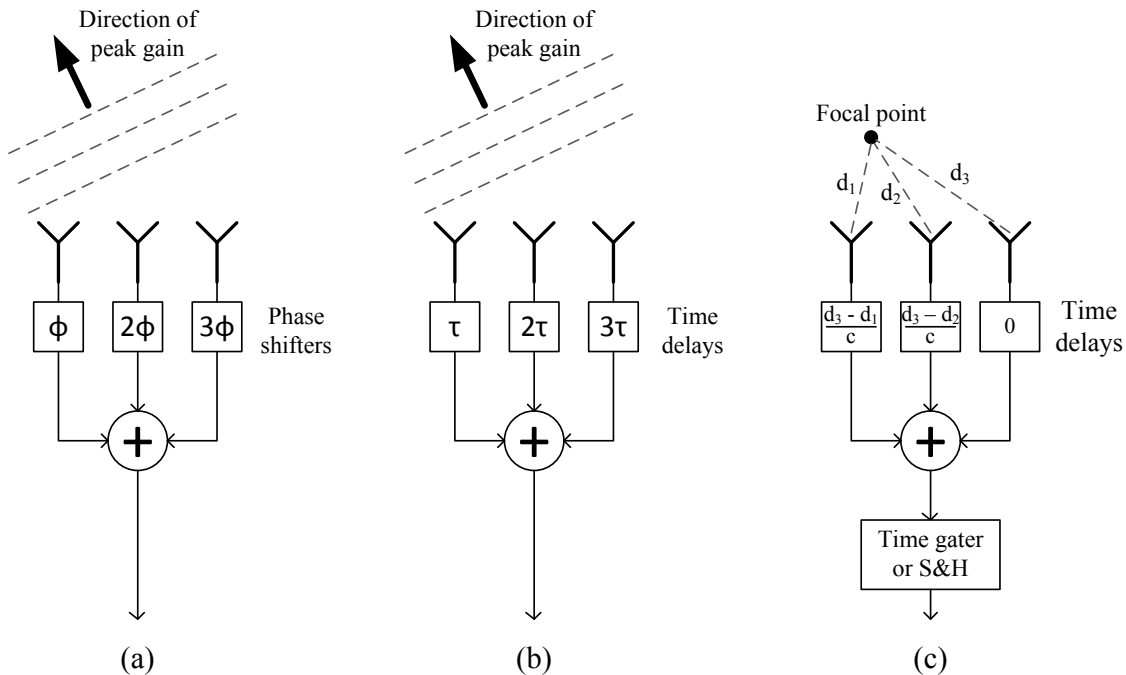
Figure 7.1: Comparison between (a) phased arrays, (b) timed arrays for far-field beamforming, and (c) timed arrays for near-field beamforming

7.1.2 Realizing time delays

Both near- and far-field timed array beamforming require the received signal to be delayed before summing. The three most common methods of implementing these time delays are:

1. Sample the receive antenna outputs at very high rate (typically > 20 GSps) and then delay and sum in the digital domain, such as in [64]. This approach allows all delays to be computed simultaneously, and hence the entire scene to be imaged simultaneously.

2. Use a fast sample-and-hold (S&H) circuit, with a precisely-delayed clock signal, at each antenna, for example [58]. The outputs of the S&H circuits are then summed and sampled at a slower rate. This process must be repeated for every voxel in the scene.

3. The output of each receive antenna is connected to variable-delay element, followed by a time gater or S&H. These delayed and gated/sampled signals are then summed in the analog domain and sampled with an ADC. The variable-delay element is usually implemented by (a) changing the path length by switching in additional traces, or (b) changing the wave velocity of the transmission line by switching in additional capacitance.

7.1.3 Requirements for high-resolution imaging

There are two main hardware requirements for a high-resolution timed-array imager: short transmit pulse widths and fast ADCs (or, alternatively, precise time delays). To achieve high image resolution, the transmitted signal needs to have a wide-bandwidth; hence, a very short pulse needs to be transmitted. Furthermore, the pulse also needs to be short enough to ensure that it has been completely transmitted before the first reflection is received. On the receive side, S&H circuits clocked with very precise delays; long delay chains with fine granularity; or very high speed ADCs are required to delay the received signals before summing. The exact requirements for an imaging system that is able to achieve similar image resolution to that of the RMA and compressive sensing imagers discussed thus far, will now be determined.

1. The pulse spatial length is given by cT, where T is the pulse duration. This term is equivalent to the wavelength of traditional microwave imaging systems. The maximum resolution achievable by the system is half the pulse spatial length. For a best-case image resolution of 10 mm, pulse spatial length must be ≤ 20 mm and $T \leq 60$ ps.

2. The resulting bandwidth of 60 ps pulse is approximately 15 GHz.

3. The depth resolution is given by $\text{Res}_{depth} = \frac{c}{2B} = \frac{cT}{2}$, where B is bandwidth. Therefore, the depth resolution is equal to the best case image resolution of 10 mm.

4. To achieve a cross-range resolution of 20 mm at 1 m range, an angular resolution of 1.1° is required. The beamwidth of a timed array, in radians, is usually given by

Beamwidth $= \frac{2cT}{L}$, where L is the length of the array in meters [61]. For a beamwidth of 1.1° and a pulse duration of 60 ps, an array length of 1.8 m is required.

5. While timed arrays do not exhibit grating lobes when antennas are placed more than $> 1\lambda$ apart, large sidelobes do start to develop. Simulation showed that placing the antennas 1.5λ apart kept these sidelobes within acceptable limits, while reducing the number of antennas. Therefore, with a 15 GHz bandwidth, 60×60 antennas are required to fill the 1.8 m 2-D antenna aperture with 30 mm spacing.

6. The time resolution of the delay and sample elements is determined by the angular resolution, as the angular resolution defines the smallest required delay between adjacent antenna elements. The required time resolution is given by $d \times \sin(Res_{ang})/c = 0.02 \times sin(1.1°)/c = 1.2ps$, where d is antenna separation.

7. Simulation showed that, in practice, this minimum delay can be increased to 20 ps without loss in resolution. This is because the time delay error at each antenna averages out when a large number of antennas are used.

8. The maximum relative delay between any two antennas occurs when an object is directly in front of an edge antenna. Assuming the object is 10 cm in front of an edge antenna, the distance to the furthest antenna is $\sqrt{1.8^2 + 0.1^2} \approx 1.8$ m. The difference in round-trip propagation time between these two paths is 12 ns. The system therefore needs to accommodate delays up to 12 ns, with 20 ps resolution.

9. If the antennas are sampled directly, a 50 GSps ADC is required to achieve the 20 ps time granularity, followed by a 600 element digital delay chain.

10. If a sample-and-hold circuit is used at each antenna instead, it needs to be triggered with picosecond accuracy. It is then followed by a variable delay element with a maximum delay of 12 ns and 20 ps resolution.

The main problem with using timed arrays for microwave imaging therefore lies in the unreasonable hardware requirements. If the antennas are sampled directly, no reasonably-priced ADCs are able to sample fast enough. If instead a S&H and delay circuit is used, the wide delay range that the delay circuit must support makes it unfeasible. This dissertation has therefore mostly concentrated on microwave imaging using phase measurements, rather than time delays.

7.2 Radio Interferometry

Radio interferometry is a technique used in radio astronomy to image stars and other astronomical objects. While the dimensions involved, and terminology used, is quite different to that found in microwave imaging, the rest of this chapter will show that radio interferometry

is actually very similar to many aspects of the near-field microwave imaging and timed array techniques presented thus far.

Figure 7.2 shows the Sub-Millimeter Array, an antenna array for radio interferometry. Unlike the 2-D antenna arrays investigated in earlier chapters, these interferometers typically operate with the antennas placed many wavelengths apart. The advantage of placing the antennas further apart is to increase the array aperture, resulting in a narrower beamwidth and hence better image resolution. While Chapter 4 showed that placing the antennas more than a wavelength apart results in large grating lobes and image aliasing, interferometers are able to get around this limitation by using a large signal bandwidth. This will be discussed in more detail later in this chapter.

Figure 7.2: The Sub-Millimeter Array (SMA) on Mauna Kea, Hawaii. The interferometer consists of eight antennas and is able to operate at wavelengths as short as 0.3 mm.
Image courtesy of The Harvard-Smithsonian Center for Astrophysics.

Despite the many similarities, there still remain a number of fundamental differences between radio interferometry and microwave imaging:

a.) Radio astronomers usually assume that the stars are infinitely far away, and hence that the wavefront, emitted by the stars, is a plane wave. This far-field assumption cannot be made for indoor microwave imaging, as the objects being imaged lie within the array near-field, and hence the curvature of the wavefront needs to be taken into account.

b.) Interferometers do not illuminate the stars and measure the reflected waves; instead, the stars emit their own microwave radiation. Therefore, to use interferometry for microwave imaging, this self-illumination will have to be approximated by illuminating the scene with a separate antenna.

c.) Interferometry generates 2-D images of the sky, while 3-D images with depth are desired for indoor microwave imaging.

Most interferometry algorithms are concerned with measuring the spatial-frequency plane, called the (u, v) plane by radio astronomers. The (u, v) plane is merely the 2-D Fourier transform of the plane in which the antenna array lies. Technically, this statement is only true if the array beam points directly upwards, but this detail can be omitted for purposes of this explanation. Keeping with the terminology used thus far in this dissertation, the antenna array is assumed to lie in the (x, y) plane and the Fourier transform of this plane is the (k_x, k_y) plane. Therefore, the (u, v) plane is identical to the (k_x, k_y) plane, and will be named as such.

The rest of this chapter will discuss how interferometers form images, starting with a small two-antenna array and working up to larger arrays. This chapter is not meant to be a complete summary of radio interferometry; only the main points relevant to indoor imaging are discussed. It should also be mentioned that interferometry is a far-field imaging technique, and so most of the discussion below assumes that the objects lie within the far field.

7.2.1 The two antenna interferometer

A two antenna interferometer consists of just two antennas connected to a correlator, via delay elements, such as in Figure 7.3. The correlator multiplies the two delayed antenna outputs, and can therefore be regarded as a downmixer. The correlator therefore operates differently than phased and timed arrays, where antenna outputs are summed. While the output of the correlator is often integrated to improve SNR, this step can be ignored for now without loss in generality.

There are two different ways to view how interferometers form images: beamforming, which is similar to how timed arrays work, and the measuring of spatial frequency components, which is more similar to microwave imaging. Although these two views refer to the same process, both are explained to provide a better understanding of radio interferometry.

Explanation in terms of beamforming

The beam formed by the two antennas in Figure 7.3 can be steered towards the source of radiation (i.e. star) by setting the delay on antenna A to $\Delta L/c$, i.e. the time it takes for the plane wave to travel distance ΔL. The delayed output of antenna A is then correlated with the output of antenna B. Since the two antennas receive the same signal, just offset in time, the output of the correlator will only output a strong signal (proportional to the power of the radiation source) if the two inputs to the correlator are perfectly aligned in time. Therefore, if a star does not lie in the desired direction (which is chosen by setting the delay τ), the signal from that star will not be aligned in time at the mixer inputs, and the output will be close to zero. Therefore, a narrow beam can be formed and pointed in different directions
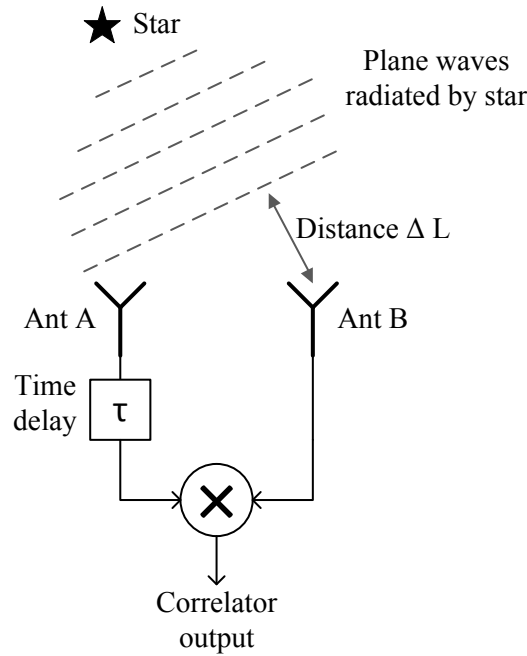
Figure 7.3: A two-antenna interferometer

by correlating the antenna outputs with different relative delays, each delay representing a different direction.

Since the two antennas are many wavelengths apart, one would expect grating lobes to occur. If the beam is pointed at a particular source such that $\Delta L = L_1$, then if any other stars are at locations such that $\Delta L = L_1 + \lambda$, where λ is the frequency at which the interferometer is operating, those stars will alias into the beam. For example, if the antennas are 2 m apart and operating at 20 GHz, one would expect grating lobes every 0.43° near boresight. However, interferometers are timed arrays and not phased arrays. Therefore, if the stars are emitting signals with sufficiently large bandwidths, the grating lobes will appear in different positions for each frequency, and average out to close to zero. This bandwidth requirement is equivalent to saying that the signal emitted by the star must not repeat within the time-of-flight across the array.

Therefore, a large separation between antennas gives a narrow beam, and provided the received signal has large enough bandwidth (or doesn't repeat very often), the beam will not exhibit grating lobes. Furthermore, this beam can be steered by changing the relative delay between antennas.

Explanation in terms of spatial frequency components

The vector between any two antenna locations is known as a baseline. This two-antenna interferometer therefore has a single baseline. Assume that the two antennas lie on the x-axis at positions $-d/2$ and $d/2$. In the spatial-frequency plane, this baseline represents two points

on the k_x axis at locations at positions $-d/\lambda$ and d/λ [65], where λ is the wavelength of the frequency of operation, as shown in Figure 7.4(a). There are two points, as one represents the vector from antenna A to B, while the other represents the reverse vector from antenna B to A.

Since these two points are the spatial-frequency representation of the array, taking the inverse Fourier transform will give the far-field beam pattern, as shown in Figure 7.4(b). The beam pattern is a sine wave, with side lobes as large as the main lobe, as expected from the inverse Fourier transform of two impulses.
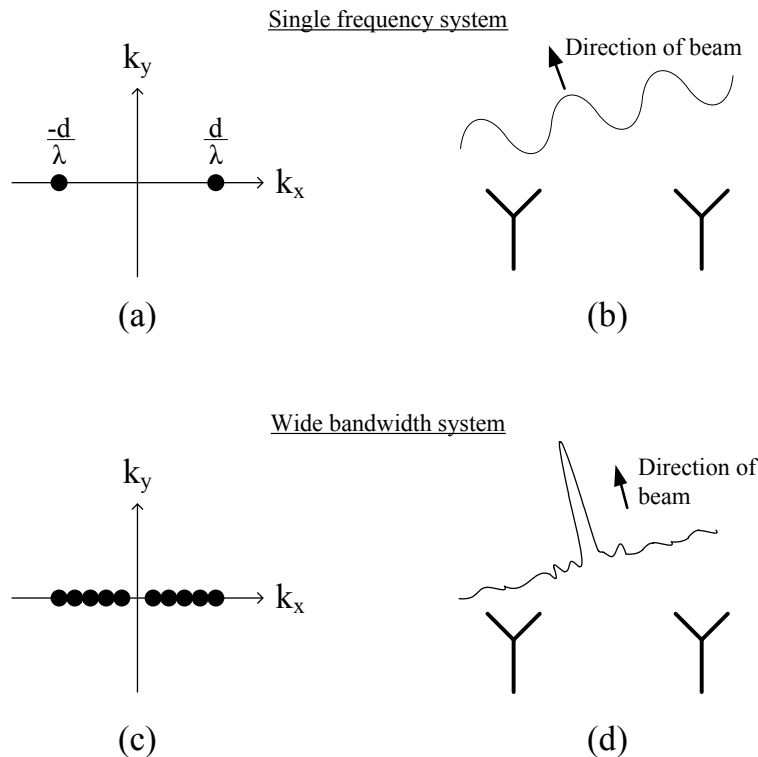
Figure 7.4: The spatial frequency plane, and corresponding radiation patterns, of the two antenna interferometer

Fortunately, interferometers do not operate at a single frequency, but rather over a wide bandwidth. As the operating frequency of the interferometer varies over its bandwidth from f_{min} to f_{max}, the effective length of the baseline between the antennas (in wavelengths) will vary too. Plotting this change in effective baseline length with frequency on the (k_x, k_y) plane, results in two lines along the x-axis, each from $\pm d/\lambda_{max}$ to $\pm d/\lambda_{min}$, as shown in Figure 7.4(c). Provided these lines extend almost down to the origin, the inverse Fourier transform of the (k_x, k_y) plane gives a narrow sinc, as shown in Figure 7.4(d). This sinc represents a much narrower beam, with beamwidth λ_{min}/d, in radians.

It was mentioned in the previous section that the two-antenna interferometer can form beams without grating lobes, provided the signal does not repeat for the time-of-flight, T_{flight},

across the array. This statement is equivalent to saying that the signal must contain frequency content at $1/T_{flight}$ Hz and below. Assuming that the normal operating frequency of the array is much higher than $1/T_{flight}$ Hz, the non-repeating signal requirement is therefore equivalent to the requirement that the signal must have a large bandwidth.

7.2.2 The four antenna interferometer

If four antennas are placed in a square, they will form the six baselines shown in Figure 7.5(a). Much like the two antenna case, if the system operates over a wide bandwidth down to (almost) 0 Hz, these baselines will mark out four lines in the (k_x, k_y) plane, as illustrated in Figure 7.5(b). This figure shows that the four antenna interferometer is able to measure both the k_x and k_y frequency components of the scene. The imaging process can again be identically described as beamforming or sampling the spatial frequency plane of the scene. While the latter explanation is typically used in radio astronomy, both explanations will be given here to emphasize the strong similarity between radio astronomy and timed-array microwave imaging.
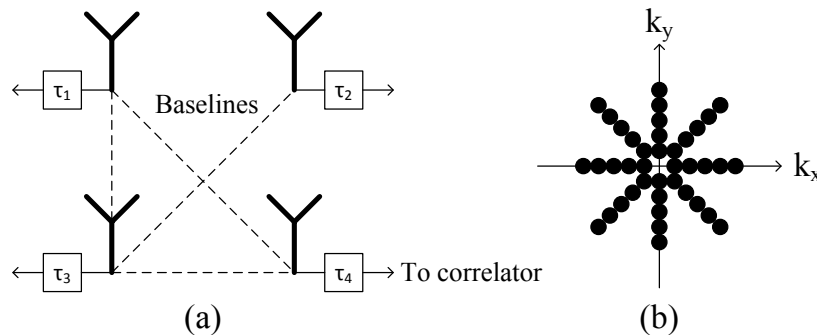
Figure 7.5: The four antenna interferometer and its baselines

Explanation in terms of beamforming

An image of the scene can be formed by correlating the output of each antenna with all the other antennas, over a range of relative delays and a wide measurement bandwidth. Again, the correlation is performed by mixing the different antenna pairs together with different relative days. In radio astronomy, the wide bandwidth might come from the emissions of the star. However, for indoor microwave imaging, this bandwidth is achieved by illuminating the scene with a wideband signal, such as a pulse or coded signal.

The output of the correlation between antennas A and B, over a range of delays τ, is merely the mixing and low-pass filtering of the two signals, such as:

$$Corr_{AB}(t, \tau) = Filt_{LPF}\{A(t) \cdot B(t - \tau)\} \tag{7.1}$$

Since the signals received at antennas A and B is identical, just shifted in time, the correlator output will be a DC signal, with the magnitude of the signal indicating how well the two antenna outputs are aligned in time. Therefore, the output of the correlator is constant with time t, and this term can be dropped from the expression for $Corr_{AB}$. The result is that $Corr_{AB}(\tau)$ gives a vector, with each element in the vector corresponding to a different time offset τ and hence beam angle.

The Fourier transform of this vector gives a set of spatial frequency measurements of the scene, along the baseline defined by the two antennas. Therefore, for each antenna pair, the correlation at different time offsets is calculated, the Fourier transform of the measurements is computed, and these measurements are used to fill in the points on the (k_x, k_y) plane, as indicated in Figure 7.5(b). The inverse 2-D Fourier transform of all these measurements on the (k_x, k_y) plane will give an image of the scene. However, as will be discussed in the next section, this image will be heavily distorted, as most of the spatial frequency plane is still missing.

Explanation in terms of spatial frequency components

Imaging with the four antenna correlator can also be regarded as directly sampling different points in the 2-D Fourier transform of the image. Equation 7.1, from the previous section, gave the expression for the output of the correlator for antennas A and B and time offset τ. Note that this is actually the expression for the convolution between the time-domain signals coming from antennas A and B. As described in the section above, taking the Fourier transform of this convolution will give all the points along this antenna pair baseline in the (k_x, k_y) plane. Using Fourier transform properties, we can write:

$$FT_{1D}\{A(t) * B(t)\} = FT_{1D}\{A(t)\} \cdot FT_{1D}\{B(t)\} \tag{7.2}$$

Therefore, by directly sampling the time samples from antennas A and B separately, taking the Fourier transform of the respective signals, and then multiplying the two resulting frequency-domain signals, all the (k_x, k_y) samples along that baseline can be obtained [66]. Furthermore, each signal no longer needs to be explicitly delayed before sampling. In practice, this method can be used to create a 2-D image of a room using the following steps:

1. For each RF frequency f in a range of frequencies:

   a) Use a separate antenna to illuminate the scene with a CW signal at frequency f.

   b) Measure the magnitude and phase of the reflected signal received at each antenna, relative to the transmitter.

   c) For each receive antenna pair: multiply together the complex samples collected at each antenna in the previous step. Write the resulting complex number to the point in the (k_x, k_y) plane that corresponds to this antenna pair at this frequency f.

d) Repeat for each frequency step.

2. Take the inverse 2-D Fourier transform of the (k_x, k_y) plane to get the 2-D image of the scene.

Since the four antenna interferometer only samples four distinct lines in the (k_x, k_y) plane, the inverse 2-D Fourier transform will typically result in a rather distorted image of the scene. Radio astronomers solve this problem by using the rotation of the earth to rotate the entire antenna array with respect to the fixed scene (i.e. the sky). In this case, the four lines in the (k_x, k_y) plane rotate to create a filled circle of samples. Without this rotation, the only way to form a reasonable image is to interpolate the missing spatial frequency samples using a model of the scene. However, interpolation is not straightforward when imaging complex objects such as people.

It must also be mentioned that interferometry allows a regular 2-D array of antennas to be replaced by just a few antennas placed many wavelengths apart. This reduction in antennas is made possible by using a signal of large bandwidth. While this approach works well for radio astronomy, where depth is not measured, it may be less suitable if one wants to use frequency information to measure depth, such as is done in 3-D RMA.

7.2.3 Costas arrays

Since a four antenna interferometer only samples a small fraction of the (k_x, k_y) plane, clearly more antennas are required to obtain high quality 2-D images of an indoor environment. A fully-populated 2-D rectangular antenna array would clearly give all the points in the spatial frequency plane. However, it turns out that a full 2-D array is not actually required, as it contains many repeating baselines.

A Costas array provides a means of filling a gridded 2-D space so that no baseline vectors are repeated [67]. Costas arrays are defined mathematically as a $N \times N$ array containing N 1s, with the rest of the array set to 0. The 1s are placed so that each row and each column contains only a single 1, and that all of the displacement vectors (i.e. baselines) between the 1s are distinct [68]. Figure 7.6 shows an example of a 5×5 Costas array.
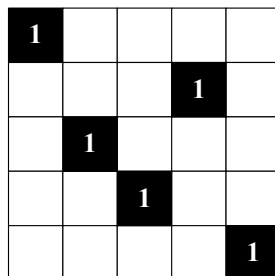
Figure 7.6: A 5×5 Costas array. All empty cells are zero.

If we regard the Costas array as representing a grid of $N \times N$ possible antenna locations, with the 1s indicating the placement of the N antennas, the resulting array will contain a unique set of baselines with no redundancy. For reasonably-sized antenna arrays, it has been found that Costas arrays typically sample 25 to 50% of the (k_x, k_y) plane [67]. This result indicates that less than $4N$ antennas are required to sufficiently sample the entire (k_x, k_y) plane. Therefore, for a 64×64 antenna array aperture, only $64 \times 4 = 256$ antennas are at most required, representing a 6% fill factor. Costas arrays hence allow sparse antenna arrays to be designed for microwave imaging, with sparsities similar to those achieved by compressive sensing.

The Costas arrays have thus far assumed that the system operates at a single frequency. Increasing the bandwidth effectively creates more baselines, allowing the number of required antennas to be reduced further. Alternatively, instead of using bandwidth to reduce the array size, it may be possible to use RF bandwidth to measure depth and hence obtain 3-D images. This approach, however, requires further investigation.

7.2.4 The cross interferometer

A common array pattern used in radio interferometry is the cross, such as the Mill's Cross array shown in Figure 7.7. If the array is of length L along each axis, then plotting all the possible baselines on the (k_x, k_y) plane will completely cover the plane between $\frac{-L}{2\lambda}$ and $\frac{L}{2\lambda}$ on each axis. A dense 2-D array of the same size will fill the (k_x, k_y) plane between $\frac{-L}{\lambda}$ and $\frac{L}{\lambda}$. Therefore, the cross interferometer will have twice the beamwidth (and hence only half as good resolution) of a dense 2-D antenna array.
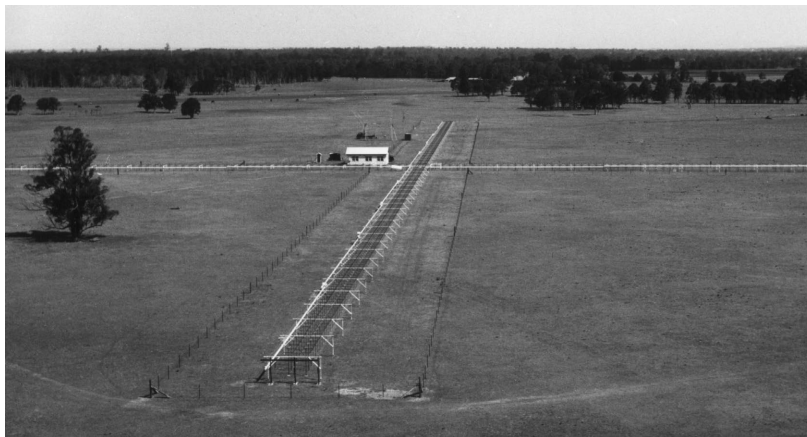
Figure 7.7: The Mills Cross array for radio astronomy at CSIRO, Australia.
Image courtesy of the Australia Telescope National Facility Historic Photographic Archive.

This result is the same that was found when comparing the X-MIMO array to the colocated array for RMA microwave imaging. Furthermore, in the X-MIMO array, the signal transmitted from each antenna on the one axis was mixed with the signal received at each

antenna on the other axis. This mixing of signals is identical to correlating different antenna pairs, as is done in interferometry. This comparison is yet another indication of the strong link between microwave imaging and radio interferometry. The only difference between the algorithms is the measurement of depth and the correction of the near-field wave curvature.

7.2.5 Interferometry within the array near-field

Despite most radio interferometers being used to image distant stars, there has been recent work on using a w-projection technique to accommodate for the curvature of the wavefront and hence allow imaging of objects that lie within the array near-field [69]. This algorithm is slightly more computationally intensive than the correlation algorithm described above, but uses the same number of antennas. Since the algorithm is already compensating for changes in depth caused by the curvature of the wave, it could potentially be modified to create images at multiple depths, allowing 3-D images to be formed. This suggests that it may be possible to use interferometry for indoor 3-D microwave imaging.

7.3 Conclusion

Two new methods for capturing microwave images were introduced in this chapter, namely timed arrays and radio interferometry. Although these methods are rarely used for indoor imaging, they do share many similarities with the existing microwave imaging methods discussed in earlier chapters.

Timed arrays usually operate in the array far-field. They are able to capture images by first forming a narrow beam (i.e. beamforming), and then raster scanning this beam over the scene. However, for operation in indoor environments, timed arrays can instead be used to image objects within the array near-field by focusing on a spot, rather than in a direction. Timed arrays initially seem attractive due to the simplicity of operation. However, it was found that the hardware requirements for imaging a room-sized volume at a reasonable resolution with a timed array was unfeasible, especially in terms of ADC sampling rate, time resolution and delay chain lengths.

Although radio interferometry initially does not seem well suited for indoor microwave imaging, it was shown that interferometers are actually very similar to timed arrays. Most of the apparent differences between radio interferometry and timed arrays lie in the terminology. Much like timed arrays, radio interferometers require large bandwidths to image correctly. However, instead of delaying and summing the antenna outputs, as is done in timed arrays, the antenna outputs are instead delayed and correlated with a mixer. An alternative, and more scalable approach, is to sample each antenna output directly, and then correlate the Fourier transforms of the different antenna outputs with each other.

The main attraction of radio interferometry for microwave imaging is the reduction in the number of required antennas. Interferometers are able to produce high quality 2-D images from 2-D arrays that are 94% sparse. The disadvantage is that interferometry requires

extremely large bandwidth, with the lower end near DC, and is a far-field imaging technique that produces 2-D images, not 3-D images. However, recent work on w-projection techniques indicate that it may be possible to adapt interferometry for 3-D imaging within the array near-field. It will be interesting to see this work taken further.

Chapter 8

Design of a Real-time Microwave Imaging System

All microwave imaging experiments described thus far were performed using the XY-table antenna array simulator. The mechanical nature of the XY-table meant that these experiments took many hours to capture a single image, prohibiting real-time imaging. Therefore, it has not been possible to image humans as they move around, which is the main application of this technology.

This chapter therefore describes the architecture of a real-time microwave imaging system, consisting of a 2-D array of a few hundred antennas and radios. The decisions driving the design of the system, as well as performance measurements of a small prototype system, will be discussed.

8.1 Selection of Imaging Algorithm and Array Parameters

The design process begins with the selection of the microwave imaging algorithm, the antenna array size and the operating microwave frequency. Since the goal of this system is to image people as they move about in a room, the chosen design parameters must ensure a resolution of 25 mm (1") at 1 m and a frame rate of 10 frames/second (fps), or better. While this resolution is probably not good enough to image individual fingers on a human hand for gesture recognition, it is sufficient for a proof-of-concept real-time imaging system.

8.1.1 Imaging Algorithm

There are three possible classes of microwave imaging algorithms that can be used for the real-time system: dense array algorithms (colocated, MIMO and single-transmitter RMA), X-MIMO RMA, and compressive sensing for sparse arrays. These algorithms have all been discussed thoroughly in previous chapters, so only a brief summary is given in Table 8.1.

Table 8.1: Comparison of different imaging algorithms for the real-time imaging system

Algorithm	Advantages	Disadvantages
Colocated RMA	Highest possible resolution	Requires $N \times N$ antennas
N_{TX} M_{RX} MIMO RMA	Faster imaging, improved SNR	Requires $N \times N$ antennas, ½ resolution of coloc RMA
Single-TX MIMO RMA	Fastest imaging	Requires $N \times N$ antennas, ½ resolution of coloc RMA
X-MIMO RMA	Fewest ($2N$) antennas required	½ resolution of coloc RMA
CS for sparse arrays	Few ($< 10\%$) antennas required	Computationally slow

A nominal antenna array size of 64×64 is required. An array of this size gives sufficient resolution to image people, as was shown in Chapter 4. It also results in images that are 64×64 pixels in the cross-range dimensions, which is about the lowest usable resolution for a useful imaging system. With this array size, the first three RMA algorithms can immediately be rejected. These algorithms all require 4096 antennas for this desired array size. Even if the array dimensions are reduced to 32×32 antennas, 1024 antennas and RF transceivers will still be required. Assuming that each antenna and transceiver can be built for under $100, the cost of the system remains prohibitively expensive.

The next option is to build a sparse antenna array of a few hundred antennas, and use the compressive sensing algorithm from Chapter 6 to form images. This array would be more affordable, but the computational complexity of the compressive sensing algorithm makes it too slow for real-time imaging. While the algorithm could be optimized for faster performance, or implemented on specialized hardware such as FPGAs or GPUs, this work would require more man-hours than were available.

Therefore, the only viable option is to build an X-shaped array, where the transmit antennas are placed in a linear array on the vertical axis and the receive antennas are placed in a linear array on the horizontal axis, forming a rotated X-shape. The antenna reflections are then processed using the X-MIMO RMA to form 3-D images. While using an X-MIMO array does mean that the resulting image resolution will only be half as good as that obtained from a similar sized full 2-D array, this loss in resolution is acceptable for a proof-of-concept prototype.

8.1.2 Array Size and RF Frequency

The cross-range resolution of the images produced by a microwave imaging system is determined primarily by array size and RF frequency. Chapter 4 showed that increasing the antenna array aperture increases the resolution until the half-wavelength resolution limit is reached. More accurately, array aperture determines the angular resolution of the system;

a larger aperture gives a smaller angular resolution. Therefore, the image resolution is determined by both the array aperture and the distance to the object being imaged. The RF frequency determines the maximum achievable resolution of the system ($\lambda/2$), irrespective of distance.

In most cases, the objects being imaged are at considerable distance from the array, and so the resolution is aperture limited. The resolution limit dictated by the RF frequency only becomes important when objects are very close to the array. This relationship is illustrated more clearly in Figure 8.1. This figure shows the theoretical resolution achieved by the X-MIMO algorithm for different array sizes, frequencies and distances from the array. The highest resolution is achieved with the largest array (128×128) at the closest distance (0.5 m). The 128×128 curve in Figure 8.1(a) shows that below 15 GHz, the frequency limits the image resolution. However, above 15 GHz, frequency has no effect on resolution. This knee in the curve decreases in frequency as the array size decreases, or as distance increases.

The 1.0 m range plot is of most interest to the real-time imaging system, as we expect most objects to be at this distance for the demonstration. At this distance, a 64×64 X-MIMO array (128 antennas total) achieves a resolution of 22 mm at 10 GHz or above. At a 2 m range, the resolution is still a reasonable 44 mm. While no commercial RF bands exist at 10 GHz, there is an automotive radar band at 24 GHz, for which commercial radio transceivers ICs already exist.

The real-time imaging system will therefore consist of 128 antennas, arranged in a 64×64 X-MIMO pattern, operating at 24 GHz.

8.2   Hardware Architecture of the Imaging System

With the array size, imaging algorithm and operating frequency decided, the next step is to determine how best to manifest the array in real hardware. Figure 8.2 shows a proposed modular array design. A number of RF daughtercards are plugged vertically into a backplane board. Each daughtercard contains a single antenna and a complete radio transceiver. Therefore, a separate daughtercard is required for each antenna in the array. While this design does increase the manufacturing cost slightly, it drastically reduces risk: if a single transceiver fails, or has a manufacturing defect, that daughtercard can be simply swapped out.

The other advantage of the proposed modular design is that its 3-D structure provides more space in which to pack the antenna and transceiver components. Even in the X-MIMO array, the antennas still need to be less than a wavelength apart (12 mm at 24 GHz). If the entire array was built on a single flat PCB, the PCB would be extremely densely populated.

After receiving, downconverting and sampling the reflected RF signal, each daughtercard needs to communicate these samples to a central hub for image processing. To minimize transmission line losses, the receive signal is first digitized on each daughtercard before being communicated over a digital bus on the backplane carrier board. A single FPGA,
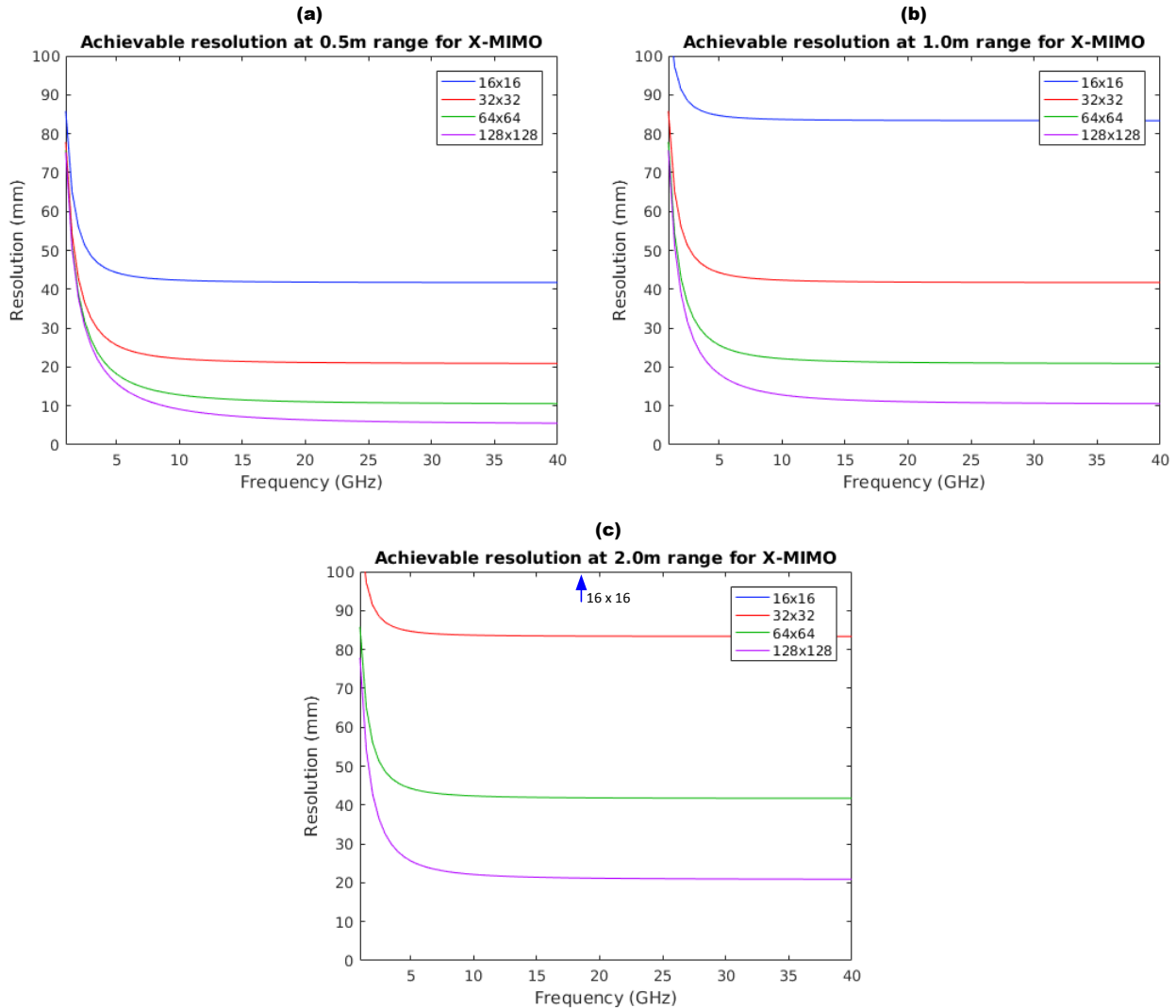
Figure 8.1: Theoretical resolution achievable by the X-MIMO algorithm at different array sizes, frequencies and distances

connected to this bus, collects the received signals from each antenna, and sends them, via Ethernet, to a desktop computer running the X-MIMO RMA.

To keep the local oscillators on all daughtercards synchronized, a low-frequency clock signal is also distributed on the backplane to the daughtercards. Since there are only 128 daughtercards, clock distribution is achieved using clock buffers and a tree structure. A phase-locked loop (PLL) on each daughtercard converts this clock signal to a high-frequency RF clock.
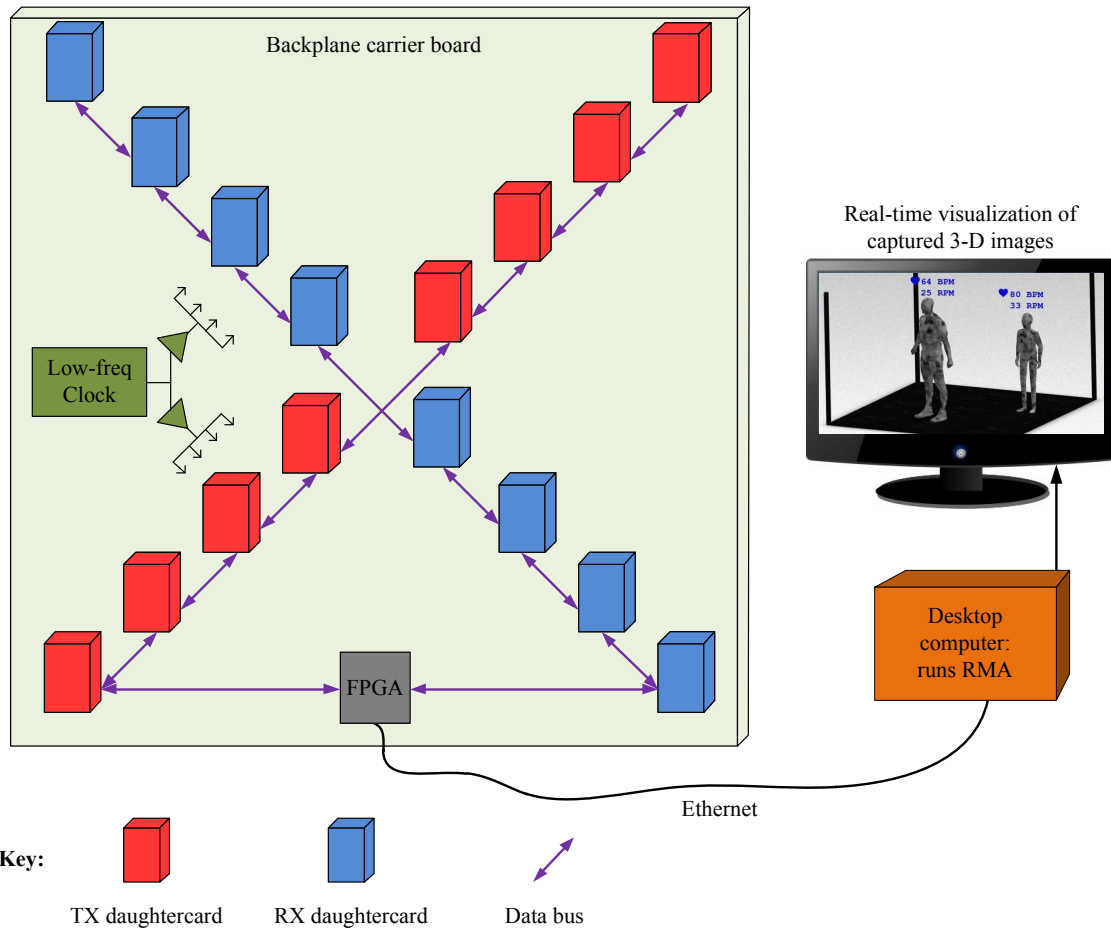
Figure 8.2: Architectural block diagram for the real-time microwave imaging system. Although only 16 daughtercards are shown, the actual system will consist of 64 TX daughtercards and 64 RX daughtercards, each containing an antenna and RF transceiver.

8.3   RF Daughtercard Design

Each daughtercard is a complete radio, containing all the components required to transmit microwave signals and sample the reflected waves. These components include the antenna, amplifiers, mixers, RF oscillators, baseband circuitry and ADCs. The daughtercard also contains a microcontroller for control and synchronization. The primary goal when designing the daughtercard was to minimize cost, as 128 of the cards will be built for the real-time imaging prototype, and potentially more for future arrays. The target manufacturing cost for components, assembly and testing was $100 per card in volume. To meet this goal, custom components and specialized manufacturing processes were avoided. An attempt was also made to keep the boards as universal as possible without increasing cost, so that they can be used in different array configurations in the future, such as sparse arrays for compressive

sensing imaging.

8.3.1 System diagram

Figure 8.3 shows the system block diagram of the resulting daughtercard design that best meets the criteria listed above. The most important component of this system is the RF transceiver, for which the Infineon BGT24MTR11 24 GHz monolithic microwave integrated circuit[1] was selected. This part was chosen because it provides a complete 24 GHz RF frontend with a wide 4 GHz bandwidth and a unit price of just $9 in large volume. Figure 8.4 shows the inner structure of the BGT24 device. The daughtercard architecture, including the RF frontend, is described below.
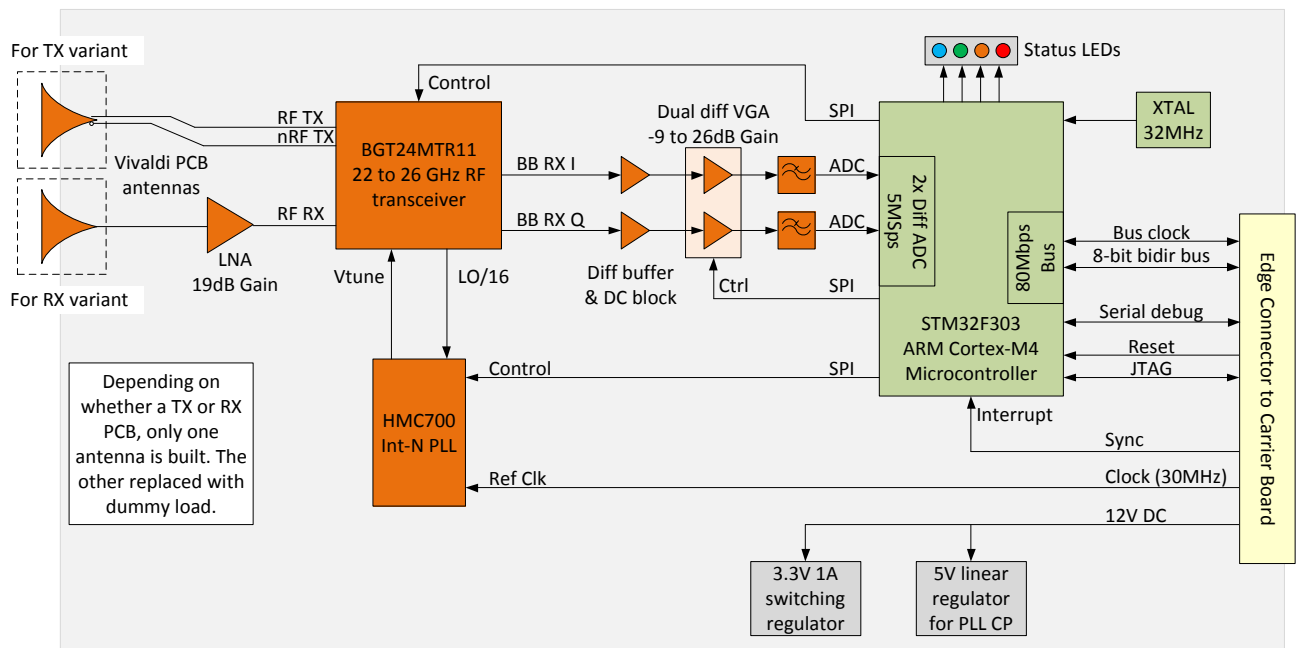
Figure 8.3: System block diagram for the RF daughtercard

- **Antennas:** The BGT24 has separate transmit and receive antenna ports, with one port differential and the other single-ended. Although antenna switches and circulators were considered, these are not easy to design nor easily available at 24 GHz. Therefore, two separate antennas are required. Unfortunately, there is only enough space for one antenna, as the RF daughtercards need to be narrow to pack together. Therefore, two different daughtercard were designed: a transmit variant and a receive variant. These two variants differ only in how the antenna ports are connected:

---

[1]https://www.infineon.com/cms/en/product/rf-and-wireless-control/
mm-wave-mmic/24-ghz-radar-industrial/BGT24MTR11/productType.html?productType=
db3a30443ff7943901400b1ba90516fa
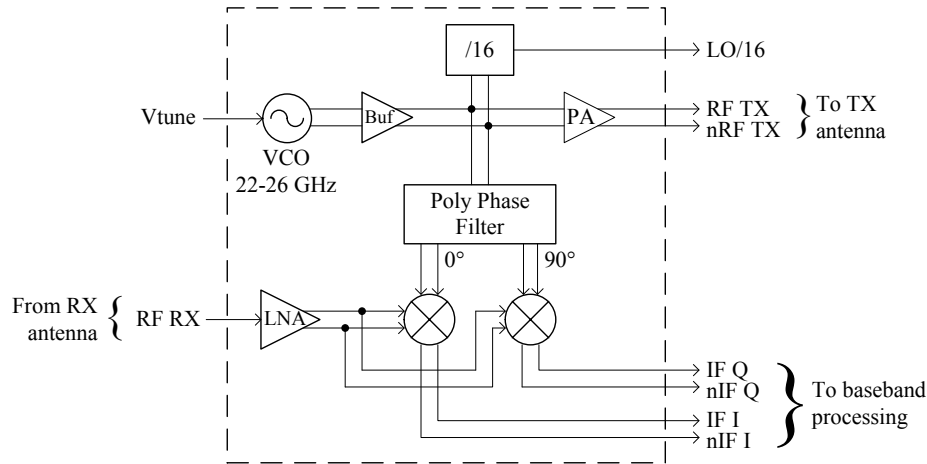
Figure 8.4: Block diagram for the BGT24MTR11 radio transceiver integrated circuit

- *Transmit daughtercard:* The BGT24 antenna transmit ports directly drive a differential Vivaldi antenna. The LNA input port is grounded. The LNA output port drives the BGT24 receive antenna port.

- *Receive daughtercard:* The BGT24 antenna transmit ports drive a dummy load. The LNA input port is connected to a single-ended Vivaldi antenna. The LNA output port drives the BGT24 receive antenna port.

Therefore, the same components and placement can be used for both variants: only the antenna and the routing of three traces changes.

- **RF transmitter:** On the transmit card, the BGT24 uses a free-running voltage-controlled oscillator (VCO), connected to an internal power amplifier (PA), to drive the transmit antenna. The VCO, which can operate between 22.5 and 26.5 GHz, is controlled by an external Hittite HMC700 PLL. The output power of the PA is digitally controllable from 2 to 11 dBm.

- **RF receiver:** On the receive card, the antenna is connected to a Macom MAAL-011111 LNA with 19 dB gain. The purpose of this LNA is not to improve the noise-figure (NF) of the receiver, but rather to mitigate the effects of local oscillator (LO) to receive signal leakage inside the BGT24. The output of the Macom LNA connects to the antenna inputs on the BGT24, where it is further amplified and mixed with the VCO output. The mixer output is outputted as baseband I and Q signals to the rest of the receive chain.

- **Baseband receiver chain:** The receiver baseband signals contain a DC offset that is first removed using a 2 Hz high-pass filter. The signals then pass through a dual variable-gain amplifier (VGA), with gain digitally controllable from -9 to +26 dB,

before being anti-alias filtered and sampled by two differential ADCs. These ADCs are integrated into the ARM microcontroller and operate at 5 MSps (the baseband signal is expected to be between DC and 1 MHz). There is no baseband transmit chain, as the transmit signal is controlled solely by manipulating the VCO on the BGT24.

- **ARM microcontroller:** The whole daughtercard is controlled by a STM32F303RE ARM Cortex-M4 microcontroller. This part was chosen due to its low cost ($5) and integrated ADCs. Although these ADCs are fairly noisy, it was shown in Chapter 5 that the microwave imaging algorithms can tolerate a reasonable amount of random noise. The microcontroller uses a number of its GPIO (general purpose input/output) pins to create a parallel bus for sending the received samples off the daughtercard. The bus interfaces on the different daughtercards are connected together on the carrier board to form a large ring network.

- **PLL:** The VCO on the BGT24 is clocked by a Hittite HMC700 PLL. The PLL receives a 30 MHz reference clock from the carrier board. The PLL compares this clock signal to a divided-down version of the BGT24 VCO clock, and uses a charge pump to control the voltage of the BGT24's VCO so that these two clock signals are phase and frequency locked. Since the PLLs on all the daughtercards receive the same reference clock signal, all the BGT24 RF transceivers should operate at the same frequency, with just a constant phase offset.

- **Power, reset and debug:** The carrier board supplies each daughtercard with 12V power. Each daughtercard contains regulators to generate the necessary supply rails. JTAG and serial signals are provided over the edge connector for programming and debugging. Finally, the edge connector also provides synchronization and reset signals to reset the microcontroller and indicate the start of capture of each imaging frame.

8.3.2   PCB and antenna design

A 6-layer PCB was designed in Altium Designer. Due to the high-frequency nature of the RF frontend, Rogers RO4350B[2], an affordable hybrid woven-glass/ceramic laminate with good dielectric properties at high frequencies, was used for the outer dielectric layers. FR-4 was used for the inner dielectric layers to minimize cost. Every effort was made to keep the PCB as narrow as possible to allow multiple daughtercards to be densely packed to form an array. A rendering of the final PCB design is shown in Figure 8.5. All the high-frequency signals and components were placed as close to the antenna as possible, and only on the outer PCB layers, to minimize interference and simplify the design.

As was mentioned earlier, two variants of the daughtercards PCB were built: a transmitter card and a receiver card. Since the BGT24 transceiver has a differential transmit antenna port, but a single-ended antenna receive port (the external LNA is also single-ended), it was

---

[2]`https://www.rogerscorp.com/acs/products/55/RO4350B-Laminates.aspx`
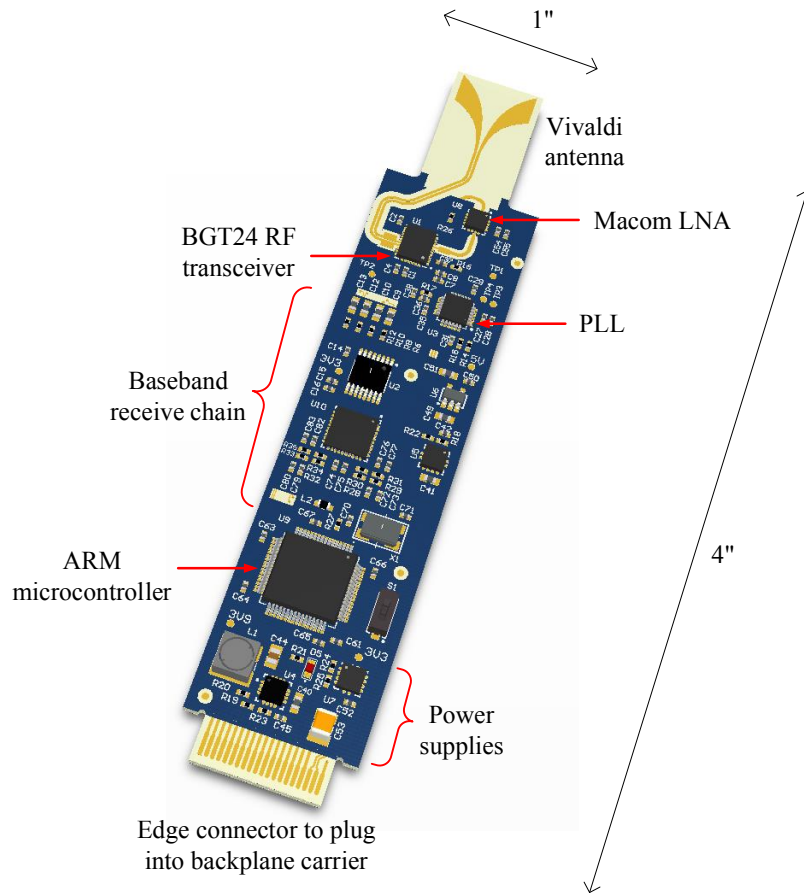
Figure 8.5: 3-D model of the PCB for the transmit daughtercard
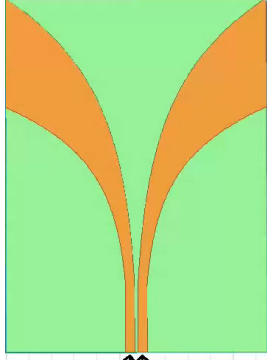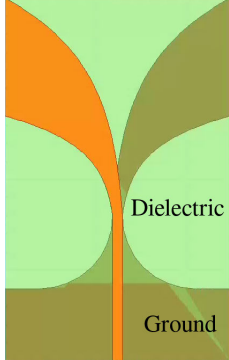
deemed best to design two different antennas to maximize compatibility with the BGT24 antenna ports. These antennas were designed in HFSS and their simulated performance characteristics are shown in Table 8.2. Vivaldi antennas were used in both cases, as they were shown in Chapter 4 to be well suited to microwave imaging.

8.3.3   RF frontend analysis: gain, SNR and power

Special care was required when designing the RF frontend, due to the limited acceptable power range for the received signal into the BGT24 RF transceiver. The RF received signal into the BGT24 needs to lie between -30 and -15 dBm. Above -15 dBm, the receiver starts to saturate and unwanted harmonics and distortion occurs. Below -30 dBm, the leakage from the LO to the receiver antenna input, inside the BGT24, becomes larger than the actual received signal. If the received signal is at the same frequency as the LO, the received signal needs to be larger than -30 dBm for it to be easily detectable

Table 8.3 shows the link budget calculations for the entire system, with a typical person being imaged at 0.5 and 1 m distance. The main figures of interest, shown in bold, are the

Table 8.2: The antennas used in the RF daughtercards

	Transmitter Antenna	Receiver Antenna
HFSS model	Differential feed	Single-ended feed
Antenna type	Differential Vivaldi	Antipodal Vivaldi (single-ended)
Frequency range	18 - 35 GHz	20 - 29 GHz
Gain	4.9 dBi	4.5 dBi
Return loss	> 16 dB	> 16 dB
Beamwidth	70°	70°

power levels at the output of the LNA and the ADC. The signal power at the output of the LNA is the same as the power into the BGT24 receiver, which needs to be between -30 and -15 dBm. With an object at 1 m range, the signal level is right at the bottom of this range. It should now be clear that due to the large path and reflection loss, the external LNA is required to keep the received signal power above the level of the LO leakage.

These results indicate that if an object is placed more than 1 m away from the antenna array, the returned signal level will be less than the LO leakage, potentially making the signal difficult to separate from the leakage. Interestingly, the evaluation kit for the BGT24 transceiver appears to operate with even lower received signal levels. This issue will therefore be investigated later in this chapter, including using filters to separate out the leakage.

It may appear strange that the power gain of the BGT24 receiver is -5 dB, even though it contains an amplifier. The BGT24 receiver actually provides 20 dB of voltage gain, but since it has very high output impedance, the power gain is significantly lower. The output of the BGT24 receiver is fed through a VGA, which is able to keep the input signal to the ADC very close to its full-scale input of -9 dBm for both 0.5 m and 1 m ranges.

The noise figure of the the receive circuit is dominated by the external LNA, which has a noise figure of 2.5 dB. However, as mentioned, a much bigger concern is the BGT24 internal LO to receive antenna input leakage.

The power consumption of the RF daughtercard is, unsurprisingly, much higher than that achievable by a single integrated circuit solution. However, at 2 W per card and 280 W for the entire array, the power consumption is still reasonable for a proof-of-concept system.

Table 8.3: Calculating the received signal power for objects placed at different distances

Component	Gain (dB)	Input P1dB (dBm)	Output Power (dBm) @ 0.5m	Output Power (dBm) @ 1m
BGT24 transmitter			11	11
Transmit antenna	5		16	16
Reflection + path loss	-60 to -72		-44	-56
Receive antenna	5		-39	-51
External LNA	19	-14	**-20**	**-32**
BGT24 receiver	-5	-12	-25	-37
VGA	-9 to 26	13	-10	-11
ADC	0	-9	**-10**	**-11**

8.4   Clock Generation and Distribution

To accurately measure the roundtrip phase from the transmitter, to each point in the scene, and back to each receiving antenna, the local oscillators in the RF transceivers need to be phase locked together. A constant offset in the phase between the different LOs is acceptable, as long as this offset remains fixed and can be measured using a calibration step. It is envisioned that the calibration step will involve imaging a small metal sphere placed in a known location in front of the array. Since the distance between each antenna and the sphere is known, the phase offsets can be calibrated out. However, any frequency deviation at the LOs is not acceptable. A common low-frequency reference clock signal is therefore distributed, using a clock tree, to all the RF daughtercards, where it is converted to a 24 GHz RF clock using a PLL. The clock distribution scheme is shown in Figure 8.6.

Low clock jitter is required, as the microwave imaging algorithms work by measuring the phase delay between transmit/receive antenna pairs and different points in the scene. Any jitter will introduce errors into these phase measurements. Since the imaging algorithms make these measurements at many different carrier frequencies, fast frequency switching is also required if the imaging system is to operate in real-time.

Using fractional-N PLLs on the daughtercards would have made image acquisition faster, since they typically have faster settling times than integer-N PLLs [70]. However, using fractional-N PLLs was not possible for this application, as there would no way to guarantee a constant phase offset between the RF clocks on the different daughtercards. This is because the RF clock frequency is not an integer multiple of the reference clock in the case of fractional-N PLLs. Specifically, if the PLL multiplies the reference clock by $N + \frac{K}{F}$ to generate the RF clock, then the VCOs on the different daughtercards will each have a phase offset of $\frac{2\pi i}{F}$, for integer i randomly chosen from $[0, F - 1]$ [71]. Even if this phase offset between the different VCOs is measured, it will change randomly every time the frequency is changed.

A integer-N PLL is therefore used on each daughtercard instead. To step the RF clock from 22 to 26 GHz in 31.25 MHz increments (i.e. 128 frequency steps), the reference clock
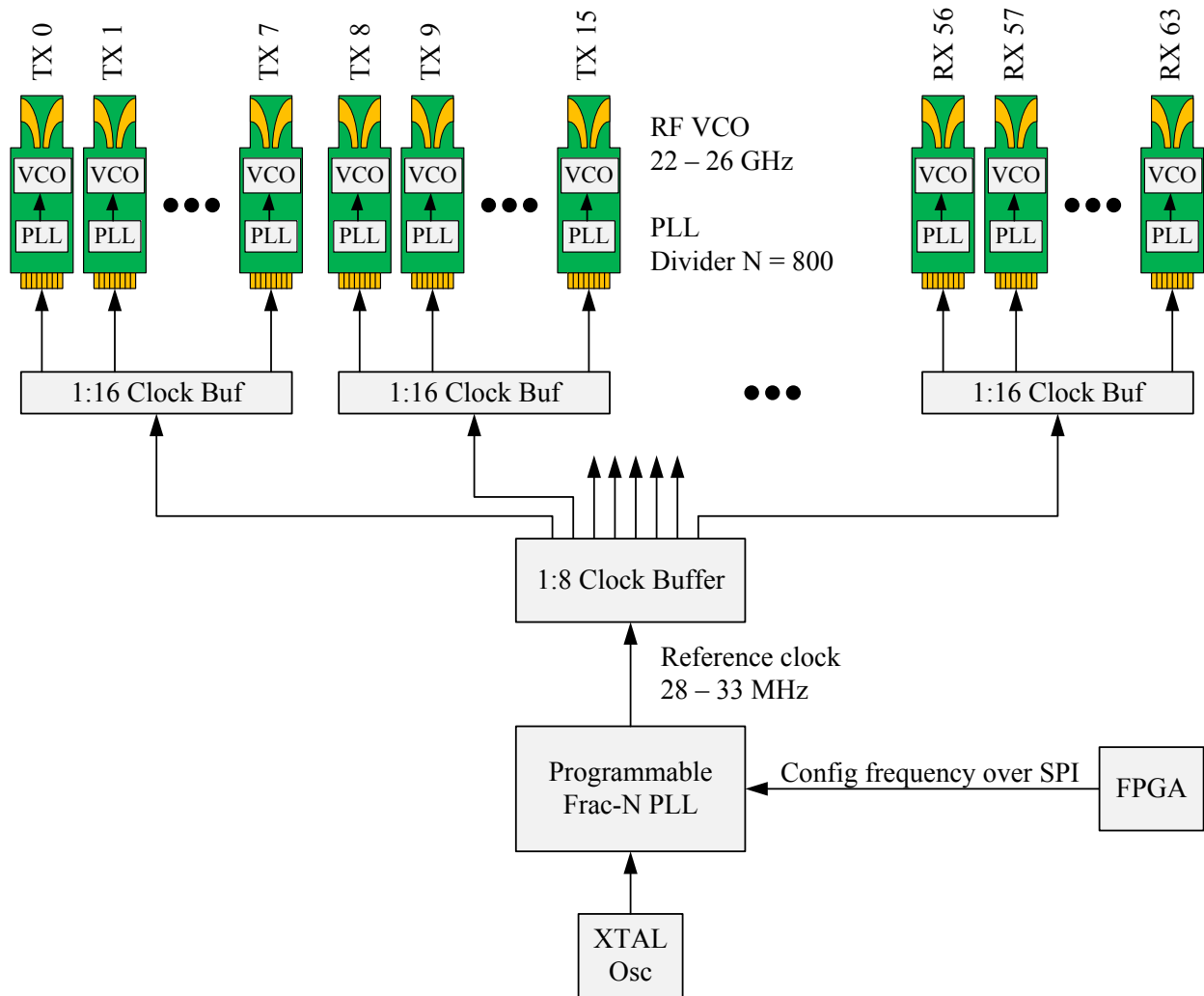
Figure 8.6: The clock distribution scheme for the real-time prototype

would need to be ~ 2 MHz. Driving each daughtercard PLL with a such a low frequency reference clock may cause phase noise problems. The proposed solution is therefore to generate a 30 MHz reference clock using a common fractional-N PLL, and distribute this 30 MHz reference to all the daughtercards. The PLLs on the daughtercards will then convert this 30 MHz signal to the 24 GHz band. To change the RF frequency from 22 to 26 GHz, the central fractional-N PLL simply changes the distributed clock from 28 to 33 MHz, while the integer clock division ratio on the daughtercard PLLs remains constant.

Being able to quickly switch operating frequencies is essential for real-time imaging. This requirement means that the PLLs on the daughtercards need to "settle" (i.e. reacquire phase lock) as soon as possible after the reference clock changes frequency. The loop filter, which sits between the PLL output and the VCO input on the daughtercard, was therefore de-

signed to have a large 450 kHz bandwidth to enable the PLL to settle as fast as possible without increasing jitter beyond acceptable levels. Unfortunately, some filter components were swapped for different values during manufacturing, resulting in a 60 kHz loop bandwidth. Even with this reduced loop bandwidth, simulation shows that each integer-N PLL output should settle to within 10 Hz of the desired frequency and 1° of the desired phase in just 95 µs, after a step in the reference frequency. The total time required to capture an image frame is therefore calculated below. T_{samp} is the time required to sample the reflected signal at each receive daughtercard, while T_{sw} is the time required to turn each transmitting antenna on or off.

$$
\begin{aligned}
T_{frame} &= N_{freq} \times (T_{settle} + N_{TX}\,(T_{samp} + T_{sw})) \\
&= 128 \times (95\mu s + 64\,(3\mu s + 0.5\mu s)) \\
&= 40 \text{ ms} \qquad (25 \text{ frames/s})
\end{aligned}
\tag{8.1}
$$

8.4.1   Clock jitter

With a reference clock of 30 MHz, an LO frequency of 24 GHz, and multiple clock buffers between the reference clock source and the daughtercards, minimizing clock jitter was one of the most challenging parts of the system design. Multiple different PLLs and clock buffers were simulated to find the best configuration. Figure 8.7 shows the simulated phase noise contributions of the different components in the final system, as well as the expected total phase noise.

At low frequencies (i.e. within the loop bandwidth), the reference clock dominates the phase noise. This phase noise is a combination of the noise from the crystal and fractional-N PLL that generates the low-frequency clock for all the daughtercards, as well as the noise contribution from the buffers in the clock tree. Above the filter cut-off frequency, the VCO in the BGT24 is the main contributor to the phase noise. By integrating the phase noise from 100 Hz to 10 MHz, it is estimated that the RF daughtercards will exhibit 457 fs RMS jitter at 24 GHz. This RMS jitter is just 1% of the 24 GHz oscillator period, and will be acceptable for microwave imaging.

8.5   Software Architecture

The real-time imaging system consists of four pieces of software running simultaneously: the firmware on the daughtercards, gateware on the central FPGA hub, the RMA algorithm running on a desktop machine and a visualization engine to display the final 3-D image. The functions of each of these pieces of software, and how they interact, is shown in Figure 8.8.

Upon power-up, the firmware on the daughtercards will configure the BGT24 RF transceiver, PLL and VGA using the serial-peripheral interface (SPI). The FPGA then sends a synchronization (sync) pulse to each daughtercard to indicate the start of a new imaging frame.
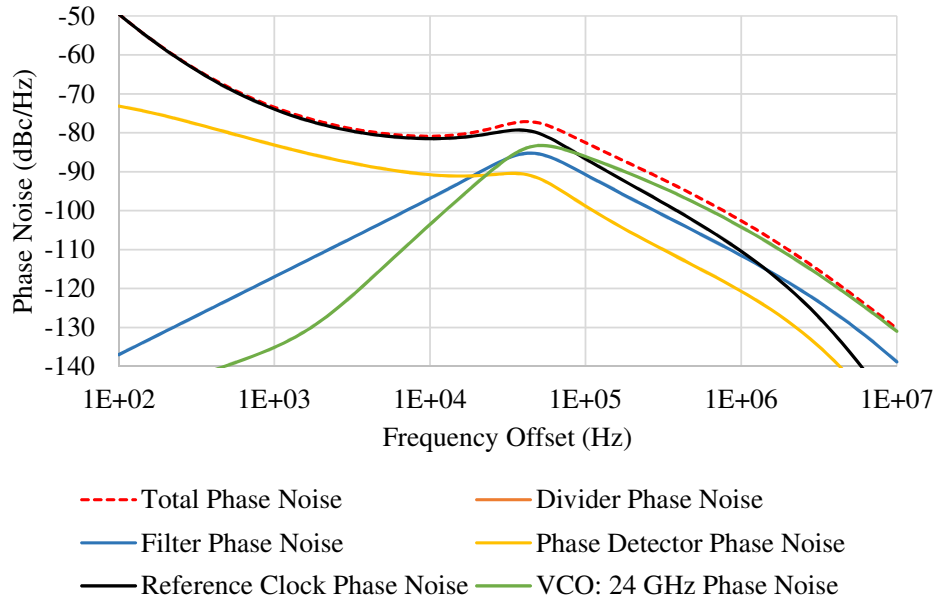
Figure 8.7: The contribution of the different components to the total closed-loop phase noise at 24 GHz, simulated using the Hittite PLL Design Tool.

Each transmit daughtercard will turn its antenna on and off at the appropriate time, while the ARM microcontroller on the receive daughtercards will sample the baseband receive signal. These actions are all synchronized using further sync pulses.

During the imaging process, the receive daughtercards are also sending the samples that they collect to the FPGA, via a ring network. The FPGA then forwards these samples to a desktop computer over a 1 Gbps Ethernet connection. Software running on the desktop computer buffers up a full frame of samples, before processing them using the X-MIMO RMA. The resulting 3-D image matrix is forwarded to a visualization engine, which renders and displays the 3-D image of the scene.

8.6   Performance Measurements of the Real-time Imaging Hardware

Before building the full 128-antenna array, a small prototype run of four transmitter and four receiver daughtercards was performed. The main purpose of this prototype run was to determine if the RF VCO on the daughtercards was stable enough for microwave imaging. This concern stemmed from the fact that the BGT24 RF transceiver was developed for the purpose of measuring automobile velocity from Doppler shift. For Doppler measurements, phase noise and jitter is not very important.

Four different experiments were therefore performed using two daughtercards to determine if the phase noise was acceptable. In the first experiment, the phase noise at 24 GHz is
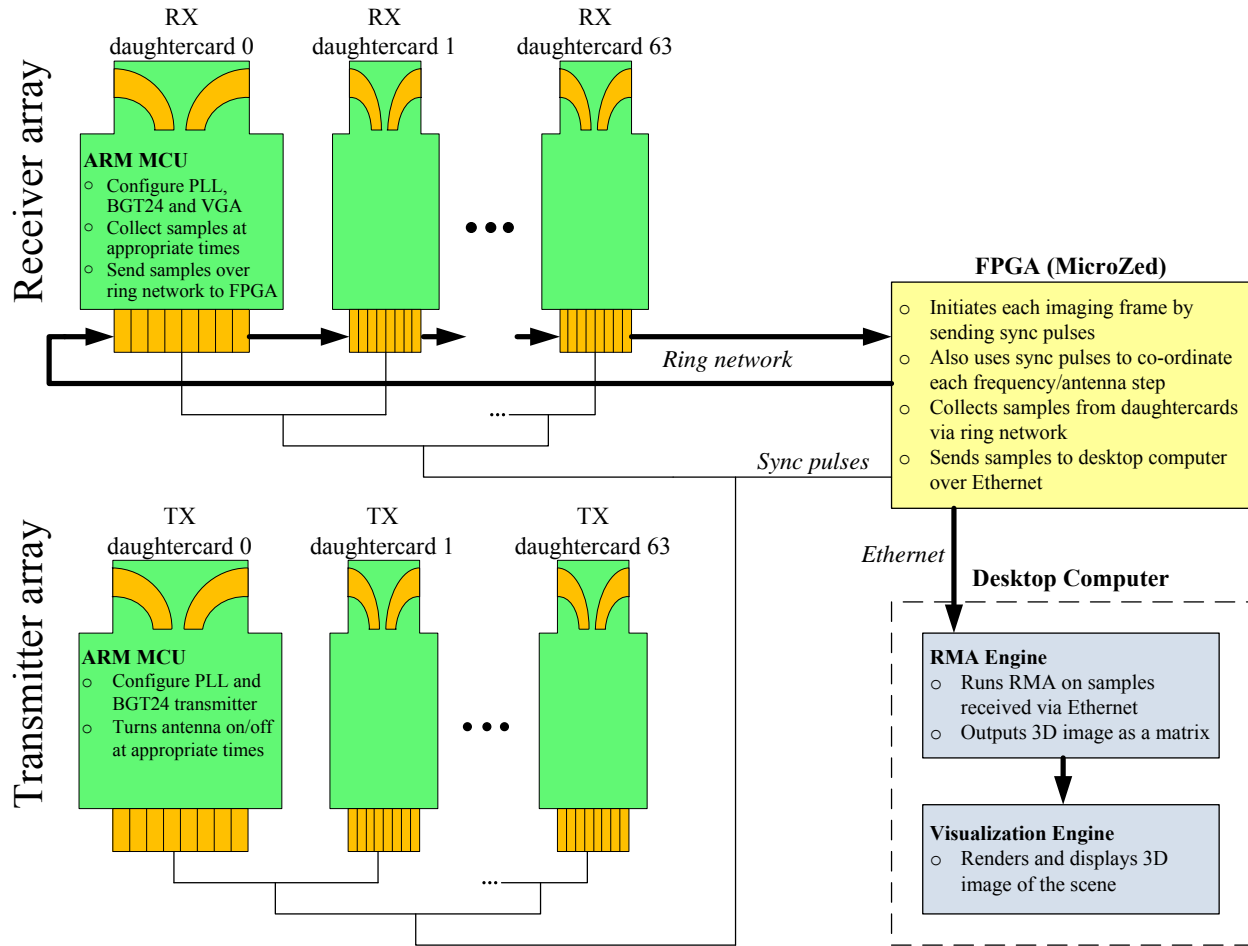
Figure 8.8: Software architecture for the real-time imaging system

measured directly using a spectrum analyzer. Next, the effect of this phase noise on image quality is determined. Since more than two daughtercards are required to perform 3-D microwave imaging, distance (ranging) measurements are used instead as a proxy for imaging. The distance between the two daughtercards is determined by measuring the phase of the received signal, over a range of carrier frequencies, in the second experiment. The error in the distance measurements gives a good indication of the expected error in the 3-D images, as the 3-D imaging algorithm also uses phase to measure distance, except, in this case, between the antennas and points in the scene. The third experiment then uses frequency-modulated continuous wave (FMCW) signals to measure the distance between two daughtercards. The last experiment determines the velocity of a moving object from Doppler measurements.

To aid in these experiments, a small carrier board was designed to hold two daughtercards in a two-element array. The daughtercards and carrier board from the prototype run are shown in Figures 8.9 and 8.10. The four experiments and their results are described in the rest of this chapter.
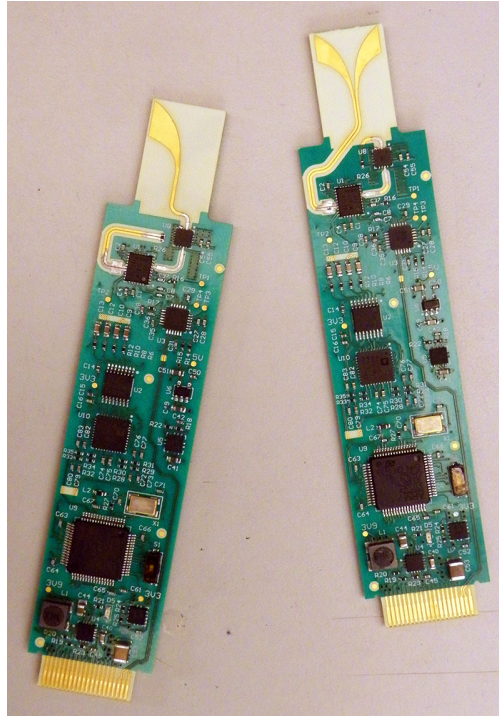
Figure 8.9: Fabricated receive (left) and transmit (right) daughtercards

8.6.1   Phase noise measurements

The aim of the first experiment was to directly measure the phase noise of the transmitted signal at 24 GHz, using an external spectrum analyzer.

Methodology

The BGT24 transceiver on a transmit daughtercard was configured to constantly transmit. The PLL was fed a fixed 30 MHz reference signal, resulting in a 24 GHz RF signal. The PLL lock-detect signal was monitored to ensure that the PLL remained locked during the experiment.

A receiving horn antenna, connected to the input of a spectrum analyzer, was then placed close to the daughtercard antenna. The phase noise of the transmitted signal was plotted using the phase noise measurement function of the spectrum analyzer.

Results

The measured phase noise is shown in Figure 8.11. At almost all frequency offsets, the measured phase noise is 10dB higher than expected (compare to Figure 8.7). The exception is below 200 Hz, where measured phase noise is slightly lower than the simulation predicted.
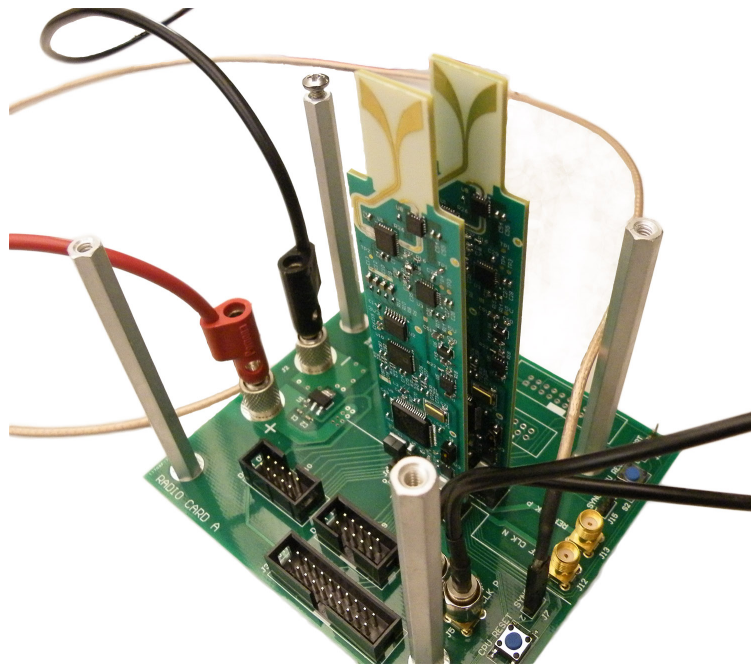
Figure 8.10: Two transmit daughtercards plugged into the prototype carrier, forming a small two-antenna array

The most likely cause is that the phase noise generated by the VCO in the BGT24 was higher than expected, as scant phase noise specifications were available for this part.

The additional in-band phase noise increased the RMS jitter by a factor of 3, from the simulated 457 fs to 1.3 ps (11.2°). The results in Section 4.8 showed that the RMS jitter at each antenna needs to be below 72° to form a reasonable image. Therefore, even with the increased jitter, the RF daughtercards are still viable for 3-D microwave imaging. They will therefore be further evaluated in the remaining experiments to determine how accurately they can measure distance and velocity.

8.6.2   Range measurements using stepped CW

The distance between a transmitter and a receiver daughtercard is determined through a number of phase measurements. The two daughtercards are setup, facing each other, at some distance apart. The transmit card slowly steps through N different frequencies. At each frequency step, the receive daughtercard measures the phase of the received signal. By evaluating how the measured phase changes with frequency, the distance between the two daughtercards can be calculated. This algorithm is essentially $1 \times 1 \times N$ 3-D imaging, with just one pixel in the cross-range directions.
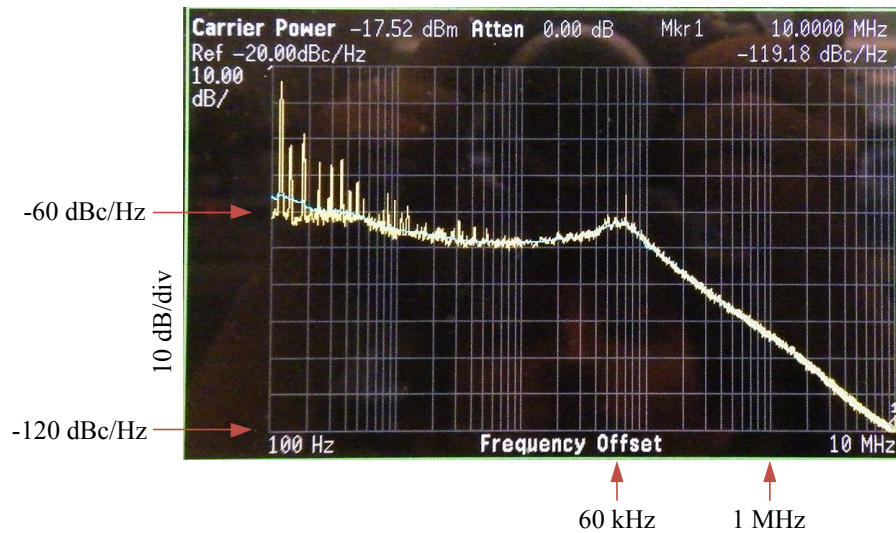
Figure 8.11: Measurement of the transmit daughtercard RF phase noise at 24 GHz

Methodology

The transmit and receive daughtercards were placed 1 m apart, facing each other, as shown in Figure 8.15. The experiment was also repeated with the daughtercards 2 m apart. The two daughtercards were fed a common low-frequency reference clock. The RF signal was transmitted line-of-sight from transmitter to receiver, rather than reflecting off an object, to minimize experimental error. Since the path loss for direct line-of-sight is much lower than reflecting off an object, the transmit power was decreased to prevent saturating the receiver.
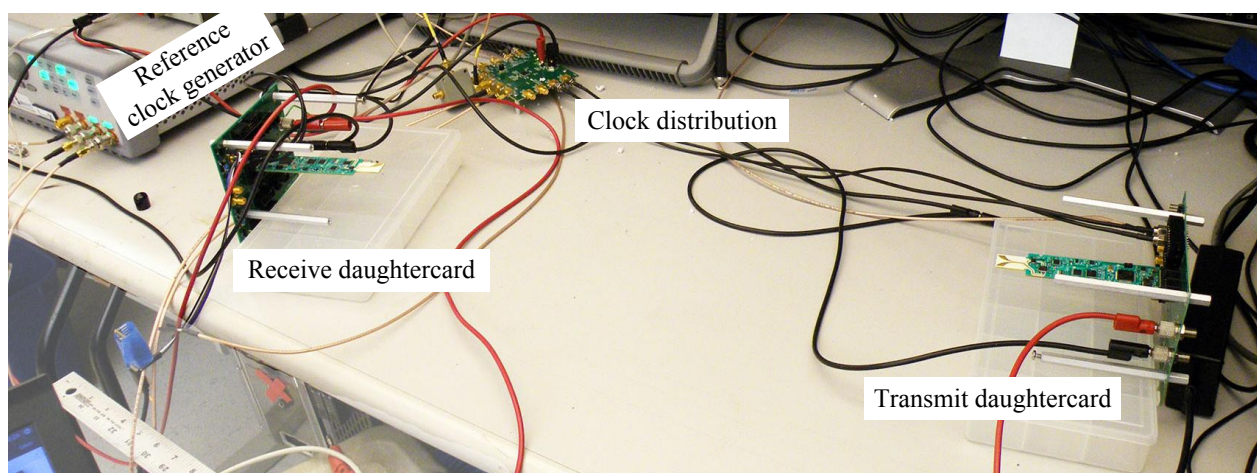
Figure 8.12: Experimental setup for calculating the physical distance between two daughtercards using RF phase measurements

The transmitter stepped through 128 frequencies, dwelling for 1 ms at each frequency

step. The measurements were initially made over the entire 4 GHz bandwidth, from 22.5 - 26.5 GHz, but after experiencing problems with noise and frequency-dependent effects, the bandwidth was reduced to 600 MHz. Multiple samples were collected at the receiver at each frequency step and averaged to improve SNR.

Results

The experiment was first performed with the transmitter switched off to determine how the receive baseband would react to a changing LO frequency. Since no RF signal is being received, one would expect the baseband receive signal to be zero at each frequency step. The dotted curve in Figure 8.13 clearly contradicts this expectation. It appears that the level of the "constant" DC offset at the baseband output of the BGT24 is dependent on the frequency of the LO. Therefore, as the LO is swept, the DC offset in the baseband changes, even though no signal is received and the PLL remains locked. Unfortunately, this changing DC offset cannot be filtered out, as it changes at a similar rate to the received signal (i.e. at every frequency step). The only solution is to characterize this change in DC offset against LO frequency, and subtract it from the actual received signal after sampling. The disadvantage of this approach is that it reduces the number of usable ADC bits.
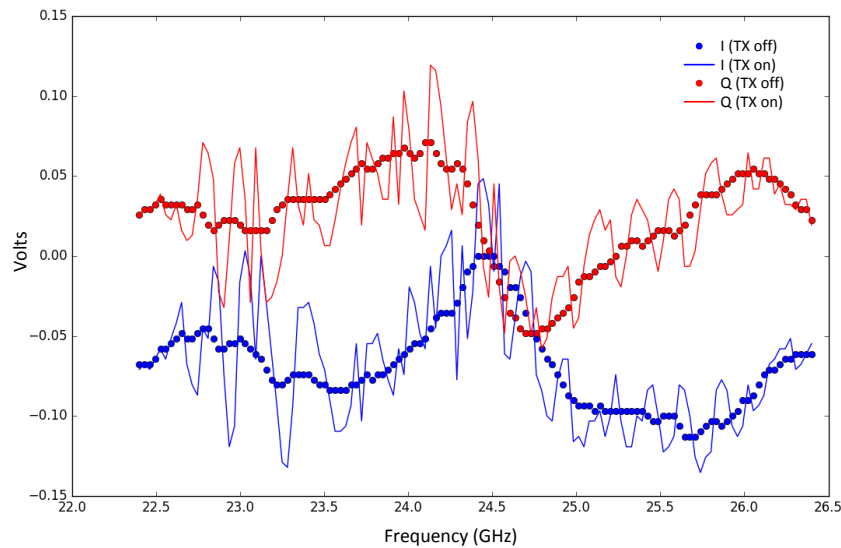
Figure 8.13: Baseband received signal (I and Q) for stepped-CW measurements. The dotted lines show the baseband signal when the transmitter is turned off, and the solid lines shows the case when the transmitter is operating.

The solid line in Figure 8.13 shows the baseband received signal for the case when the transmitter was turned on and placed 0.5 m from the receiver. It is clear that the magnitude of the changes in the DC offset is much larger than the received signal. If the DC offset (dotted line) is subtracted from the baseband signal when the transmitter was turned on,

the received signal can be extracted. The phase of this received signal is plotted at each frequency step in Figure 8.14. Since the phase would typically wrap around every 2π, the phase in this plot has been unwrapped to make the figure clearer.

<div align="center">(a)   (b)</div>
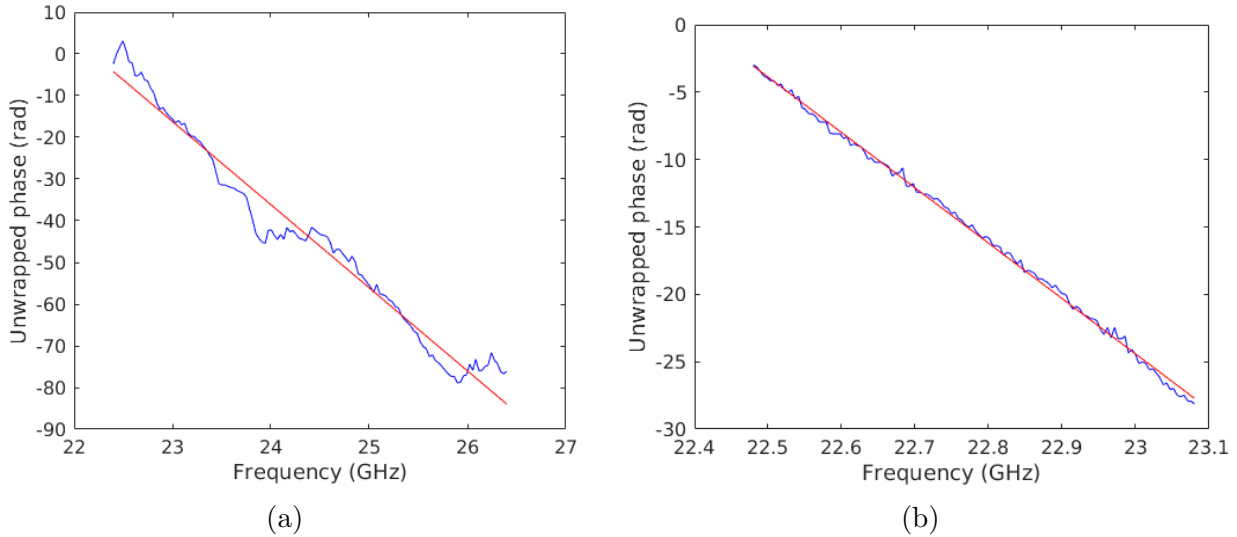
Figure 8.14: The unwrapped phase of the received signal in stepped-CW mode, with (a) the transmitter 1m away and using the full 4 GHz bandwidth, and (b) the transmitter 2m away and using a reduced 600 MHz bandwidth. Blue shows the actual measured phase, while red shows the best fit.

With the transmitter and receiver a fixed distance apart, one would expect the phase of the received signal to increase linearly with frequency, as increasing the frequency increases the number of wavelengths between the transmitter and the receiver. The slope of this line gives the distance between the transmitter and receiver. Any deviation from this straight line is an indication of phase noise.

The phase of the received signal in Figure 8.14(a) deviates from a best-fit straight line with a standard deviation of 240°, much larger than the measured jitter of the RF daughtercard. This large deviation occurs because the measured phase experiences number of discontinuities as the transmit frequency is increased over the full bandwidth, most likely caused by the BGT24 RF transceiver. To avoid these discontinuities, the experiment was repeated over a much smaller 600 MHz bandwidth, from 22.8 to 23.4 GHz. Figure 8.14(b) shows that the measured phase no longer exhibits any sharp phase discontinuities, and that the standard deviation has decreased to 19°.

The previous experiment measured the transmit jitter as 11°. Assuming that the transmitter and receiver experience the same amount of jitter, the expected overall link RMS jitter is $11° \times \sqrt{2} = 16°$, which is reasonably close to the 19° of RMS jitter measured in this experiment. More importantly, this jitter is within the maximum acceptable RMS jitter of 72° that the imaging algorithms can handle.

The experiment was performed multiple times with the reduced 600 MHz RF bandwidth, with both 1 m and 2 m separation between the transmitter and receiver, and the distance calculated from the slope of the resulting best-fit straight line. With the transmitter and receiver 1 m apart, the distance was measured 15 times, resulting in a mean measured distance of 0.98 m and a standard deviation of 0.16 m, while 2 m separation resulted in a mean measured distance of 2.01 m with a standard deviation of 0.04 m.

8.6.3 Range measurements using FMCW

Distance can also be measured by transmitting a frequency-modulated continuous wave (FMCW) and looking at the shift in frequency at the receiver. In this case, the LO at both the transmitter and the receiver is continuously swept from a low to a high frequency, and not in discrete steps. This continuous sweeping means that by the time the transmitted signal has reflected off objects and arrived back at the receiver, the receiver LO has already increased in frequency by an amount proportional to the propagation delay of the signal through the air. Mixing the received signal with the LO results in a low-frequency tone whose frequency is directly proportional to the distance from the transmitter to the receiver. The frequency of this tone is given by [12, ch. 3]:

$$f_{FMCW} = \frac{\text{distance} \times \text{bandwidth}}{c \times T_{\text{chirp}}} \tag{8.2}$$

where T_{chirp} is the duration of the sweep from lowest to highest frequency, and "distance" refers to the total round-trip distance. Since FMCW typically allows faster distance measurements than the stepped-CW approach, experiments were performed with the prototype real-time imaging system operating in FMCW mode.

Methodology and Results

The transmit signal was swept from 22.5 to 26.5 GHz in 1 ms, resulting in a 4 THz/s chirp rate. This frequency sweep was achieved by sweeping the reference clock from 28 to 33 MHz and ensuring that the PLLs remain locked the entire time. During the experiments, the received baseband signal clearly contained tones caused by the difference in LO and RF received signal frequency. However, it was difficult to unambiguously measure distance based on the frequency of these tones, as the Fourier transform of the received signal showed multiple tones of equal magnitude.

These poor results are most likely due to two causes. Firstly, the reference clock source used for the stepped-CW experiments was unable to generate continuous frequency sweeps. Therefore, a different clock source, with 20 dB higher phase noise, was used instead. Secondly, since the reference clock was continuously changing frequency, it was not possible to calibrate out the changing DC offset in the baseband. For these two reasons, it is envisioned that the final real-time imaging system will operate in stepped-CW mode, and not use FMCW.

8.6.4 Velocity measurements using Doppler

To verify the suitability of the RF daughtercards for Doppler imaging, a transmitter and a receiver daughtercard were placed side-by-side and used to measure the velocity of an object moving towards them. As the transmitted wave reflects off the moving object, the received signal should increase in frequency according to (8.3). Since Doppler velocity measurements is the primary commercial application of the BGT24 transceiver IC, this experiment is a good indication of whether the system works.

$$f_{\text{dop}} = \frac{\text{velocity} \times f_{\text{carrier}}}{c} \tag{8.3}$$

Methodology

A transmitter and receiver daughtercard were placed side-by-side, as shown in Figure 8.15 A metal plate of size 5 cm × 30 cm is moved towards the daughtercards using a computer-controlled linear actuator. The transmitter generated a RF signal with a fixed frequency of 24 GHz, while the receiver daughtercard sampled the receive baseband at 5 MSps.
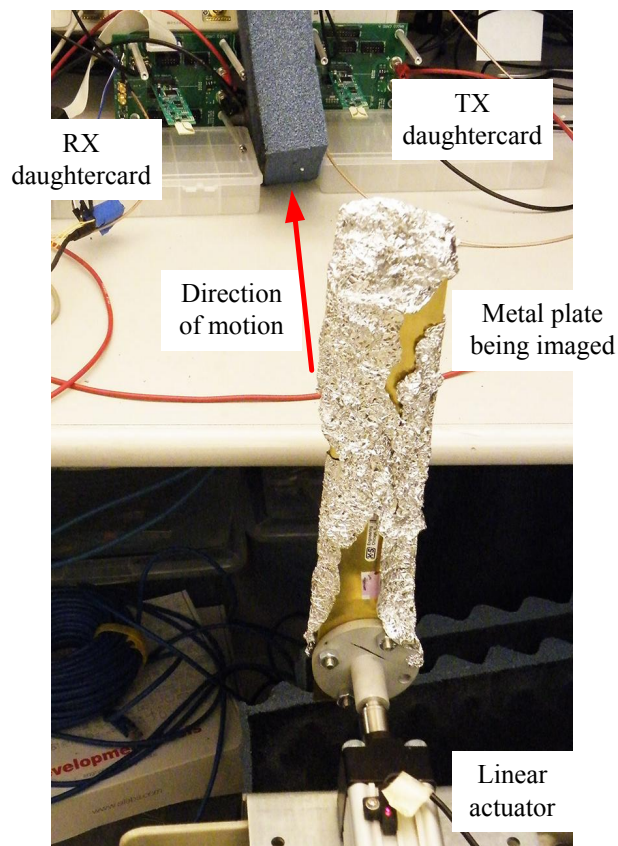
Figure 8.15: Experimental setup for measuring the velocity of a moving object.

Results

Figure 8.16 (a) and (b) shows the baseband received signal and the corresponding Fourier transform (with X-axis scaled to velocity) for the object moving at 150 and 250 mm/s respectively. In both cases, there is a clear peak in the Fourier transform within 4% of the correct velocity. Unfortunately, the spectrum also contains harmonics of significant magnitude, most likely caused by distortion at some stage in the transmit or receive chain.
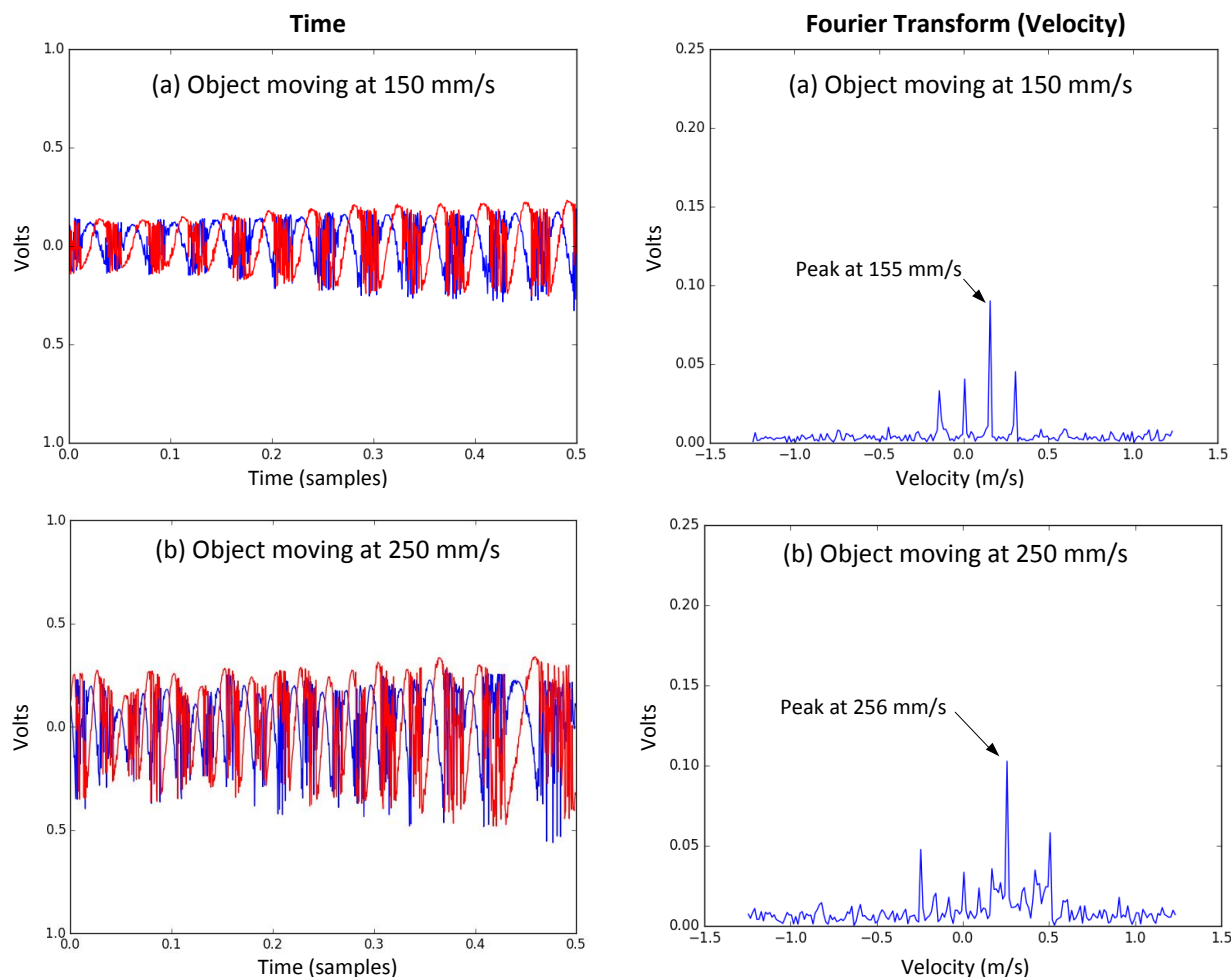
Figure 8.16: The results of the experiments using Doppler shift to measure velocity

8.7 Conclusion

A modular real-time microwave imaging system was designed, consisting of a number of RF daughtercards that can be plugged into a backplane to form an antenna array. Each daughtercard contained a 24 GHz RF transceiver, a PLL, a baseband receive chain, ADCs

and a microcontroller. It was decided that arranging 128 of these daughtercards in a X-MIMO configuration, and processing the results using the X-MIMO RMA, would be the most economical way to illustrate the capabilities of a real-time imaging system.

After building a small number of daughtercards, it was found that the RF phase noise was 10 dB higher than expected. Fortunately, this only resulted in the RMS jitter increasing from the expected 1% to 3% of the clock period. Since the microwave imaging algorithms require that the RMS jitter be below 20% of the clock period, the daughtercards should be suitable for microwave imaging. The suitability of the daughtercards was further verified by attempting to use two of them to measure range via stepped-CW measurements. When placing the transmitter and receiver daughtercards 2 m apart, and stepping the transmit signal through a 600 MHz bandwidth, the measured phase increased linearly with a standard deviation of just 19°. The distance between the two daughtercards was calculated, from these phase measurements, to be 2.01 ± 0.04 m. Achieving accurate distance measurements is important, as it is the basis of the RMA.

Unfortunately, attempting to use the full 4 GHz bandwidth to measure distance was unsuccessful, as the resulting phase measurements showed sharp discontinuities at certain frequencies. Attempts to measure distance using FMCW were also unsuccessful, but in this case it was mostly due to a noisier-than-expected reference clock generator. Success was found again by using the RF daughtercards to measure the velocity of a moving object from its Doppler shift.

The daughtercards are therefore suitable for building modular real-time microwave imaging systems, provided the RF bandwidth is kept within 600 MHz. The next step is to manufacture the remaining daughtercards and design a suitable carrier board for all 128 cards. However, this step is a significant engineering undertaking and beyond the scope of this dissertation. It might also be advantageous to find a suitable replacement for the BGT24 RF transceiver that exhibits better phase response over the full RF bandwidth. Fortunately, it is most likely that new 24 and 60 GHz RF transceivers will be released in the near future with better phase noise characteristics, as the technology matures and the demand for commercial phased arrays increases.

Chapter 9

Conclusion

9.1 Summary of Work

This dissertation has focused on designing cost- and energy-efficient microwave imaging systems, with the goal of capturing 3-D images of people and objects within a room. Microwave imaging was shown to be well suited to indoor environments, as unlike optical imaging techniques, microwave imaging works in all lighting conditions and is able to directly capture 3-D images. Microwave imaging systems can also be made compact and unobtrusive, through the use of printed antennas. However, the resolution achievable by microwave imaging, within a room-sized environment, is typically on the order of millimeters to tens of millimeters. This limitation means that microwave imaging is best suited to applications where only moderate image resolution is required, such as locating people within an indoor environment or recognizing hand gestures.

Most of the microwave images in this dissertation were produced using variants of the range-migration algorithm (RMA). This algorithm allows 3-D images to be captured using a 2-D antenna array. One or more antennas in the array illuminate the scene with a CW RF signal, while other antennas record the signal that is reflected back by the objects in the scene. This illumination and sampling is repeated at many different frequencies. Through the application of Fourier transforms and Stolt interpolations, these backscattered RF measurements are converted into a 3-D image of the scene. This algorithm works well for indoor microwave imaging, as it takes into account the curvature of the wavefront within the array near field. Novel variants of this algorithm were also developed, including algorithms for MIMO systems, single-transmitter systems and Doppler imaging systems that both image the scene and calculate the velocity of every object in it.

A microwave imaging testbed was built to characterize the performance of these microwave imaging algorithms in different environments and antenna array configurations. This testbed used an XY-table to move a transmit antenna and a receive antenna within a 2-D aperture, allowing any array configuration to be emulated. The RF frontend was built using off-the-shelf components, and operated from 17 to 20 GHz. Standard imaging

phantoms were also developed, using both metal and pig tissue. These phantoms allowed the image resolution and image SNR, achieved by each array configuration and algorithm, to be measured in a repeatable fashion.

The imaging testbed yielded a number of useful results. It was found that images could be obtained at distances of 0.5 m with a transmit power as low as 1µW. Furthermore, transmit power affected image SNR only, and not image resolution. An 80×80 antenna array, using the colocated RMA, was able to image objects with a resolution of 12.5 mm, when the objects were placed 0.5 m from the array. Other RMA variants that used small transmit apertures relative to array size, such as the single-transmitter MIMO algorithm, produced images with only half as good resolution.

Array size was found to be the most important parameter in microwave imaging system design. Increasing the aperture results in a proportional improvement in image SNR and image resolution, until the resolution reaches the half-wavelength limit. Unfortunately, increasing the array size by simply moving the antennas further apart is not possible, as antenna spacing larger than 0.9λ resulted in unrecognizable images. It was also found that these systems are well suited to imaging human hand phantoms, primarily due to the diffuse nature of the microwave reflection off the skin, validating the utility of these systems for imaging people within a room.

While 2-D antenna arrays were shown to generate high quality images, two major problems limit the commercial viability of the technology: cost and power consumption. One solution is to reduce the cost and power consumption of the RF transceiver components. Simulations showed that these microwave imaging systems are able to operate with very low power PAs at the transmitter, and low power, and hence noisy, LNAs at the receiver. In both cases, reducing the power or increasing the noise figure of these components should also reduce cost. Furthermore, it was found that larger antenna arrays are more energy efficient than smaller arrays, due to the larger array gain. These results lead to the development of a methodology for designing cost and energy efficient microwave imaging systems.

Alternatively, cost and power can be reduced by decreasing the number of antennas in the array, while keeping the array aperture fixed. A new compressive sensing algorithm was therefore developed for 3-D microwave imaging, that allows images to be formed using sparse antenna arrays that are just 4% dense. This algorithm takes advantage of the fact that the objects in the scene have the same reflectivity over a large surface, resulting in distributed surfaces with uniform intensity in the final images. Such images are known to be sparse in the wavelet domain, hence allowing compressive sensing to be used. The decrease in the number of antennas does however come at the cost of increased computational complexity.

While most of this work focuses on generating 3-D images from the phase of the backscattered radio waves, two other microwave imaging techniques were also discussed. One technique is using timed arrays, which typically transmit very short pulses to image objects in the array far-field. The antennas in the receive array are delayed and summed to form a narrow beam that can be raster scanned over the scene. Timed arrays can also be used to image objects in the near-field, by focusing all the antennas on a single point rather than in a particular direction. However, the hardware required to achieve reasonable image resolution

within a room-sized environment was found to be technically and economically unfeasible.

While radio interferometry is typically used to image astronomical bodies, it was found that interferometry is actually very similar to timed arrays. The most straightforward approach to imaging is to form a narrow beam by correlating different antenna outputs over a range of relative delays. However, a more scalable approach is to directly sample the individual antenna outputs, without delay elements, and correlate them in the frequency domain. The main advantage of using an interferometric approach for microwave imaging is that it allows fewer antennas to be used. While interferometry remains primarily a 2-D far-field imaging technology, recent research indicates that it may be possible to adapt interferometry for near-field 3-D imaging.

The microwave imaging testbed, which was used for capturing all the microwave images presented in this dissertation, worked well for evaluating the different imaging algorithms, but it does not allow real-time microwave imaging. The architecture for a real-time microwave imaging system was therefore discussed and a small prototype array built. This real-time system consisted of an array of RF daughtercards, each containing an antenna and RF frontend, that could be plugged into a common carrier board. After building a small number of daughtercards, the RF phase noise was measured and found to be acceptable for RMA imaging. Since only a small number of daughtercards were manufactured, building a complete imager was not possible. Instead, two daughtercards were used to very accurately measure distance based on phase measurements taken at different frequencies. Since measuring distance from phase is the basis of the RMA imaging algorithms, the success of these experiments show that the architecture outlined here is viable for designing real-time microwave imaging systems. Furthermore, a clear path was described for scaling the two-antenna prototype to a full 128 antenna system.

9.2 Future Work

The microwave imaging algorithms and systems, discussed in this dissertation, can be extended in two main ways: further improving the image capture techniques, and post-processing the final 3-D images.

9.2.1 Further improvements to microwave imaging systems

There still remain a number of improvements, that were not fully investigated, that can be made to further improve the imaging speed or reduce the system cost of microwave imaging systems. These improvements were mentioned in previous chapters and are summarized here.

Building a full array for the real-time imaging system

While a small two-antenna array was built for the real-time imaging system, this array can be extended to a full real-time 3-D imaging system by building all 128 RF daughtercards and

a new carrier board. It may also be desirable to replace the RF transceiver integrated circuit with a different part that provides a larger usable bandwidth. A real-time microwave imaging system, such as this system, would be invaluable for investigating the image post-processing algorithms discussed in Section 9.2.2.

Accelerating the compressive sensing algorithm

The compressive sensing algorithm discussed in Chapter 6 is currently too slow for real-time imaging. One solution would be to accelerate the algorithm by implementing it on specialized hardware, such as an FPGA or ASIC. Another solution is to seed the image reconstruction algorithm with the previous recovered video frame, which, provided the images do not change much between video frames, could substantially reduce computation time.

Radio interferometry in the array near-field

Much like the compressive sensing approach, radio interferometry provides a method for reducing the number of antennas in the array, without sacrificing image quality. Unfortunately, traditional radio interferometry is not able to image objects within the array near-field. Possible modifications to the algorithm to allow near-field and 3-D imaging were discussed in Chapter 7 and should be investigated further.

9.2.2 Image post-processing

This dissertation has concentrated on how to capture 3-D images of people and objects within a room, in a cost- and energy-efficient manner. The next step is deciding what to do with the images once they have been captured using the proposed real-time microwave imaging system. Post-processing these images will allow more useful information to be extracted from them. This is especially important if the images will be primarily consumed by a machine, rather than a person, as is the most likely case. It is believed that post-processing is the area where most future work on microwave imaging will focus, and will perhaps be the most interesting aspect of the field. Some examples of image post-processing are described below.

Object detection using Doppler imaging

Doppler imaging was shown to both image a scene and calculate the velocity of every voxel in the resulting images. Therefore, if an object moves in the room, all the voxels representing that object will have the same velocity in the output image. Therefore, by clustering neighboring voxels with similar velocities, it should be possible to detect individual objects. This data will aid in determining the number of people in the room and where they are positioned.

Object classification

While object detection allows moving objects to be detected, it would be more useful to know whether the moving object is a human or a cat, for example. Image classification techniques from optical imaging should help here. It may also be possible to use models of what people look like and how they move to better identify them, such as in [72].

Future frame estimation from Doppler imaging

If there are no moving objects within a room, then the images produced by the microwave imaging system will be identical from frame to frame. The imaging frame rate can therefore be reduced to save energy. Furthermore, if an object is moving in the room, and its velocity is calculated from the Doppler shift, the position of the object in the next frame can be estimated. Therefore, if reliable motion estimation data is available, the microwave imaging system does not actually need to capture every single frame.

9.3 Where is Microwave Imaging Headed?

It is the belief of the author that the future of microwave imaging lies not in large arrays with apertures over a meter long. Instead, microwave imaging systems will shift to higher millimeter-wave frequencies, allowing the antenna arrays to become much more compact. Figure 8.1 showed that increasing the operating frequency of the array, while keeping the number of antennas constant, has no effect on image resolution, but will result in a physically smaller antenna array, assuming half-wavelength antenna spacing. Therefore, higher operating frequencies allow physically smaller antenna arrays with the same image resolution.

Furthermore, it is expected that more RF transceiver ICs that support large arrays will become commercially available. This movement in the industry is already starting to happen, with Broadcom[1] and Samsung[2] recently announcing 60 GHz transceivers with support for up to 32 antennas on the same package. Therefore, instead of building arrays of thousands of separate antennas and transceivers, less than a hundred of these transceiver modules can be tiled together on single PCB, creating an equivalent antenna array in a smaller form factor.

Finally, while all microwave images in this dissertation were produced for viewing by humans, it is expected that most microwave images will not be consumed by humans, but rather by machines running image processing algorithms. It is therefore expected that a large amount of future work will focus on how to automatically extract useful information from these images.

---

[1] `https://www.broadcom.com/news/press-releases/broadcom-announces-industrys-first-60-gHz-wireless-mesh-solution`

[2] `https://news.samsung.com/global/samsung-electronics-60ghz-wi-fi-technology-accelerates-data-transmission-by-five-times`

Bibliography

[1] J. Lopez-Sanchez and J. Fortuny-Guasch, "3-D radar imaging using range migration techniques," *IEEE Trans. Antennas Propag.*, vol. 48, no. 5, pp. 728–737, May 2000.

[2] B. S. Cook, B. Tehrani, J. R. Cooper, and M. M. Tentzeris, "Multilayer inkjet printing of millimeter-wave proximity-fed patch arrays on flexible substrates," *IEEE Antenn. Wireless Propag. Lett.*, vol. 12, pp. 1351–1354, 2013.

[3] D. Sheen, D. McMakin, and T. Hall, "Three-dimensional millimeter-wave imaging for concealed weapon detection," *IEEE Trans. Microw. Theory Techn.*, vol. 49, no. 9, pp. 1581–1592, Sep 2001.

[4] J. Dong, "Microwave lens designs: Optimization, fast simulation algorithms, and 360-degree scanning techniques," Ph.D. dissertation, Dept. Elect. Eng., Virginia Polytechnic Inst. and State Univ., Falls Church, VA, 2009.

[5] C. Zhang, M. Kuhn, B. Merkl, M. Mahfouz, and A. E. Fathy, "Development of an UWB indoor 3d positioning radar with millimeter accuracy," in *2006 IEEE MTT-S International Microwave Symposium Digest*, June 2006, pp. 106–109.

[6] E. Mok and G. Retscher, "Location determination using WiFi fingerprinting versus wifi trilateration," *Journal of Location Based Services*, vol. 1, no. 2, pp. 145–159, 2007.

[7] B.-J. Jang, S.-H. Wi, J.-G. Yook, M.-Q. Lee, and K.-J. Lee, "Wireless bio-radar sensor for heartbeat and respiration detection," *Progress In Electromagnetics Research C*, vol. 5, pp. 149–168, 2008.

[8] E. F. Greneker, "Radar sensing of heartbeat and respiration at a distance with security applications," vol. 3066, 1997, pp. 22–27.

[9] K. Khoshelham and S. O. Elberink, "Accuracy and resolution of kinect depth data for indoor mapping applications," *Sensors (Basel)*, vol. 12, no. 2, p. 14371454, 2012.

[10] M. Kyto, M. Nuutinen, and P. Oittinen, "Method for measuring stereo camera depth accuracy based on stereoscopic vision," vol. 7864, Jan. 2011, pp. 78 640I–1 – 78 640I–9.

[11] R. J. Przybyla, H. Y. Tang, S. E. Shelton, D. A. Horsley, and B. E. Boser, "3D ultrasonic gesture recognition," in *2014 IEEE International Solid-State Circuits Conf. Digest of Technical Papers (ISSCC)*, Feb 2014, pp. 210–211.

[12] B. R. Mahafza, *Radar Systems Analysis and Design using MATLAB.* CRC Press, 2000.

[13] R. J. Mailloux, *Phased Array Antenna Handbook*, 2nd ed. Artech House, 2005, pp. 12-13.

[14] A. L. Boyer, P. M. Hirsch, J. A. Jordan, L. B. Lesem, and D. L. Van Rooy, "Reconstruction of ultrasonic images by backward propagation," in *Acoustical Holography*, A. Metherell, Ed. Springer US, 1971, pp. 333–348.

[15] G. Bolondi, F. Rocca, and S. Savelli, "A frequency domain approach to two-dimensional migration," *Geophysical Prospecting*, vol. 26, no. 4, pp. 750–772, 1978.

[16] C. Cafforio, C. Prati, and F. Rocca, "SAR data focusing using seismic migration techniques," *IEEE Trans. Aerosp. Electron. Syst.*, vol. 27, no. 2, pp. 194–207, Mar 1991.

[17] A. J. Hunter, B. W. Drinkwater, and P. D. Wilcox, "The wavenumber algorithm: Fast Fourier-domain imaging using full matrix capture," *AIP Conf. Proc.*, vol. 1096, no. 1, pp. 856–863, 2009.

[18] M. Soumekh, "Bistatic synthetic aperture radar inversion with application in dynamic object imaging," *IEEE Trans. Signal Process.*, vol. 39, no. 9, pp. 2044–2055, Sep 1991.

[19] X. Zhuge and A. Yarovoy, "Three-dimensional near-field MIMO array imaging using range migration techniques," *IEEE Trans. Image Process.*, vol. 21, no. 6, pp. 3026–3033, June 2012.

[20] W. C. Chew, *Waves and Fields in Inhomogeneous Media.* IEEE Press, 1995.

[21] R. H. Stolt, "Migration by Fourier transform," *GEOPHYSICS*, vol. 43, no. 1, pp. 23–48, 1978.

[22] L. Liang, M. Jungang, J. Yuesong, and L. Zhiping, "Near-field radar 3d synthetic aperture imaging based on stolt interpolation," in *2005 Asia-Pacific Microwave Conf. Proc.*, Dec 2005, pp. 1–4.

[23] H. Callow, M. Hayes, and P. Gough, "Wavenumber domain reconstruction of SAR/SAS imagery using single transmitter and multiple-receiver geometry," *Electronics Letters*, vol. 38, pp. 336–338, March 2002.

[24] S. Li, B. Ren, H.-J. Sun, W. Hu, and X. Lv, "Modified wavenumber domain algorithm for three-dimensional millimeter-wave imaging," *Progress In Electromagnetics Research*, vol. 124, pp. 35–53, 2012.

[25] X. Zhuge, T. G. Savelyev, A. G. Yarovoy, L. P. Ligthart, and B. Levitas, "Comparison of different migration techniques for uwb short-range imaging," in *European Radar Conf. (EuRAD)*, Sept 2009, pp. 184–187.

[26] T. H. Lee, *Planar Microwave Engineering.* Cambridge University Press, 2004.

[27] V. Kasabegoudar, D. Upadhyay, and K. J. Vinoy, "Design studies of ultra-wideband microstrip antennas with a small capacitive feed," *International Journal of Antennas and Propagation*, vol. 2007, no. 67503, pp. 1–8, 2007.

[28] U. S. Kim, D. D. Lorenzo, J. Gautier, P. Enge, and J. A. Orr, "Phase effects analysis of patch antenna CRPAs for JPALS," in *Proceedings of the 17th International Technical Meeting of the Satellite Division of The Institute of Navigation (ION GNSS 2004)*, Sep 2004, pp. 1531 – 1538.

[29] L. Wirola, I. Kontola, and J. Syrjarinne, "The effect of the antenna phase response on the ambiguity resolution," in *2008 IEEE/ION Position, Location and Navigation Symposium*, May 2008, pp. 606–615.

[30] P. J. Gibson, "The vivaldi aerial," in *9th European Microwave Conf.*, Sept 1979, pp. 101–105.

[31] M. Zhou, "Design and time-domain analysis of antenna array for UWB imaging application," Ph.D. dissertation, School of Elect. Eng. and Comp. Sci., Queen Mary University of London, London, UK, 2014.

[32] R. O. Lee and R. N. Simons, "Effect of curvature on tapered slot antennas," in *1996 Digest IEEE Antennas and Propagation Society International Symposium*, vol. 1, July 1996, pp. 188–191.

[33] J. L. Prince and J. M. Links, *Medical Imaging Signals and Systems*, 1st ed. Prentice Hall, 2005, pg. 165.

[34] L. Wirola, I. Kontola, and J. Syrjarinne, "The effect of the antenna phase response on the ambiguity resolution," in *2008 IEEE/ION Position, Location and Navigation Symposium*, May 2008, pp. 606–615.

[35] B. W. Cook, A. Molnar, and K. S. J. Pister, "Low power rf design for sensor networks," in *2005 IEEE Radio Frequency integrated Circuits (RFIC) Symposium*, June 2005, pp. 357–360.

[36] R. Min, M. Bhardwaj, S.-H. Cho, E. Shih, A. Sinha, A. Wang, and A. Chandrakasan, "Low-power wireless sensor networks," in *14th International Conf. on VLSI Design*, 2001, pp. 205–210.

[37] S. Voinigescu, *High Frequency Integrated Circuits.* Cambridge University Press, 2013.

[38] A. Hajimiri, H. Hashemi, A. Natarajan, X. Guan, and A. Komijani, "Integrated phased array systems in silicon," *Proceedings of the IEEE*, vol. 93, no. 9, pp. 1637–1655, Sep. 2005.

[39] B. W. Cook, "Low energy RF transceiver design," Ph.D. dissertation, Dept. Elect. Eng., Univ. California, Berkeley, May 2007, Tech. Rep. UCB/EECS-2007-57.

[40] W. A. van Cappellen, S. J. Wijnholds, and J. D. Bregman, "Sparse antenna array configurations in large aperture synthesis radio telescopes," in *2006 European Radar Conf.*, Sept 2006, pp. 76–79.

[41] Q. Huang, L. Qu, B. Wu, and G. Fang, "UWB through-wall imaging based on compressive sensing," *IEEE Trans. Geosci. Remote Sens.*, vol. 48, no. 3, pp. 1408–1415, March 2010.

[42] M. Rossi, A. M. Haimovich, and Y. C. Eldar, "Spatial compressive sensing for MIMO radar," *IEEE Trans. Signal Process.*, vol. 62, no. 2, pp. 419–430, Jan 2014.

[43] Y. Fang, B. Wang, and C. Sun, "Three-dimensional near-field microwave imaging approach based on compressed sensing," in *2015 Int Symp on Antennas and Propagation (ISAP)*, Nov 2015, pp. 1–4.

[44] B. Mamandipoor, M. Fallahpour, G. Malysa, K. Noujeim, U. Madhow, and A. Arbabian, "Spatial-domain technique to overcome grating lobes in sparse monostatic mm-wave imaging systems," in *IEEE MTT-S Int Microw Symp (IMS)*, May 2016, pp. 1–4.

[45] E. J. Candes and M. B. Wakin, "An introduction to compressive sampling," *IEEE Signal Process. Mag.*, vol. 25, no. 2, pp. 21–30, March 2008.

[46] R. G. Baraniuk, "Compressive sensing [lecture notes]," *IEEE Signal Processing Magazine*, vol. 24, no. 4, pp. 118–121, July 2007.

[47] E. J. Candes, J. Romberg, and T. Tao, "Robust uncertainty principles: exact signal reconstruction from highly incomplete frequency information," *IEEE Trans. Inf. Theory*, vol. 52, no. 2, pp. 489–509, Feb 2006.

[48] E. J. Candes, J. K. Romberg, and T. Tao, "Stable signal recovery from incomplete and inaccurate measurements," *Communications on Pure and Applied Mathematics*, vol. 59, no. 8, pp. 1207–1223, 2006.

[49] M. Lustig, D. Donoho, and J. M. Pauly, "Sparse MRI: The application of compressed sensing for rapid MR imaging," *Magnetic Resonance in Medicine*, vol. 58, no. 6, pp. 1182–1195, 2007.

[50] E. van den Berg and M. P. Friedlander, "Probing the Pareto frontier for basis pursuit solutions," *SIAM Journal on Scientific Computing*, vol. 31, no. 2, pp. 890–912, 2008.

[51] S. S. Chen, D. L. Donoho, and M. A. Saunders, "Atomic decomposition by basis pursuit," *SIAM Review*, vol. 43, no. 1, pp. 129–159, 2001.

[52] A. Bjork, *Numerical Methods for Least Squares Problems.* Society for Industrial and Applied Mathematics, 1996.

[53] M. A. T. Figueiredo, R. D. Nowak, and S. J. Wright, "Gradient projection for sparse reconstruction: Application to compressed sensing and other inverse problems," *IEEE Journal of Selected Topics in Signal Processing*, vol. 1, no. 4, pp. 586–597, Dec 2007.

[54] A. Maffett, "Array factors with nonuniform spacing parameter," *IEEE Trans. Antennas Propag.*, vol. 10, no. 2, pp. 131–136, March 1962.

[55] S. Becker, J. Bobin, and E. J. Candès, "NESTA: A fast and accurate first-order method for sparse recovery," *SIAM J. Img. Sci.*, vol. 4, no. 1, pp. 1–39, Jan. 2011.

[56] L. Zhang, T. Yang, R. Jin, and Z.-H. Zhou, "A simple homotopy algorithm for compressive sensing," in *Proc. 18th Int. Conf. Artificial Intelligence and Statistics (AISTATS)*, 2015, pp. 1116–1124.

[57] P. Garrigues and L. E. Ghaoui, "An homotopy algorithm for the lasso with online observations," in *Advances in Neural Information Processing Systems 21.* Curran Associates, Inc., 2009, pp. 489–496.

[58] C. M. Lai, K. W. Tan, L. Y. Yu, Y. J. Chen, J. W. Huang, S. C. Lai, F. H. Chung, C. F. Yen, J. M. Wu, P. C. Huang, K. J. Chang, S. Y. Huang, and T. S. Chu, "A UWB IR timed-array radar using time-shifted direct-sampling architecture," in *2012 Symposium on VLSI Circuits (VLSIC)*, June 2012, pp. 54–55.

[59] A. G. Yarovoy, T. G. Savelyev, P. J. Aubry, P. E. Lys, and L. P. Ligthart, "UWB array-based sensor for near-field imaging," *IEEE Transactions on Microwave Theory and Techniques*, vol. 55, no. 6, pp. 1288–1295, June 2007.

[60] T. S. Chu, J. Roderick, and H. Hashemi, "An integrated ultra-wideband timed array receiver in 0.13um cmos using a path-sharing true time delay architecture," *IEEE Journal of Solid-State Circuits*, vol. 42, no. 12, pp. 2834–2850, Dec 2007.

[61] G. Franceschetti, J. Tatoian, and G. Gibbs, "Timed arrays in a nutshell," *IEEE Transactions on Antennas and Propagation*, vol. 53, no. 12, pp. 4073–4082, Dec 2005.

[62] L. Ziomek, *Fundamentals of Acoustic Field Theory and Space-Time Signal Processing.* CRC Press, 1994.

[63] W. Zhi, F. Chin, and M. Y. w. Chia, "Near field imaging for breast cancer detection by UWB minimum variance beamforming," in *2006 IEEE International Conference on Ultra-Wideband*, Sep 2006, pp. 593–597.

[64] E. J. Bond, X. Li, S. C. Hagness, and B. D. V. Veen, "Microwave imaging via space-time beamforming for early detection of breast cancer," in *2002 IEEE International Conference on Acoustics, Speech, and Signal Processing*, vol. 3, May 2002, pp. 2909–2912.

[65] J. D. Monnier and R. J. Allen, *Radio and Optical Interferometry: Basic Observing Techniques and Data Analysis.* Springer Netherlands, 2013, pp. 325–373.

[66] A. Parsons, D. Backer, A. Siemion, H. Chen, D. Werthimer, P. Droz, T. Filiba, J. Manley, P. McMahon, A. Parsa, D. MacMahon, and M. Wright, "A scalable correlator architecture based on modular FPGA hardware, reuseable gateware, and data packetization," *Publications of the Astronomical Society of Pacific*, vol. 120, no. 873, p. 1207, Nov. 2008.

[67] A. Parsons, J. Pober, M. McQuinn, D. Jacobs, and J. Aguirre, "A sensitivity and array-configuration study for measuring the power spectrum of 21cm emission from reionization," *The Astrophysical Journal*, vol. 753, no. 1, p. 81, 2012.

[68] J. P. Costas, "Medium constraints on sonar design and performance," Tech. Rep., 1965, R65EMH33, GE Co.

[69] J. Lazio, "On near-field w-projection for radio interferometric imaging," Tech. Rep., May 2009, Naval Research Laboratory, NRL/MR/7210–09-9173.

[70] Texas Instruments, "Fractional/integer-N PLL basics," Tech. Rep. SWRA029, Aug 1999.

[71] K. Kihira, Y. Kitsukawa, H. Nakamizo, T. Takahashi, and H. Miyashita, "A phased array antenna using commercial fractional-N PLL synthesizers by clock shift of LE signals," in *The 8th European Conf. on Antennas and Propagation (EuCAP 2014)*, April 2014, pp. 546–550.

[72] S. Ganesh, A. D. Ames, and R. Bajcsy, "Composition of dynamical systems for estimation of human body dynamics," in *Proc. 10th International Workshop on Hybrid Systems: Computation and Control (HSCC 2007)*, Apr 2007, pp. 702–705.